POLITECNICO DI MILANO

Department of Civil and Environmental Engineering

Doctoral Programme in Environment and Infrastructure Engineering

POLITECNICO
MILANO 1863

LAGRANGIAN AND EULERIAN STUDY OF BED-LOAD KINEMATICS

Doctor of Philosophy Dissertation of:

Seyed Abbas Hosseini-Sadabadi

Tutor:
Prof. Francesco Ballio

Advisor:
Prof. Francesco Ballio
Prof. Alessio Radice

I would like to dedicate this thesis to my parents …

Acknowledgements

This thesis project would not have been possible without the support of many people. I hereby wish to express my gratitude to my supervisors, Prof. Alessio Radice and Prof. Francesco Ballio who were abundantly helpful and offered invaluable assistance, support and guidance. Special thanks also to Dr. Jenny Campagnol for the assistance with material provided to support this document. This work was supported by the Research Executive Agency, through the 7th Framework Programme of the European Union, Support for Training and Career Development of Researchers (Marie Curie-FP7-PEOPLE-2012-ITN), which funded the Initial Training Network (ITN) HYTECH 'Hydrodynamic Transport in Ecologically Critical Heterogeneous Interfaces', N.316546.

Abstract

Several processes in fluvial hydrodynamics such as erosion, deposition, bed-forms, etc. are governed by bed-load transport. For several decades, many theoretical and experimental studies were devoted to increasing our understanding of the phenomenological aspects of bed-load transport and, in turn, prediction performance.

The classical approach to bed-load transport, currently used in the engineering practice, relates the expected transport rate to the bulk properties of water flow and sediment. Uncertainties in the results provided by this approach have oriented the most recent research towards a deeper insight in particle motion by direct measurement and detailed analysis of sediment kinematics at small spatial and temporal scales. Most of these works have taken advantage of image-based methods, which are non-intrusive and can provide high-resolution data.

The investigation of sediment kinematics may be approached from a Lagrangian or Eulerian point of view. The former follows the individual particles as they move, whilst the second accounts for a finite control volume and studies the transport properties within this volume.

The present work was primarily aimed at investigating the kinematics of bed-load particles for weak transport conditions induced by one-dimensional turbulent flow. This study presents results from several laboratory experiments with the friction velocity ranging from 1.2 to 1.8 times the threshold value for sediment transport. The runs were performed releasing bed-load particles over a fixed, rough bed, that was created gluing sediment grains over plates. Following that, image analysis was applied to track each moving particle along its trajectory.

A conceptual framework was proposed to define the relevant kinematic quantities to be analyzed, for both the Lagrangian and Eulerian approaches. The starting point of the framework is dividing the particle history into two states, namely motion and stillness. For that, an appropriate criterion for identification was conceived, that is based on comparing the position of the particle at a certain instant with all the positions taken before and after that instant.

Several Lagrangian and Eulerian kinematic properties were measured, including particle instantaneous velocity, hop length and duration, rest time, concentration of moving particles, entrainment and disentrainment rates, and solid discharge. Experimental limitations were

recognized and addressed when possible. Scaling analysis was performed to conclude how measured values could depend on the size of the observation area. In addition, the dependency of the kinematic properties on the bed shear stress was investigated. Encouragingly, the Lagrangian and Eulerian estimates were in good agreement, supporting the unified framework that was used. An attempt was made towards interpreting the results in the light of the main expected physical mechanisms affecting the bed-load particle kinematics.

In summary, the present study is structured as follows:

Chapter 1 provides some theoretical background, and summarizes earlier findings on bed-load kinematics.

Chapter 2 presents a novel descriptive/conceptual framework for the definition and measurement of Lagrangian and Eulerian indicators of bed-load transport.

Chapter 3 describes the experimental conditions for the investigation of motion of bed-load particles over a fixed bed.

Chapter 4 is devoted to particle tracking velocimetry (PTV). The chapter basically presents the methods used to track individual particles, with particular attention onto tracking mistakes and their correction.

Chapter 5 accounts for the post-processing of particle tracking data, focusing on the definition of particle motion/rest as the basis for the measurements, and on the sensitivity of measured values to the chosen definition criterion.

In chapter 6, Lagrangian quantities are studied, and results are compared with those reported in earlier investigations. The impact of a finite observation window on the values obtained for the quantities is also discussed. The innovation of this study is that experimental data will be analysed within the novel conceptual framework proposed in Chapter 2. Additionally, to the author's knowledge this is the first study which investigates the impact of finite observation scale (experimental censorship) on resulting statistics. Measurements will also allow for the analysis of time of motion and time of rest which have previously received limited attention.

Chapter 7 presents the analysis of the Eulerian quantities and of their scaling properties.

In Chapter 8, the results obtained from the Lagrangian and Eulerian approaches are compared to prove the complementarity between the approaches.

The final Conclusions provide the main outcomes of the work.

Contents

List of Figures

List of Tables

Chapter 1 Introduction

1.1 Summary of flow characterization

1.1.1 Flow type

In open channel hydraulics, the flow type is characterized by the Reynolds number (Re), a dimensionless quantity defined as the ratio of inertial forces to viscous forces. Re is expressed as:

$$\mathrm{Re} = UL/\upsilon \tag{1.1}$$

Where U is the bulk velocity, L is the characteristic length, and υ is the kinematic viscosity. In open channel flow the commonly used characteristic length is the hydraulic radius $R = A/\mathrm{w}_p$, the ratio of the flow area to the wetted perimeter. Thus, the Reynolds number for open channel flow is computed as $\mathrm{Re} = UR/\upsilon$. Depending on the different values of Re the flow is classified in the following types [e.g., *French*, 1985]:

$$\begin{cases} \text{Laminar} & \rightarrow \mathrm{Re} < 500 \\ \text{Transitional} & \rightarrow 500 < \mathrm{Re} < 12500 \\ \text{Turbulent} & \rightarrow \mathrm{Re} > 12500 \end{cases}$$

Laminar or viscous flow occurs for Re < 500 where the fluid velocity is low and viscosity of the flow overcomes the internal forces. In this type of flow fluid particles move smoothly along the parallel paths. Re > 12500 represents a *turbulent flow* identified by random, unpredictable three-dimensional fluid motions. However, a flow in between (500 < Re < 12500) is known as *transitional*, a short-lasting phase where flow type intermittently changes between laminar and turbulent.

1.1.2 Flow layers and Turbulent regime

Experimental studies indicated that the flow field in open channels is divided into the following sub layers, representing distinctive characteristics (Fig. 1.1):

1. Viscous sublayer δ' : It is the thin layer where flow is fully laminar without any turbulence (no velocity fluctuations)
2. Buffer layer (mixing layer): in this layer, there is constant mixing of laminar and turbulent flow, and the flow is influenced by turbulence and viscosity. The thickness of this layer is almost five times the viscous sublayer.
3. Turbulent wall shear layer (logarithmic layer): It is the layer (right on top of the buffer layer) wherein the Reynolds shear stress is predominant and the viscous shear stress is effectively negligible. Note that in this layer, Prandtl introduced the mixing length concept and found that the logarithmic law of velocity distribution (the log law of the wall) is preserved. Hence, this layer is also known as logarithmic layer.
4. Turbulent outer layer: In this layer, large eddies produce a strong 3D mixing of fluid in flow.

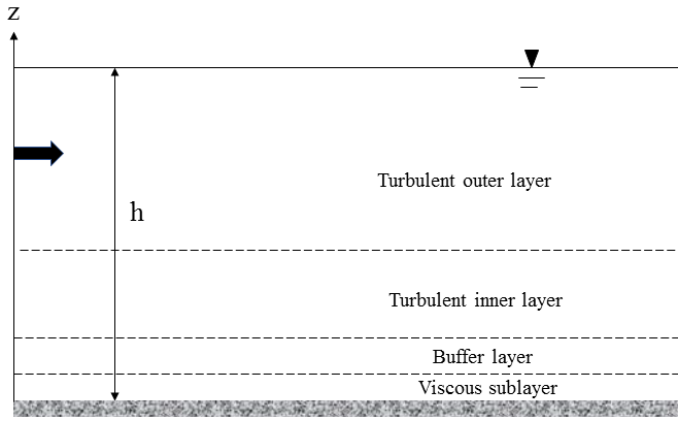

Figure 1.1 Classification of channel flow field in different layers [*Dey*, 2014].

Note that the distance up to the turbulent wall shear layer from the boundary is called *inner layer*. Traditionally, the turbulent flow field in open channels can also be classified into hydraulically *smooth, transitional and rough* flow regimes. This classification is based on the dimensionless shear Reynolds number:

$$\mathrm{Re}^* = u^* k_s / \upsilon \qquad (1.2)$$

Where u^* and k_s are shear velocity and the boundary roughness height respectively. Following different values of Re^* the flow regime is divided into:

1. *Hydraulically smooth flow* $(\mathrm{Re}^* \le 5)$: In this kind of flow, the boundary roughness height k_s is significantly smaller than the viscous sublayer thickness δ' and therefore velocity distributions in turbulent wall shear and outer layers are purely affected by the fluid viscosity (Fig. 1.2a)
2. *Hydraulically rough flow* $(\mathrm{Re}^* \ge 70)$*:* In this flow regime, the boundary (equivalent) roughness height is much larger than the viscous sublayer thickness (Fig. 1.2b). Near the boundary, the roughness produces eddies annihilating the viscous sublayer. The velocity distributions in turbulent wall shear and outer layers are affected by the boundary roughness, but not by the fluid viscosity.
3. *Hydraulically transitional flow* $(5 < \mathrm{Re}^* < 70)$: In this flow, the boundary roughness height is typically equal to the viscous sublayer thickness (Fig. 1.2c). The velocity distributions are dependent on the joint effect of the boundary roughness and the fluid viscosity.

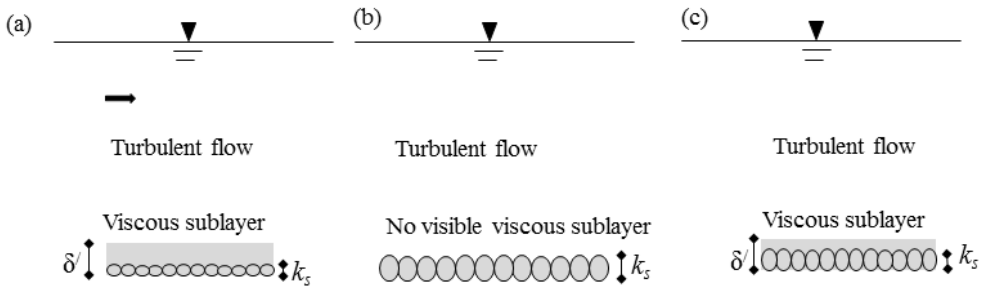

Figure 1.2 Sketch of different flow regimes: a) smooth, b) rough, and c) transition [*Dey*, 2014].

Empirical relationships for the height of different layers are summarized in Table. 1.1.

Table 1.1 Different ranges of viscous sublayer height based on empirical studies.

Author	Year	Height of the viscous sublayer δ'	Height of the inner layer δ_i
Kırkgöz	1989	0.05δ δ -0.14δ	0.5δ -0.6δ
Kundo and Choen	1990	$5\upsilon/u^*$	
Nino and Garcia	1996	$5\upsilon/u^*$	-
ASCE Manual	2005	$11.6\upsilon/u^*$	-

1.2 Introduction to bed-load sediment transport

In nature, many of the changes in river morphology such as bank erosion and bed forms are governed by *bed-load sediment transport* [*Yalin*, 1977; *Dietrich and Smith*, 1984; *Yalin and Ferreira da Silva*, 2001]. In rivers with bed-flow interactions, when the flow-induced shear stress exceeds the threshold of motion *bed-load* transport is initiated. In this type of transport bed particles slide, roll, or travel in sequences of short jumps, known as *saltation* (Fig. 1.3). It is estimated that on average bed-load transport contributes up to 60% of total sediment flux transported in a river especially in gravel bed rivers [*Métivier et al*., 2004; *Meunier et al.*, 2006; *Liu et al*., 2008], the rest correspond to suspended load and is out of the scope of this work.

The variables usually considered to characterize the flow field and transport of sediment are: the fluid density ρ, kinematic viscosity ν, the flow depth H, shear velocity u^*, diameter of particle d and its density ρ_s, bed slope S, gravitational acceleration g, and q_s as the volumetric sediment transport per unit width and time. Using the Buckingham's theorem, the following dimensionless equation can be obtained:

$$q^* = f\left(\tau^*, \mathrm{Re}_s, \Delta, \mathrm{S}, \frac{H}{d}\right) \tag{1.3}$$

Where: $q^* = \dfrac{q_s}{\sqrt{\Delta g d^3}}$ Dimensionless sediment transport rate per unit width (1.4)

$$\tau^* = \frac{u^{*2}}{\Delta g d} \qquad \text{Shields number} \qquad (1.5)$$

$$\mathrm{Re}_s = \frac{\sqrt{\Delta g d^3}}{\nu} \qquad \text{Settling Reynolds number} \qquad (1.6)$$

$$\Delta = \frac{(\rho_s - \rho)}{\rho} \qquad \text{Specific gravity of sediment} \qquad (1.7)$$

Over the past decades, many studies have been devoted to exploring function *f* that best connects q^* to the set of parameters in (1.3). Examples of such works are: theoretical studies of [e.g., *Duboys*, 1879; *Einstein*, 1950; *Bagnold*, 1956; *Ashida and Michiue*, 1973; *Engelund and Fredsoe*, 1976; *Bridge and Dominic*, 1984], experimental works of [e.g., *Meyer-Peter and Müller*, 1948; *Fernandez-Luque and Van Beek*, 1976; *Wong,* 2003; *Recking et al*., 2009] and field data analysis of [*Bagnold*, 1980; *Gomez*, 1991]. A summary of widely cited equations for bed-load transport is given in Table 1.2.

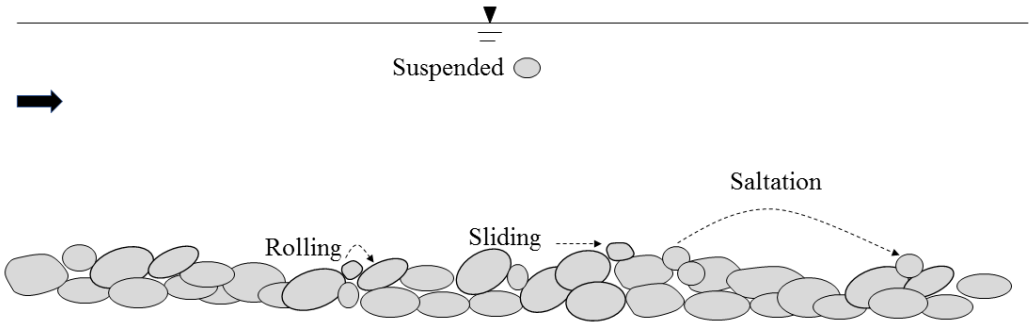

Figure 1.3 Sketch of different sediment transport modes.

Table 1.2 Summary of well-known equations for bed-load transport.

Authors	***Transport rate*** q^*	***Description***
Meyer-Peter and Müller (1948)	$8(\tau^* - \tau^*_c)^{3/2}$	Fit of experimental data
Einstein (1950)	$12 f(\tau^* - \tau^*_c)^{3/2}$	Theoretical origin
Bagnold (1973)	$\frac{\bar{u}}{\mu\sqrt{\Delta g d}}(\tau^* - \tau^*_c)$	Theoretical origin; $\bar{u}$ is the average particle velocity, μ is friction coefficient
Ashida and Michiue (1973)	$17(\tau^* - \tau^*_c)(\sqrt{\tau^*} - \sqrt{\tau^*_c})$	Theoretical origin, and fit of experimental data
Fernandez-Luque and Van Beek (1976)	$5.7(\tau^* - \tau^*_c)^{3/2}$	Fit of experimental data
Engelund and Fredsoe (1976)	$18.74(\tau^* - \tau^*_c)(\sqrt{\tau^*} - 0.7\sqrt{\tau^*_c})$	Theoretical origin
Bridge and Dominic (1984)	$\frac{\alpha}{\mu}(\tau^* - \tau^*_c)(\sqrt{\tau^*} - \sqrt{\tau^*_c})$	Theoretical origin, and fit of experimental data; α is a fitting parameter
Wong (2003)	$3.97(\tau^* - \tau^*_c)^{3/2}$	Fit of experimental data

Despite several equations proposed for bed-load transport, some general features among them are accepted:

1. Many of the proposed relationships (Table 1.2) include a threshold of sediment motion below which the transport does not initiate.
2. For conditions sufficiently far from the threshold, $\tau^* \gg \tau^*_c$, they all except *Bagnold* [1973] predict that $q^* \propto \tau^{*3/2}$. Some studies [e.g., *Meyer-Peter and Müller*, 1948; *Einstein*, 1950; *Fernandez-Luque and Van Beek*, 1976; *Wong*, 2003] predict $q^* \propto (\tau^* - \tau^*_c)^{3/2}$ while others [e.g. *Ashida and Michiue*, 1973; *Engelund and Fredsoe*, 1976; *Bridge and Dominic*, 1984] showed that $q^* \propto (\tau^* - \tau^*_c)(\sqrt{\tau^*} - \sqrt{\tau^*_c})$.

In the recent decades, improvements in measuring techniques have enabled the direct measurement and detailed analysis of motion of bed-load particles (sliding/rolling or saltation).

These measurements can enhance our understanding of particle motion at grain scale as well as mechanism governing the process. Results of these measurements when combined with proper theoretical interpretation can also improve the prediction of bed-load transport models. Most of these works have taken the advantage of image-based methods, which are non-intrusive and can provide high-resolution data. Examples of these techniques can be found in the pioneering studies of *Francis* [1973], *Fernandez-Luque and Van Beek* [1976], *Drake et al*. [1988]. This research line has been continuous up to present date. Example of more recent studies are: *Bottacin-Busolin et al.* [2008], *Radice and Ballio* [2008], *Lajeunesse et al.,* [2010], *Ramesh et al*., [2011], *Roseberry et al*. [2012], *Tregnaghi et al.* [2012 a, b], *Campagnol et al.* [2013], *Julien and Bounvilay* [2013], *Heays et al*. [2014], *Campagnol et al.* [2015], *Fathel at al.* [2015], and *Furbish et al.* [2016].

Investigation of bed-load transport kinematics can be obtained either throughout a Lagrangian approach which explores the motion of individual sediment, or Eulerian approach where several to many particles within a control volume are investigated. In the context of bed-load sediment transport the two approaches correspond to following the trajectories of solid particles [e.g., *Ancey et al.,* 2010; *Lajeunesse et al*., 2010; *Campagnol et al*., 2013; *Heays et al*., 2014; *Fathel et al*., 2015] and to characterizing the sediment transport properties at some place respectively [e.g., *Nelson et al*., 1995; *Böhm et al*., 2004; *Garcia et al*., 2007; *Radice et al*., 2013]. Typically, the Lagrangian approach is mostly used when dispersion of tracer particles comes into play [e.g., *Lisle et al.,* 1998; *Nikora et al.,* 2001 and 2002; *Martin et al*., 2012; *Hassan et al*., 2013; *Ancey and Heyman*, 2014; *Campagnol et al.,* 2015; *Fan et al.,* 2016; *Fathel et al*., 2016], whereas the Eulerian approach is employed for the investigation of sediment fluxes [e.g., *Frey et al.,* 2003; *Singh et al.*, 2009; *Radice et al*., 2009, *Cohen et al*., 2010; *Turowski* 2010; *Furbish et al*., 2012a; *Ballio et al*., 2014].

Dividing the Shields number by the critical shear number (computed using the critical shear velocity u_c^*) and taking the square root of the ratio, (1.3) can be rewritten as:

$$q^* = f\left(\frac{u^*}{u_c^*}, \mathrm{Re}_s, \Delta, \mathrm{S}, \frac{H}{d}\right) \tag{1.8}$$

In this way, the stage value u^*/u_c^* is one of the dimensionless groups of the functional relationship. Investigation of the kinematic properties of moving sediments as a function of these dimensionless parameters has been the core of several studies during the past decades. In this chapter, a general introduction to the Lagrangian and Eulerian kinematic properties of bed-load transport together with the key-findings of previous studies will be given.

1.3 Lagrangian kinematic properties of bed-load moving sediment

1.3.1 Entrainment

When the hydrodynamic forces imposed on the bed of loose sediment exceed the resistance of particle stabilizing forces, particles start to move. This is known as particle entrainment. In fluvial hydrodynamics particle entrainment is the initiating process of sediment transport. Many hydrodynamic changes such as dunes, ripples, erosion and deposition patterns all start with sediment entrainment. The hydrodynamic conditions just enough to initiate a particle motion is the threshold of motion and is an important element in the investigation of bed-load transport. *Shields* [1936] was a pioneer in studying the threshold condition for initiation of motion. He defined entrainment as a deterministic process in which the ratio between driving and stabilizing forces is the governing process of particle entrainment. The semi-theoretical approach proposed by Shields resulted in the first quantitative criterion to define entrainment based on the time averaged boundary shear stress. The deterministic approach was then followed by several other studies in which the incipient motion was theoretically defined by the analysis of the dynamic equilibrium of the forces acting on a grain [see e.g., *Wilberg and Smith*, 1987; *Dey*, 1999, 2003]. After the discovery of the turbulent structures in flow, the role of turbulence on sediment entrainment was highlighted. Several studies [e.g., *Sutherland*, 1967; *Heathershaw and Thorne*, 1985; *Schmid*, 1985; *Papanicolaou et al.*, 2002; *Zanke*, 2003] indicated that high pressure fluctuations induced by burst events have a significant contribution to the entrainment of particles.

In recent decades, with the improvement of measuring techniques particle entrainment was visually studied [*Pilotti et al.*, 1997; *Papanicolaou et al.*, 1999; *Keshavarzy and Ball*, 2000]. However, in order to analyze the experimental measurements, an operative definition of entrainment is necessary to identify when a sediment is effectively entrained and starts moving. The commonly used definition of entrainment for the analysis of experimental data was first suggested by *Drake et al.* [1988] who stated that: "Because some particles in repose vibrated or jostled against their neighbors without going anywhere, we defined entrainment operationally as continuous movement a net horizontal distance of one particle diameter". *Roseberry et al*. [2012] considered a particle entrained, if it does not move back and forth over its stable position. Apparently, this second definition could be less restrictive than the previous one where a minimum distance is required for a particle to be entrained.

1.3.2 Disentrainment

Disentrainment is the counter part of particle entrainment and occurs when fluid-induced forces are not intense enough to keep the particle at motion and thus particle is settled back on the bed to rest. In comparison with the entrainment phase, disentrainment occurs quickly [*Roseberry et al.*, 2012] and this is the reason for the limited studies dealing with the definition of particle distrainment and observing mechanisms governing particle motion during this phase. The image-based study of *Drake et al.* [1988] is likely the first study that analyzed particle settlement. In their investigation particle disentrainment was defined as the "absence of net horizontal motion for 0.25 s or longer that follows displacement". Additionally, they also found that based on the mode of transport disentrainment occurs differently. For sliding and saltating particles, interactions between moving particle and the larger grains settled on the bed cause the settlement whereas considering the rolling ones, particles disentrain mainly due to the decrease of the kinematic energy. However, Drake's criterion, based on the absent time of motion is a subject to question because characteristic scale variable of particle motion is not included in this definition.

1.3.3 Intermediate trajectories

Nikora et al. [2002] proposed a conceptual model for the Lagrangian analysis of particle motion. The model explores three different ranges of scales: the local, intermediate and global range. The local range corresponds to the trajectories between the frequent collisions of a particle with the bed; the intermediate range corresponds to a trajectory bounded by two successive rests (from entrainment to disentrainment), and the global range comprises many intermediate trajectories. Global trajectories are by definition infinite and in practice due to the finite observation size their analysis is not straightforward. The present study primarily focuses on the intermediate (hop) properties of bed-load transport.

Several fundamental studies of Lagrangian quantities, considered in this review are: *Francis* [1973], *Abbot and Francis* [1977], *Niño et al*. [1994], *Lee and Hsu* [1994], *Hu and Hui* [1996], *Niño and García* [1996], *Niño and García* [1998], *Sechet and Le Guennec* [1999], *Ancey* [2002], *Lee et al*. [2000, 2006], *Lajenuesse et al*. [2010], *Ramesh et al*. [2011], *Martin et al*. [2012] and *Campagnol et al*. [2013]. This section starts with the definitions of bed-load kinematic properties. Following that, previous findings regarding each kinematic variable will be discussed.

1.3.3.1 Trajectory length

Fig. 1.4 summarizes the findings of previous studies for the variation of normalized trajectory length L_p / d with stage value u^* / u_c^*. The trajectory of a saltating particle is usually measured as the distance a flying particle travels between two subsequent touches of the bed [e.g., *Hu and Hui*, 1996] whereas for sliding and rolling particles the trajectory is measured as the distance between two successive rests (hop) [e.g., *Campagnol et al*., 2013]. It should be noted that for rolling and sliding conditions, particles have relatively lower velocities compared to the bounding conditions, where a particle impacting the bed may maintain a significant velocity. As indicated in Figure 1.4 in all the experiments the ratio of u^* / u_c^* lies between 0.7-5 with the exception of *Ramesh et al*. [2011] who performed their experiments on a nearly smooth bed, and for conditions relatively higher than the incipient motion (u^* / u_c^* between 6 and 22).

In conclusion, findings of all researchers show a growing trend of the normalized trajectory length with shear velocity. Excluding the results of mixed modes of transport (sl/r/s) from comparison, it is demonstrated that trajectory lengths of saltating particles (labeled as "s" in the legend of Fig. 1.4) are in general longer than those for sliding and rolling particles (labeled as "sl/r"). In fact, rolling and sliding particles are in constant interactions with the bed and thus will be disentrained more quickly than the saltating ones where the interactions with the bed are minimized. Table 1.3 delivers a summary of experimental relationships found for the variation of normalized trajectory length with the stage value.

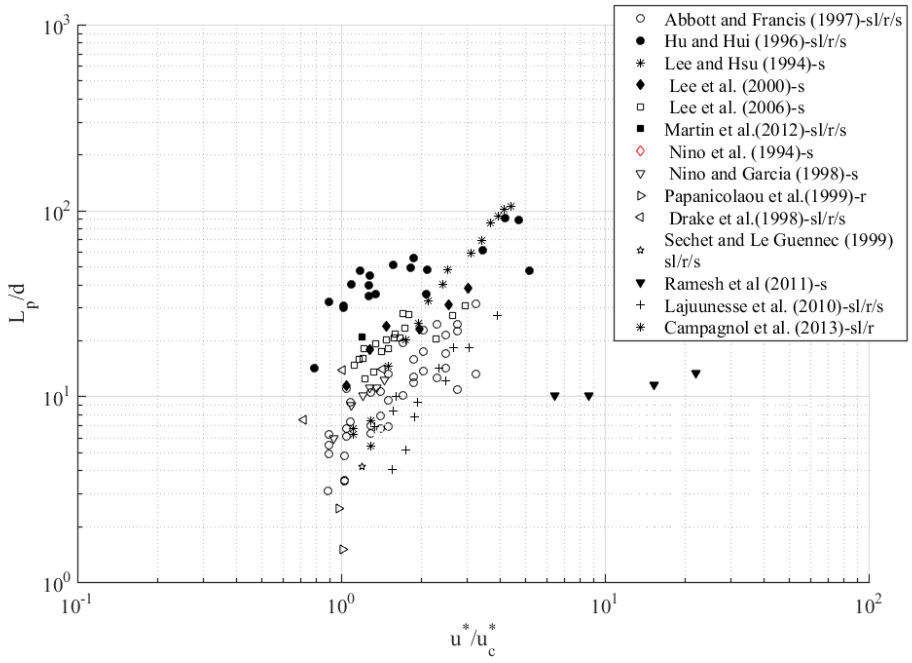

Figure 1.4 Summary of variation of normalized length L_p/d with stage value u^* / u_c^*. The tags next to the author's names indicate the motion mode analyzed in the experimental work: sl – sliding; r – rolling; s – saltating.

1.3.3.2 Trajectory mean velocity

The second property of a trajectory is the mean velocity of a travelling particle within its trajectory V_p. Investigations of normalized velocity V_p / u^* as a function of stage value are

illustrated in Fig.1.5. An increasing trend (a power law with different exponents) was found for the variation of particle velocity with stage value. The measurements also indicated that the velocity of saltating particles is higher than those with sliding or rolling modes of transport. As enlightened for trajectory length this is due to the fact that saltating particles move at a distance from the bed which prevents them from subsequent interactions with the bed and thus particles move faster.

Concerning the nature of the bed, Fig. 1.5 demonstrates that in experiments performed with fixed bed [e.g., *Hu and Hui*, 1996; *Nino and Garcia*, 1996; *Abbot and Francis*, 1997] particles are in general associated with higher velocities compared to the experiments conducted over an erodible bed [see e.g., *Lajeunesse et al*., 2010; *Ramesh et al*., 2011]. In a detailed analysis *Lajeunesse et al*. [2010] calculated the coefficient of velocity for particles moving over a mobile bed and compared the results with the fixed bed data of *Abbot and Francis* [1977] and *Lee and Hsu* [1994] and concluded that particles move faster over a fixed bed.

Different relationships for the variation of trajectory averaged velocity as a function of shear velocity are also summarized in Table 1.3.

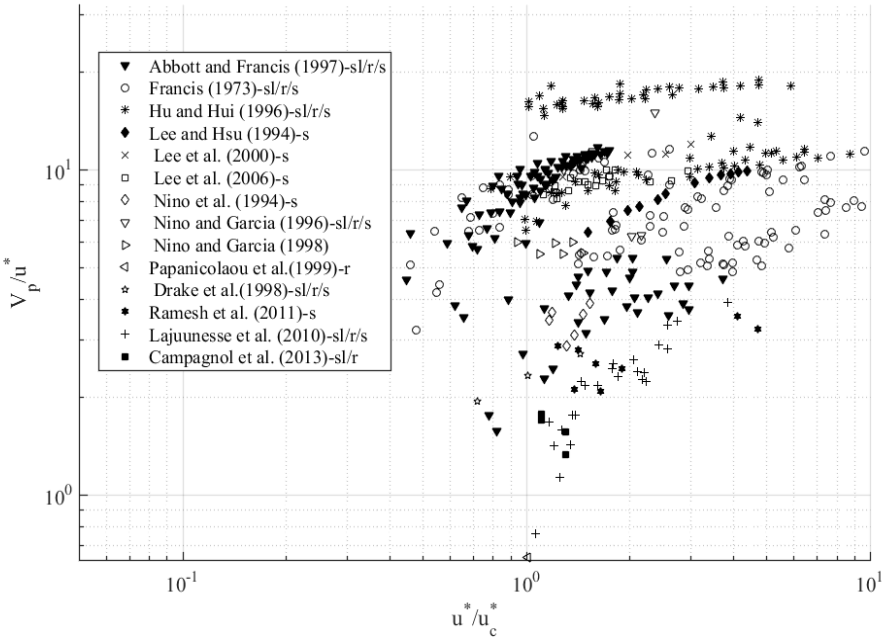

Figure 1.5 Summary of variation of normalized velocity (V_p / u^*) with stage value u^* / u_c^*.

Table 1.3 Summary of derived relationships for trajectory length and average velocity.

Authors	L_p/d	V_p/u^*
Francis (1973)	-	Dependency with u^*/u_{cr}^*
Abbot and Francis (1977)	Dependency with u^*/u_{cr}^*	$\frac{V_p}{u^*} = a\left[1-\left(\frac{u^*}{u_{cr}^*}\right)^{-1}\right]$ $a = 13.4-14.3$
Lee and Hsu (1994)	$\frac{L_p}{d} = 196.3\Phi_{cr}^{0.788}\left[\left(\frac{u^*}{u_{cr}^*}\right)^2-1\right]^{0.788}$	$\frac{V_p}{u^*} = 11.53\Phi_{cr}^{0.174}u_{cr}^*\left[\left(\frac{u^*}{u_{cr}^*}\right)^2-1\right]^{0.174}$
Niño et al. (1994)	$\frac{L_p}{d} = 2.3\left(\frac{u^*}{u_{cr}^*}\right)^2$	$\frac{V_p}{u^*} = a\left[1-\left(\frac{u^*}{u_{cr}^*}\right)^{-1}\right]$ $a = 6.8-8.5$
Niño and García (1998)	Dependency with Re_s and u^*/u_{cr}^*	-
Hu and Hui (1996)	Smooth bed: $\frac{L_p}{d} = 76.74\Phi_{cr}^{0.86}\left(g\frac{\rho_s}{\rho}\right)^{0.70}\left(\frac{u^*}{u_{cr}^*}\right)^{1.72}$ Rough bed: $\frac{L_p}{d} = 27.54\Phi_{cr}^{0.90}\left(g\frac{\rho_s}{\rho}\right)^{0.94}\left(\frac{u^*}{u_{cr}^*}\right)^{1.80}$	Smooth bed: $\frac{V_p}{u^*} = 19.5-5.1\left(\frac{u^*}{u_{cr}^*}\right)^{-1}$ Rough bed: $\frac{V_p}{u^*} = 11.9-5.2\left(\frac{u^*}{u_{cr}^*}\right)^{-1}$
Lee et al. (2000, 2006)	Dependency with Re_s and u^*/u_{cr}^*	Dependency with Re_s and u^*/u_{cr}^*
Lajeunesse et al. (2010)	$\frac{L_p}{d} = (70\pm2)\frac{(u^*-u_{cr}^*)}{V_s}$	$\frac{V_p-V_c}{V_s} = a\frac{(u^*-u_{cr}^*)}{V_s}$ $a = 4.4\pm0.2,\ \ V_c/V_s = 0.11\pm0.03$
Ramesh et al. (2011)	Dependency with u^*/u_{cr}^*	Dependency with u^*/u_{cr}^*
Campagnol et al. (2015)	Dependency with u^*/u_{cr}^*	Dependency with u^*/u_{cr}^*

1.3.3.3 Time of motion and time of rest

Bed-load transport is an intermittent process governed by sequences of alternating motion and stillness periods. Unlike several studies conducted for the trajectory length and its mean velocity, there is limited literature on the analysis of time of motion and rest. *Papanicolaou et al*. [1999]; *Martin et al.* [2012], and *Campagnol et al*. [2013] were possibly among the first studies who presented their results of trajectory duration. Regarding the measurements of particle rest, *Niño and García* [1998] is probably one of the few studies in which the time elapsed between sediment disentrainment and entrainment was measured. A summary of previous investigations of normalized time of motion and rest ($t^m u^*/d$ and $t^r u^*/d$, respectively) as a function of u^*/u_c^* is given in Fig. 1.6. A clear trend for the variation of time of motion with shear velocity is not observed in Fig. 1.6a. On the other hand, *Niño and García* [1998] found that for jumping grains the mean value of normalized time of rest is between 10 and 20 when u^*/u_c^* changes from 0.95 to 1.16. The normalized value of time of rest is shown to be falling as u^*/u_c^* increases (Fig. 1.6b). They also explored that the measured standard deviation of t^r was very high, lying between 80-112% of the mean resting time and decreasing as the values of shear velocity grew.

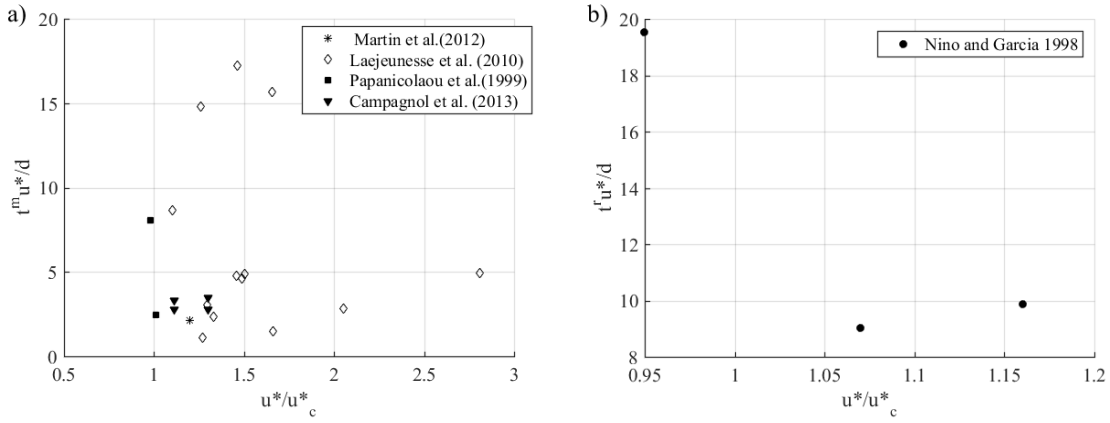

Figure 1.6 Summary of variation of normalized a) time of motion and b) time of rest with u^*/u_c^*.

1.4 Eulerian bed-load transport kinematics

In the recent decades, increasing attention has been paid to the phenomenological aspects of bed-load sediment transport by shifting from large to grain scales to offer an insight into the mechanics of particle entrainment and transport fluxes.

1.4.1 Entrainment and disentrainment rates

An entrainment/disentrainment rate can be operationally determined by assessing if one or more particles have been entrained/disentrained from a certain area within a certain time interval [e.g., *Van Rijn*, 1984; *Cao*, 1997]. Entrainment/disentrainment rates (calculated as the total number of entrainment/disentrainment events within constant spatial and temporal domains) are on one hand related with suitably chosen control volumes and are therefore Eulerian quantities. On the other hand, they are related with particle start and stop; therefore, these rates could be computed only provided that each grain was individually tracked. Measurements were thus conducted in a Lagrangian way, but data on single particle motion were averaged using appropriate spatial and temporal support scales to obtain values for the Eulerian quantities of interest.

1.4.2 Solid discharge

Understanding and providing quantitative prediction of sediment fluxes in river streams stand at the core of sediment transport studies and engineering practices. In spite of various studies during the past decades, due to the complexity of the process there are still huge uncertainties in the estimation of sediment transport rate. Typically, bed-load sediment transport rate is empirically correlated with near bed shear velocity. A comprehensive review by *Chanson* [1999] explores several equations that have been proposed for the prediction of the sediment transport rate (see examples in Table 1.2). An example of a pioneering work regarding this approach is *Meyer-Peter and Müller* [1948] who estimated the sediment fluxes

as a function of bed shear stress. As indicate earlier in Table 1.2 the shortcoming of this method is that the relationships found by different researchers sometimes result in sediment fluxes different by an order of magnitude.

Particle visualization at small scales motivated several researchers to separate and individually investigate the key components that contribute to the sediment transport. Some [e.g., *Beek*, 1976; *Wiberg and Smith*, 1987; *Hu and Hui*, 1996b; *Lee et al*., 2000; *Garcìa et al*., 2000; *Seminara et al*., 2002; *Parker et al*., 2003; *Radice et al*., 2006, 2010a; *Ballio and Radice,* 2007; *Radice and Ballio*, 2008] studied bed-load sediment flux as the product of the areal concentration of sediments and of the grain velocity.

On a horizontal basis, the quantities are averaged over a reference bed area *A*, and then bed-load transport is calculated as:

$$q_s = C_A v_A d_{50} \tag{1.9}$$

Where C_A and v_A are the areal concentration and the areal average velocity of moving particles and d_{50} is the representative particle diameter.

1.4.2.1 Particle concentration and particle velocity

Radice and Ballio [2008] investigated the double-average characteristics of sediment flux in one-dimensional bed-load transport and studied the variations of double average concentrations and velocities with stage values. Results of the cited work suggest that concentration once correlated with shear velocity is more variable than the velocity (Fig. 1.7). In a detailed analysis, *Radice et al*. [2009], studied the scaling analysis of moments of statistics for sediment concentration and showed that the mean value of concentration is scale invariant whereas the standard deviation decreases with larger support scales. They provided a mathematical derivation for the trend of variance and revealed that deviation from the trend is best explained by the spatial correlation. Results of scale dependency are presented in Fig. 1.8.

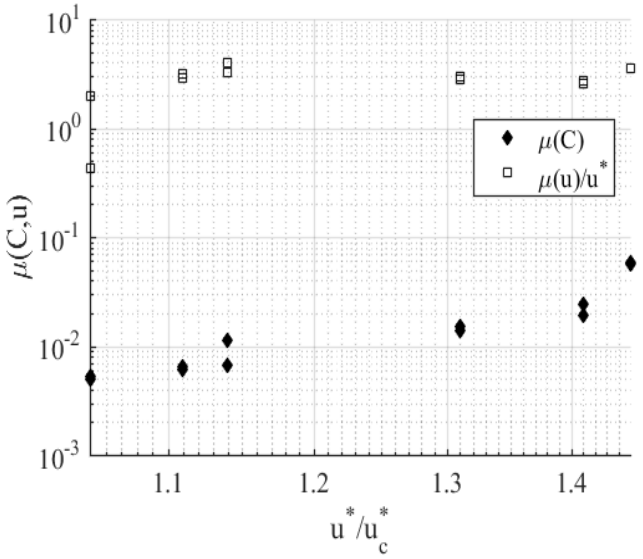

Figure 1.7 Variation of the mean values of concentration and normalized particle velocity with u^* / u_c^* [*Radice and Ballio*, 2008].

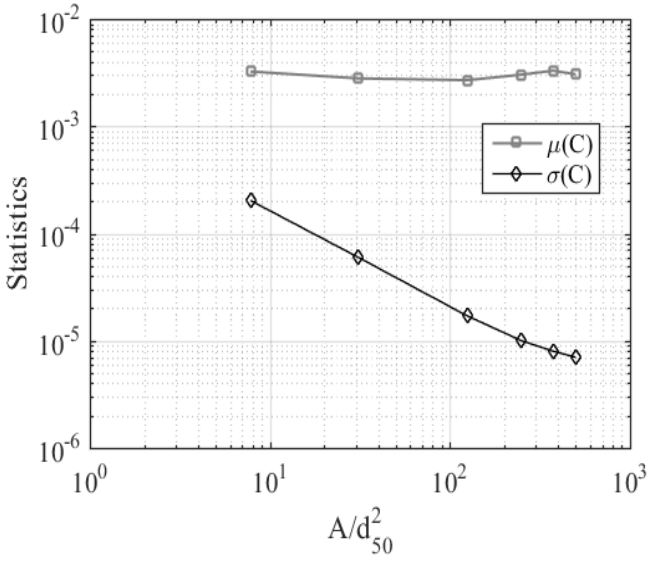

Figure 1.8 Scale dependence of mean and standard deviation of concentration [*Radice et al*. 2009]. *A* represents the scale of observation.

1.5 Discussion

Functional parameters involved in semi-empirical relationships for bed-load transport were studied in this chapter. A comparison among different experimental studies indicates that in general, higher values of stage result in longer travel distances between entrainments and disentrainments with an increase in trajectory velocities. It was shown that any growth in the shear velocity on the other hand, will decrease the particle's resting time. Regarding the structure of the bed, experimental results indicated that velocity of particles moving over a fixed bed are higher than those over a mobile bed.

Form a Eulerian point of view, scholars studied the main components of solid discharge (concentration and velocity) and investigations showed that the concentration of particles is more variable with shear velocity than the other component i.e. velocity of moving sediments. The average values of these quantities were also shown to be invariant of the spatial scale.

Chapter 2 Conceptual framework

2.1 Introduction

As shown earlier in chapter 1, in spite of numerous studies dealing with Lagrangian and Eulerian bed-load kinematics, the lack of a general framework with univocal definitions of Lagrangian and Eulerian bed-load indicators is noticed. The existence of such framework helps to pile new findings instead of placing them side by side.

Ballio et al. [2017] introduced a novel universal framework for the description and analysis of bed-load kinematics. In the proposed framework; (i) the sediment kinematics are described taking both the Lagrangian and the Eulerian approach, (ii) a set of relevant indicators is defined using various averaging methods and (iii) conceptual relationships among the key quantities are determined.

Accounting for this framework, definitions and measurements of several quantities whose analysis have been already discussed (see sections 1.3 and 1.4) will be presented. From an operational point of view, the definitions and relationships presented in the framework are useful for analysing/interpreting results from experiments with bed-load sediment transport. As will be shown in the following chapters, this framework will be applied to experiments conducted in this study and subsequently Lagrangian and Eulerian bed-load kinematics will be investigated for a range of experiments with different stage values.

2.2 General hypothesis

This framework considers the transport of identical grains as one-dimensional bed load. These grains represent an arbitrary sample from the population of all the sediment involved in the process. For the sake of simplicity, grains are assumed to move only in the positive streamwise

x direction and all the properties of a particle (mass, volume, velocity, …) are attributed to its center of mass. The fundamental starting quantity is the time history of particle velocity, from which most of the variables commonly used in bed-load studies are derived. Lagrangian description of bed-load is based on the kinematics of individual particles; values are then integrated/averaged in space for the Eulerian description over a control volume.

2.3 Lagrangian description

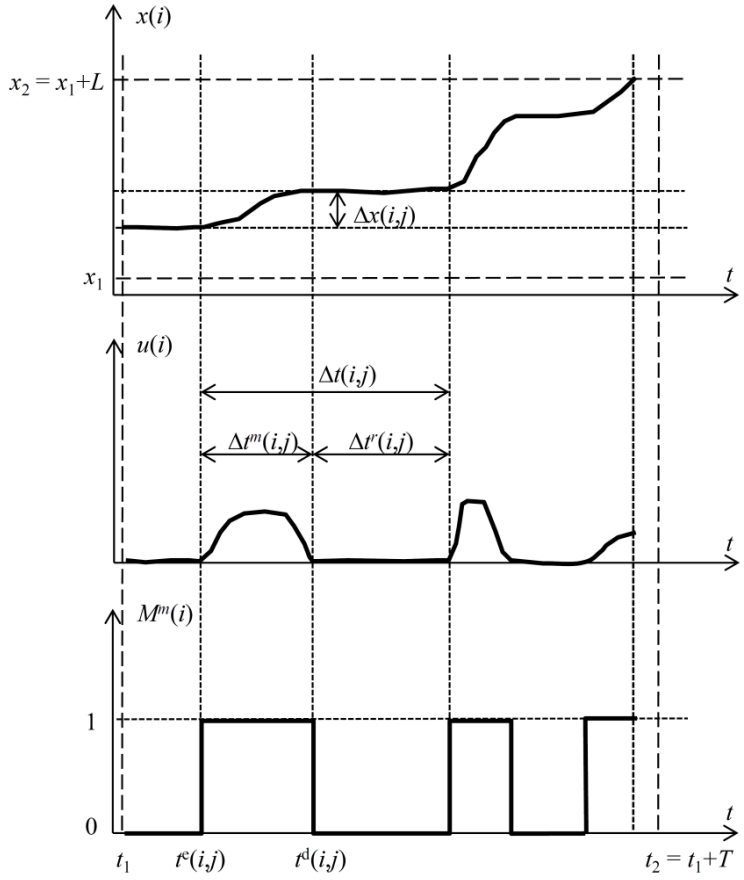

Figure 2.1 Conceptual description of an *i*-th particle path by its position (x), velocity (u) and clipping function for motion (M^m). Properties of a *j*-th event (time of motion and rest, total duration, displacement length, instants of entrainment and disentrainment) are sketched. The long-dash lines mark an Eulerian observation window.

An individual particle is denoted with *i* and the total number of particles in the sample is *N*.

The streamwise position of a particle at any time t is denoted with $x(i,t)$. For the i-th particle one can identify a succession of alternating periods of motion and rest. A single period of motion followed by a single period of rest together form an 'intermediate event' (hop) (Fig. 2.1). $J(i)$ indicates the total number of events in the observed history of the particle. The duration of the j-th event for the i-th particle is $\Delta t(i,j)$, and it can be further split into duration of motion and stillness, $\Delta t^m(i,j)$ and $\Delta t^r(i,j)$, respectively. Similarly, $\Delta x(i,j)$ represents the displacement of a particle i during an event j, which is known as 'hop length'.

Since at any instant, particle i may or may not be in state of motion, it is convenient to introduce a 'clipping function' M^m to quantify a particle state as:

$$M^m(i,t)=\begin{cases}1 & \text{if particle is moving}\\ 0 & \text{if particle is not moving}\end{cases} \tag{2.1}$$

The clipping function M^m can be expressed as:

$$M^m(i,t)=\sum_j\left[\mathrm{H}\left(t-t^{\mathrm{e}}(i,j)\right)-\mathrm{H}\left(t-t^{\mathrm{d}}(i,j)\right)\right] \tag{2.2}$$

where $t^{\mathrm{e}}(i,j)$ and $t^{\mathrm{d}}(i,j)$ identify the instants of entrainment (pickup) and disentrainment (deposition), respectively, for an event j, and H( ) is the Heaviside step function. (An example of a temporal evolution of M^m is shown in Fig. 2.1. The time derivative of $M^m(i,t)$ is therefore:

$$\frac{\mathrm{d}M^m(i,t)}{\mathrm{d}t}=\sum_j\delta\left(t-t^{\mathrm{e}}(i,j)\right)-\sum_j\delta\left(t-t^{\mathrm{d}}(i,j)\right)=e(i,t)-d(i,t), \tag{2.3}$$

where δ is a Dirac delta function that can be used to define $e(i,t)$ and $d(i,t)$, i.e., entrainment and disentrainment functions, respectively. The total time of motion for a particle i during period T, is defined as $T^m(i)$. Alternatively, 'intermediate' quantities can be used to express $T^m(i)$ as:

$$T^m(i)=\sum_{j=1}^{J(i)}\Delta t^m(i,j). \tag{2.4}$$

The total time of rest for the particle i during T is then:

$$T^r(i)=\sum_{j=1}^{J(i)}\Delta t^r(i,j) \tag{2.5}$$

Assuming that T is large enough to disregard truncated periods of motion/rest at the beginning and at the end of the time window, it follows that for each particle i:

$$T(i)=T^m(i)+T^r(i) \tag{2.6}$$

The corresponding relative time spent in motion, (herein also defined as porosity) $\varphi_T^m(i)$, (= time spent in motion/total observation time) is:

$$\varphi_T^m(i)=\frac{T^m(i)}{T}=\overline{M^m(i,t)} \tag{2.7}$$

One can also define an instantaneous relative number of particles in motion, $\varphi_N^m(t)$, (= number of moving particles/total number of observed particles), as:

$$\varphi_N^m(t)=\frac{N^m(t)}{N}=\frac{\sum_{i=1}^{N}M^m(i,t)}{N} \tag{2.8}$$

2.4 Eulerian description

Consider a reference plan area A extending between two x-locations x_1 and $x_2 = x_1+L$ (Fig. 2.2).

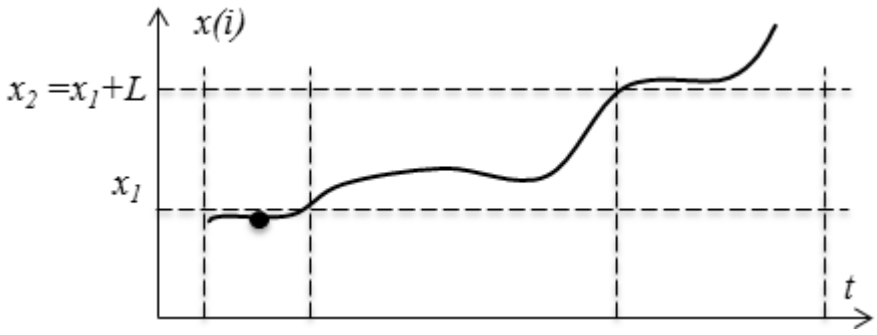

Figure 2.2 Sketch of a particle moving through the reference plan area A of the bed (bounded by x_1 and x_2).

To identify whether a particle i is within the reference area A, a Eulerian clipping function is defined as:

$$M^A(i,t)=\begin{cases}1 & \text{if particle is within } A \text{ at time } t\\ 0 & \text{if particle is not within } A \text{ at time } t\end{cases} \tag{2.9}$$

The total number of particles within A at time t is expressed as:

$$N_A(t)=\sum_{i=1}^{N} M^A(i,t) \tag{2.10}$$

and the number of particles within A that are in motion at time t as:

$$N_A^m(t)=\sum_{i=1}^{N} M^A(i,t)\ M^m(i,t)=\sum_{i=1}^{N_A(t)} M^m(i,t) \tag{2.11}$$

The number of particles at rest within A at time t is:

$$N_A^r(t)=\sum_{i=1}^{N} M^A(i,t)\ \left(1-M^m(i,t)\right)=\sum_{i=1}^{N_A(t)} \left(1-M^m(i,t)\right) \tag{2.12}$$

Subsequently, the concentration of moving/still sediments over a certain near-bed area A at each instant are defined as:

$$C_A^m(t)=\frac{N_A^m(t)\,w}{Ad},\ C_A^r(t)=\frac{N_A^r(t)\,w}{Ad} \tag{2.13 and 2.14}$$

Where d is particle diameter and w is the volume of a single particle. In a time series, Eulerian velocity at instant t is calculated by averaging the values of instantaneous velocity of all moving particles within A:

$$u_A^m(t)=\{u^m\}_A \tag{2.15}$$

2.4.1 Eulerian variables: sediment discharge

As shown earlier (1.9), Eulerian sediment fluxes can be calculated from the concentration and velocity of moving particles, the calculation of solid discharge within the framework is then:

$$q = \overline{C_A^m(t) u_A^m(t) d} \tag{2.16}$$

(2.16) is a purely Eulerian quantity.

2.4.2 Eulerian variables: sediment discharge passing a transverse line

Consider again the reference plan area A in Fig. 2.2 with the transverse line x_{tl} (Fig. 2.3). To verify whether a particle i passes this line within Δt, a clipping function is introduced as:

$$M^{tl}(i,t) = \begin{cases} 1 & \text{if } x(i,t) > x_{tl} \text{ and } x(i,t-\Delta t) < x_{tl} \\ 0 & \text{otherwise} \end{cases} \tag{2.17}$$

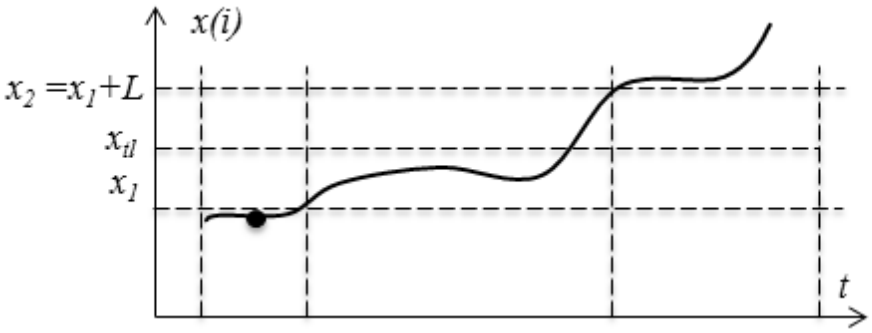

Figure 2.3 Sketch of a particle moving through the reference plan area A of the bed (bounded by x_1 and x_2) A. x_{tl} represents a transverse line perpendicular to the flow direction.

Therefore, the total number of particles that pass the reference line can be expressed as:

$$N_A^{tl}(t) = \sum_{i=1}^{N} M^A(i,t)\ M^{tl}(i,t) = \sum_{i=1}^{N_A^{tl}(t)} M^{tl}(i,t) \tag{2.18}$$

Sediment flux across this line can be alternatively computed for any given Δt as:

$$q = \frac{N_A^{rtl}(t)w}{l_r \Delta t} \tag{2.19}$$

Where l_r is the length of the reference line in the transverse direction.

Averaging options

The definitions presented above will be used to derive more information relevant for the relationships between Lagrangian and Eulerian description of sediment motion. This is achieved through various forms of averaging or filtering, which are applied to overcome the key issue of a spatial mismatch between the two descriptions (i.e. Lagrangian is pointwise, but moving; Eulerian is referred to a finite fixed spatial domain, thus involving spatial averaging/regularization). Therefore, the following options are available:

Event averaging yields properties of motion of a single grain at the scale of individual hops:

$$\langle \theta \rangle = \frac{1}{J} \sum_{1}^{J} \theta(j) \tag{2.20}$$

Time averaging provides regularized / integrated properties of motion of a single grain or a set of grains and thus smoothes temporal fluctuations:

$$\bar{\theta} = \frac{1}{T} \int_{t}^{t+T} \theta(t) \mathrm{d}t \tag{2.21}$$

Sample averaging yields quantities that are averaged over a set of individual particles:

$$\{\theta\} = \frac{1}{N} \sum_{i=1}^{N} \theta(i) \tag{2.22}$$

$$\{\theta\}_A = \frac{1}{N_A} \sum_{i=1}^{N_A} \theta(i) \tag{2.23}$$

In the above equations θ is a general quantity which may be associated with a time instant *t*, a particle *i*, and a motion event *j*. Furthermore, square brackets [θ] will be used to denote an expected value obtained by averaging over a large number of statistical realisations (ensembles). In ideal (uniform, stationary and ergodic) conditions, when the spatial and temporal windows and the number of ensembles are sufficiently large, all averaging options should produce identical statistics. However, experimental conditions always impose limitations (small averaging area, short observation time) and therefore results are filtered rather than being averaged quantities (the magnitude of a filtered quantity depends on the size of the averaging window). In such conditions, temporal and sample averaging may be used to complement each other, i.e. to increase the number of ensemble realisations and hence produce a better estimate of the expected values compared to what either of them would do on its own. Temporal and sample averaging can be considered together, and assumed to produce a single sample from the general population. A sufficiently large set of such samples yields the statistics for the general population, i.e. expected values.

Using the arguments above, the expected value of the relative duration of motion (i.e. porosity for movement) is:

$$\vartheta^m = \left[M^m(i,t) \right]. \tag{2.24}$$

If the process is uniform in space and time (and ergodic) one can think that, for large *T* and large *N*, both time porosity and sample porosity converge to the expected value, i.e.

$$\varphi_T^m = \varphi_N^m = \vartheta^m. \tag{2.25}$$

However, this is often difficult to achieve, so one can operationally combine time and sample averaging to make convergence quicker. Sample average of time porosity and time average of sample porosity converge, for sufficiently large *T* and *N*, to the expected value of porosity:

$$\left\{ \varphi_T^m \right\} = \overline{\varphi_N^m} = \vartheta^m \tag{2.26}$$

The expected porosity for movement gives the ‘large scale’ information about the particles’ activity, i.e. the percentage of time, on average, that particles spend in motion. In typical laboratory conditions, this porosity is difficult to measure because any particle is observed for

a limited (in space and time) portion of its trajectory. From a Eulerian perspective, one is interested in describing the state of motion within the reference area A. Therefore, relative number of moving particles within the reference area A is $\varphi_A^m(t)$, (=number of moving particles within A/total number of particles within A):

$$\varphi_A^m(t)=\frac{N_A^m(t)}{N_A(t)} \tag{2.27}$$

2.4.3 Entrainment / disentrainment

Derivation of Eulerian entrainment and disentrainment functions, $E(t)$ and $D(t)$, from their Lagrangian counterparts is analogous to that presented for a number of particles in motion over A:

$$E(t)=\sum_{i=1}^{N} M^A(i,t)e(i,t)=\sum_{i=1}^{N_A(t)} e(i,t)=\sum_{i=1}^{N_A^r(t)} e(i,t) \tag{2.28}$$

$$D(t)=\sum_{i=1}^{N} M^A(i,t)d(i,t)=\sum_{i=1}^{N_A(t)} d(i,t)=\sum_{i=1}^{N_A^m(t)} d(i,t) \tag{2.29}$$

Note that summing of $e(i,t)$ over either N_A or $N_A{}^r$ gives the same result since an already moving particle cannot be entrained. For an analogous reason summing of $d(i,t)$ over either N_A or $N_A{}^m$ yields identical results. Temporal evolutions for E and D will be discontinuous, analogously to those for e and d described above. If previous definitions are averaged in time one obtains:

$$\overline{E}=\sum_{i=1}^{N}\overline{M^A(i,t)e(i,t)}=\overline{\sum_{iA=1}^{N_A(t)} e(i,t)}=\overline{N_A(t)\{e(i,t)\}_A}=\overline{N_A^r(t)\{e(i,t)\}_A^r} \tag{2.30}$$

$$\overline{D}=\sum_{i=1}^{N}\overline{M^A(i,t)d(i,t)}=\overline{\sum_{iA=1}^{N_A(t)} d(iA,t)}=\overline{N_A(t)\{d(i,t)\}_A}=\overline{N_A^m(t)\{d(i,t)\}_A^m} \tag{2.31}$$

In the limit of big samples / long times T / uniformity condition where we can assume all trajectories to have the same time averages: $\bar{e}=1/\langle\Delta t\rangle=1/\tau$, we simply obtain the intuitive result:

$$\overline{E}=N_A\bar{e}=\frac{N_A}{\tau} \tag{2.32}$$

2.4.4 Eulerian variables: Einstein-type sediment discharge

Suppose that λ is the distance travelled by one particle within T. Under the condition of uniformity / long time / big samples the relationship between the sediment discharge and the Lagrangian variables is linked to the already derived relations:

$$\frac{[\lambda]}{T}=\frac{[J\langle\Delta x\rangle]}{[J\langle\Delta t\rangle]}=\frac{[\langle\Delta x\rangle]}{[\langle\Delta t\rangle]}=\frac{\xi}{\tau} \tag{2.33}$$

(note that J is constant under the above conditions). At the end, we obtain:

$$q=w\frac{N_A}{A}\frac{[\lambda]}{T}=w\frac{N_A}{A}\frac{\xi}{\tau}=w\frac{N_A}{A}\bar{e}\xi=\frac{w}{A}\overline{E}\xi \tag{2.34}$$

which is the typical Einstein-type formulation for sediment discharge.

2.5 Bridge between approaches

As discussed above, the proposed framework enabled the quantification of several Lagrangian and Eulerian indicators at simple deterministic levels. It is however, important to mention that the two approaches complement each other, as they provide alternative descriptions of the process. For example, let one consider the sediment transport rate: it has been expressed in a fully Eulerian form as proportional to a bed-load sediment concentration and a sediment velocity (2.16) or in a Lagrangian-Eulerian form as proportional to a Eulerian entrainment rate and a Lagrangian hop length (2.34). A link between the approaches and conditions of equivalence for expressions 2.16 and 2.34 will be verified in the coming chapters when the framework will be applied to a series of experimental data.

Chapter 3 Experiments

3.1 Introduction and facilities

The experiments for the current study were conducted in a pressurized duct at the Hydraulic Engineering Laboratory of the Politecnico di Milano, Milan, Italy. The channel length is 5.8 m, while the rectangular cross section is 0.4 m wide and 0.11 m high. A fixed-rough bed was employed by gluing two layers of sediment particles onto steel plates. A comparison of this fixed bed with a movable bed of the same material indicated the standard deviation for the bed elevation (representing bed roughness) was almost identical in both types of bed [*Campagnol et al*., 2015]. Uniform quasi-spherical Polybutylene Terephthalate grains (identical to the glued ones) with the dimension d = 3 mm and a density $\rho_g = 1.27 \times 10^3\ kg/m^3$ were used for the experiments. For a better particle tracking, the entire bed was painted in black, while the bed-load grains released into the channel were white (Fig. 3.4). A transparent lid covered the entire channel to eliminate picture distortion that could have been caused by a wavy free surface. The coverage of the flume resulted in a fully pressurized system. However, several studies [e.g., *Ettema*, 2008; *Radice*, 2009] confirmed that sediment transport mechanics does not significantly change as the flow becomes pressurized. Particle motions were recorded using a CCD camera installed on top of the flume. The constant flow discharge during each experiment was measured using a magnetic flowmeter attached to the pipe next to upstream tank (Fig. 3.1) and to regulate the entering flow, some tube sheets were installed at the duct inlet. A pipe transferred the water from the outlet into the inlet tanks in a closed loop. Experiments were performed for a range of discharges from Q=12.1-23.1 l/s. In total, 18 experiments were carried out.

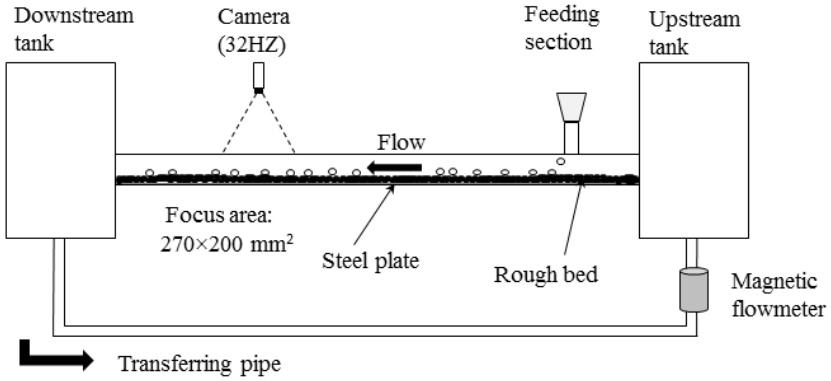

Figure 3.1 Sketch of experimental apparatus.

3.2 Characterization of bed surface structure and velocity measurement

3.2.1 Measurements of bed elevation, tools and operative procedure

In general, the bed surface can be described as an area consisting of continuous random bed elevations $z = f(x, y, t)$ where x and y are longitudinal (main flow direction) and transverse coordinates, and t is the time. In the presence of a fixed-bed, the elevation is independent of time and is thus only a function of x and y position: $z = f(x, y)$. A Laser Distance Sensor was used to measure z_V as the vertical distance between the bed surface and the laser and subsequently derive the bed elevation fluctuations. The device sends a pulse of laser light to the target and measures the electric voltage of the received signal V (Fig. 3.2). The voltage depends on the distance between the target and the receiver as well as the property of the environment through which the light passes. It is worth mentioning that, the device should be calibrated before any new application. To measure bed elevation z_b a dry bed was used and the beam emitted by the laser distance sensor crossed just air. The calibration procedure was performed placing an object at a fixed increasing distance from the beam source and measuring the respective values of V. Tested distance ranged between 100 to 150 mm and it was increased with a spatial lag of 5 mm. The equation for the voltage to distance was then found as:

$$z_v = 39.53677V + 103.26224 \quad (3.1)$$

After laser calibration, the beam was installed on top of the flume and vertical distances z_v and subsequently bed elevation $z_b = D - z_v$ (Fig. 3.3) was measured over a 50 mm long by 35 mm wide test section (Fig. 3.4). Measurements were performed along streamwise lines (L_1- L_8) with the resolution of 1 mm and spacing of 5 mm in the transverse direction corresponding to a total of 408 measured points (Fig. 3.4). The job was done manually by fixing the *y* position and shifting the laser distance sensor along the streamwise lines (L_1- L_8). An example of z_v measurements along the streamwise axis (L_4) is given in Fig. 3.5. A three-dimensional sketch of bed elevations for the test section is given in Fig. 3.6.

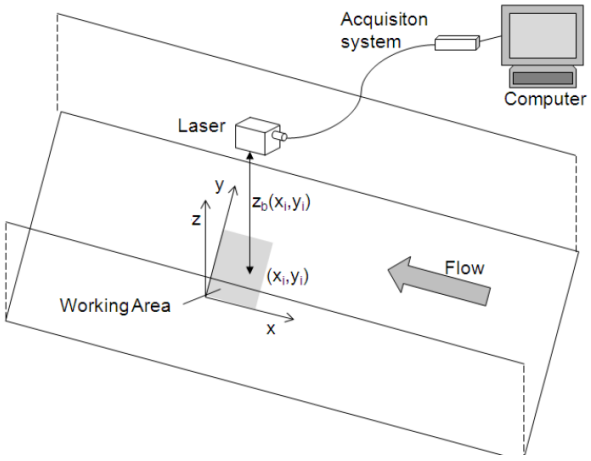

Figure 3.2 Application of Laser Distance Sensor for bed elevation measurements.

Second to forth-order moments of statistics can provide necessary information to characterize the bed surface. The standard deviation of the elevations $\sigma(z_b)$ indicates the range of fluctuations of bed elevation and is a measure of the vertical roughness scale [see *Nikora et al.*, 1998; *Heritage and Milan*, 2009; *Coleman et al.*, 2011]. Skewness $S_k(z_b)$ can be used to assess the general shape of the bed surface. A positive skewness (S_k >0) shows that in general

measurements of bed elevation are higher than $\sigma(z_b)$ whereas the opposite prevails for S_k <0. Finally, kurtosis $K_u(z_b)$ provides the degree of the regularity of the bed structure. In other words, high values of kurtosis indicate that there are sporadic values of z_b very different from the mean. For the measurements performed here, the standard deviation was computed as 1.28 mm slightly less than half a particle size. The negative value of skewness (S_k=-0.19) shows that values of z_b smaller than the average value of bed elevation are more probable. The computed value of kurtosis, K_u=3.2 represents the sporadic presence of relatively high values in the measurements of bed elevation.

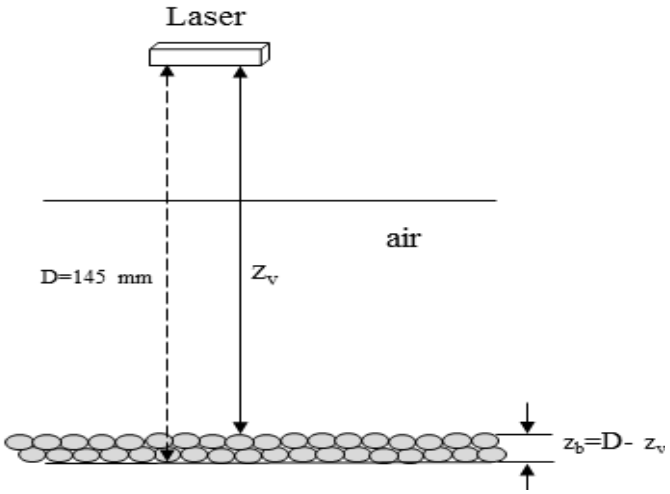

Figure 3.3 Sketch of vertical distance z_b measurements.

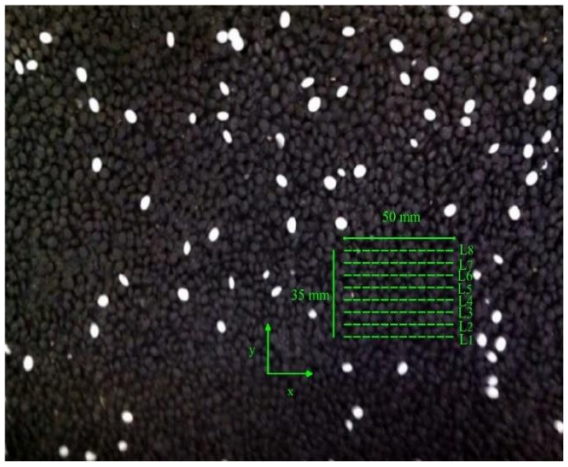

Figure 3.4 Test section 50 mm × 35 mm for bed elevation measurements.

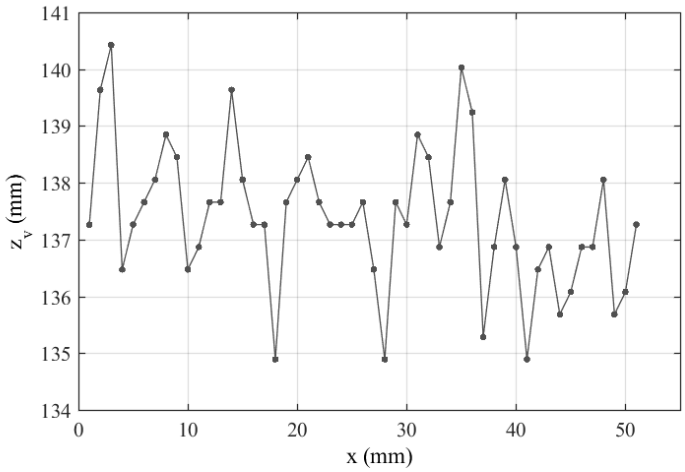

Figure 3.5 Example of vertical distance z_v measurements (L_4).

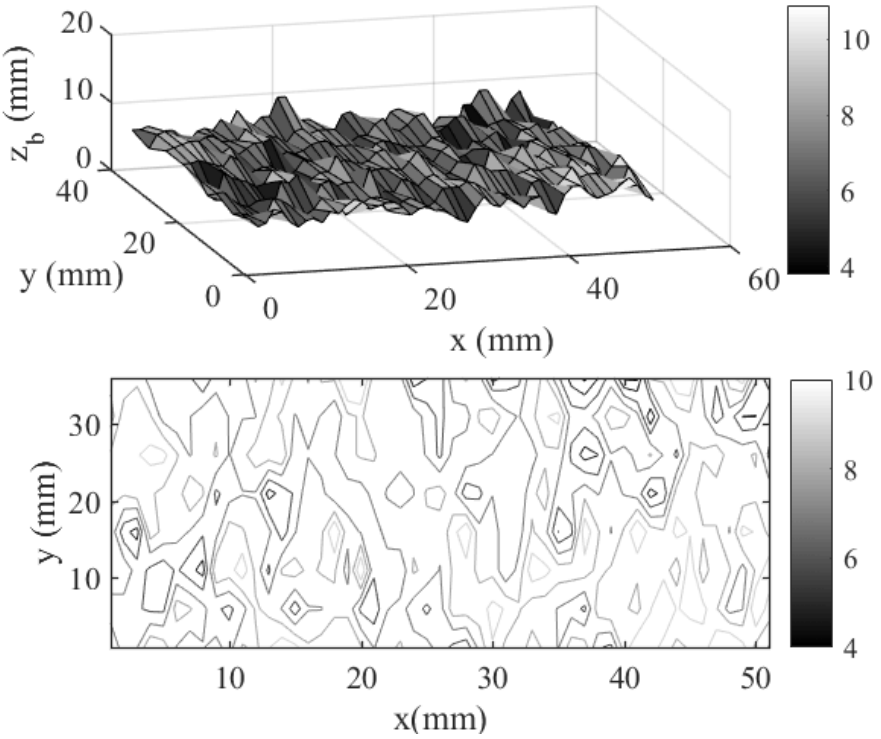

Figure 3.6 Bed survey test section 50 mm × 35 mm.

3.2.2 Time-averaged velocity profiles

Two ultrasonic velocity profilers (UVP) with 81° orientation were used to measure vertical profiles of instantaneous streamwise u, and vertical components v of flow velocity. Probes were placed at different locations on the top lid (Fig. 3.7) to cover the length of the channel and measure the velocity profiles for various positions. The time-averaged velocity profiles were then derived using measurements of instantaneous particle velocity. Fig. 3.8 shows the time-averaged velocity profiles at the centreline of the channel in Section 3, (Section 3-y200) where particle motion recording was carried out. As expected, the streamwise mean velocity profiles are similar to the theoretical one for plane channel flow. Obviously, knowing that the bottom of the duct is rough and the lid is smooth, the profile is not symmetrical and the mean velocity is higher close to the smooth boundary than to the roughened one.

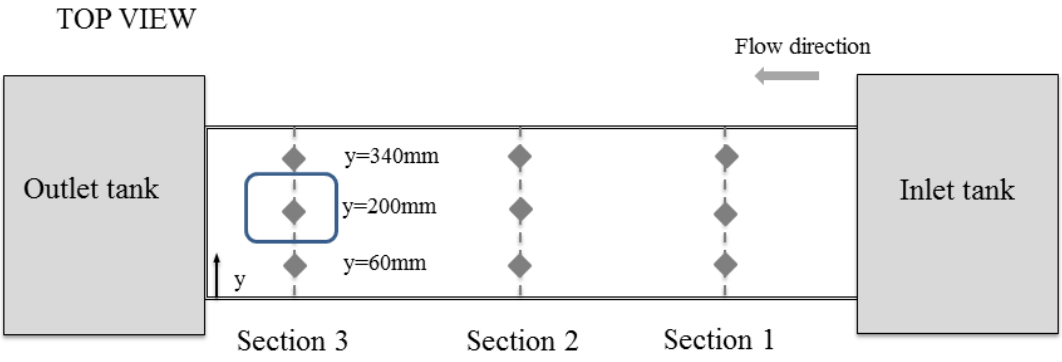

Figure 3.7 Locations of velocity measurements (field diamonds). Square box shows the location of particle motion recording.

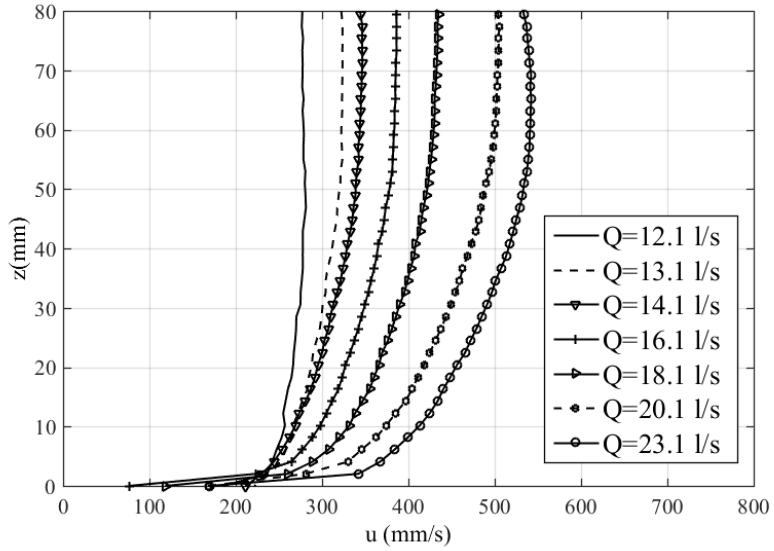

Figure 3.8 Time-averaged streamwise velocity profiles (Section 3, Y200).

3.2.3 Calculation of local shear velocity u^* and bed shear stress τ

Shear stress τ acting on the surface of the bed material is the driving force in the transport process. It has always been a challenging task to determine bed shear velocity u^* and subsequently calculate shear stress τ in experimental flumes or field channels. *Clauser* [1954] proposed a practical method in which shear stress can be determined from the time-averaged streamwise velocity profile following a logarithmic equation:

$$u(z) = \frac{u^*}{\kappa} \ln z + (-\frac{u^*}{\kappa}) \ln z_0 = C_1 \ln z + C_2 \tag{3.2}$$

Where $u(z)$ is the time-averaged streamwise velocity at elevation z, $\kappa = 0.4$ is the von Kármán constant and z_0 is the hydrodynamic roughness length. The time-averaged velocity data in the logarithmic layer can be fitted to (3.2) to calculate the coefficients C_1 and C_2, and then, bed shear velocity u^* can be determined from the value of C_1. Once u^* is obtained, the bed shear stress can be calculated as:

$$\tau = \rho u^{*2} \tag{3.3}$$

An example of data fitting in the logarithmic layer to estimate u^* is given in Fig. 3.9. In this example, fitting the data by least-squares method, C_1 was estimated as 38.052 and subsequently u^* was calculated as: $u^* = C_1\kappa = 38.052 \times 0.41 = 15.60$ mm/s (3.4)

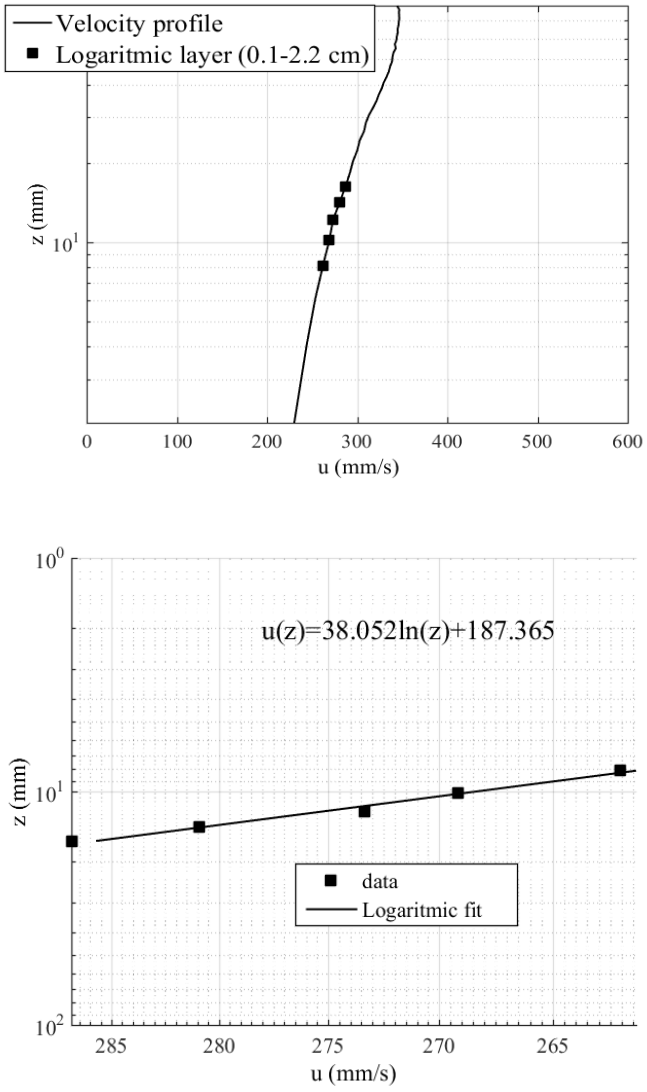

Figure 3.9 Example of u^* estimation by Clauser method, Q=14 l/s, S3Y200.

The 95% confidence interval (*CI*) for the shear velocity estimation was computed using the following formula [*Campagnol et al.*, 2013]:

$$CI = 2.179\sigma\ (u^*) / N^{0.5} \tag{3.5}$$

Where $\sigma(u^*)$ is:

$$\sigma(u^*) = \sqrt{\frac{N\sum_{i=1}^{N}(u_i - C_1 \ln(z_i) - C_2)^2}{(N-2)(N\sum_{i=1}^{N}(\ln(z_i))^2 - (\sum_{i=1}^{N}\ln(z_i))^2)}} \tag{3.6}$$

In which N is the total number of data in the logarithmic layer for which the Clauser method was used, u_i is the corresponding velocity for every single z_i obtained from the velocity profile, and $C_1 \ln(z_i) - C_2$ is the computed velocity using the least-squares fitting method. The shear velocities and the associated confidence intervals for the experimental discharges were computed regarding section (S3Y200) and results are presented in Fig. 3.10.

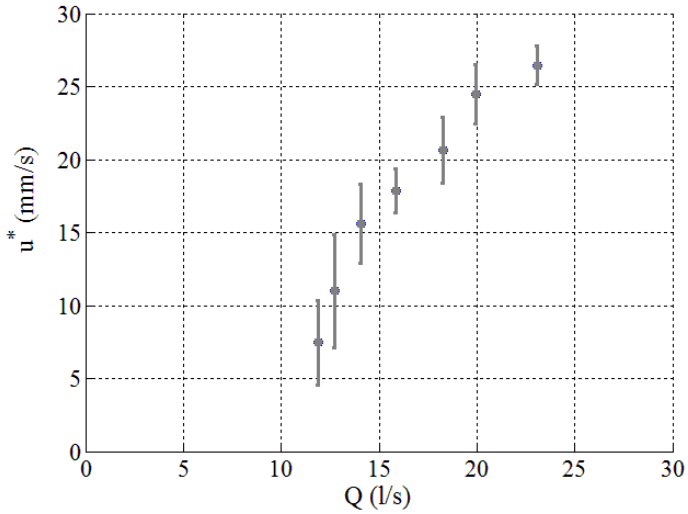

Figure 3.10 Computed shar velocities at the center of recording section (S3Y200) for different experimental discharges. Bar plots indicate the 95% confidence intervals.

As indicated in Fig. 3.10 shear velocity and flow discharge are positively correlated meaning that as the discharge increases the bed shear velocity and consequently bed shear stress also

increases. However, the shear velocity for the discharges of Q=12.1 and 13.1 l/s, might be underestimated. In fact, DOP calculates the velocity of tiny particles in the fluid based on the reflected echoes and as the intensity of dusts is not as much of those for higher discharges the computed values of velocity might be underestimated. Time averaged vertical velocity profiles for the range of performed discharges are depicted in Fig. 3.11. Relatively low values of vertical velocities encourage that the flow is generally unidirectional. The hydrodynamic characteristics of the experiments are summarized in Table 3.1.

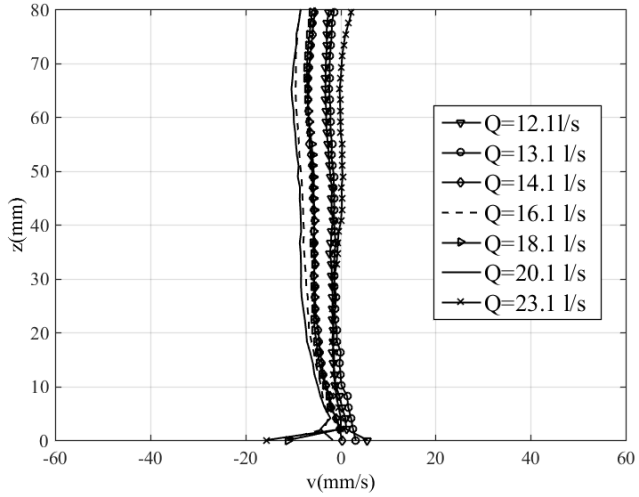

Figure 3.11 Time-averaged vertical velocity (v) profiles at the centre of channel (S3Y200)

Table 3.1 Hydrodynamic characteristics of experiments.

$Q(l/s)$	$U(mm/s)$	$u^*_{(S3Y200)}(mm/s)$	Re(–)	Flow type	Re^*(–)	Turbulent regime
12.1	272.7	7.45±2.92	2.83E4	Turbulent	22.35	Transitional
13.1	295.5	10.98±3.85	3.07E4	Turbulent	32.94	Transitional
14.1	318.2	15.60±2.72	3.30E4	Turbulent	46.80	Transitional
16.1	363.6	17.86±1.49	3.78E4	Turbulent	53.58	Transitional
18.1	409.1	20.66±2.26	4.25E4	Turbulent	61.98	Transitional
20.1	454.5	24.48±2.06	4.73E4	Turbulent	73.44	Rough (fully developed)
23.1	522.7	23.46±1.34	5.44E4	Turbulent	77.07	Rough (fully developed)

3.3 Incipient motion, transport capacity and particle feeding

Preliminary experiments of *Campagnol et al*. [2012] estimated the transport capacity of the flume (maximum solid discharge transported by the flow) as:

$$q^* = 0.008\left[(\frac{Q}{Q_c})^2 - 1\right]^{1.3} \tag{3.7}$$

in which q^* is the dimensionless sediment transport per unit width and time, Q is the flow discharge and Q_c =10 l/s is the threshold discharge for the initiation of motion. An *ad hoc* relationship between the calculated shear velocity and the critical shear velocity was found as

$$u^* / u_c^* = Q / Q_c \tag{3.8}$$

It is generally approved that the incipient sediment motion is not a well-defined condition [see, for example, *Buffington and Montgomery*, 1997]. In this study, the method proposed by *Radice and Ballio* [2008] was followed to experimentally estimate the threshold discharge. Volumetric sediment transport is calculated as:

$$Q_s^* = q * \sqrt{g\Delta d^3}B \tag{3.9}$$

Where Q_s^* is volumetric sediment transport (mm^3/s) $\Delta = \frac{(\rho_s - \rho)}{\rho}$ is the specific gravity and B is the flume width (400 *mm*).

Particle feeding was performed using an automatic impulsive feeder that repeatedly released a constant volume of sediment into the flume at a certain time interval (see again Fig. 3.1). The volumetric particle feeding rate is therefore:

$$Q_f = V_{slot}(1-p)/\Delta t \tag{3.10}$$

Where $V_{slot} = 380\times10\times10 = 38\times10^3\,\text{mm}^3$ is the volume of the slot, p =0.33 is the calculated sediment porosity and Δt is the time interval between each feeding action.

3.4 Experimental procedure

Experiments were conducted for a range of $u^* / u_c^* = 1.2 - 2$. Prior to start, the channel bed was cleaned from any dust and loose particles, the feeder was filled with white sediments and the pump was turned on. The discharge gradually increased to fill the inlet tank, and once the water arrived into the flume from the inlet tank, the discharge was raised and adjusted to the desired value for the sediment transport experiment. At this stage before particle feeding, the flow was running for 5-10 minutes to stabilize. After flow stabilization for each experiment particle feeding started and as soon as the first group of sediments approached the recording section, filming began at 32 fps. The duration of recording was 50 s for each experiment. Presented results are related with a focus area of 270× 200 mm^2 in streamwise and transverse direction, respectively. Following (3.9) and changing the time interval Δt experiments with different feeding rates could be carried out. Detailed characteristics of experiments are given in Fig. 3.12 and Table 3.2.

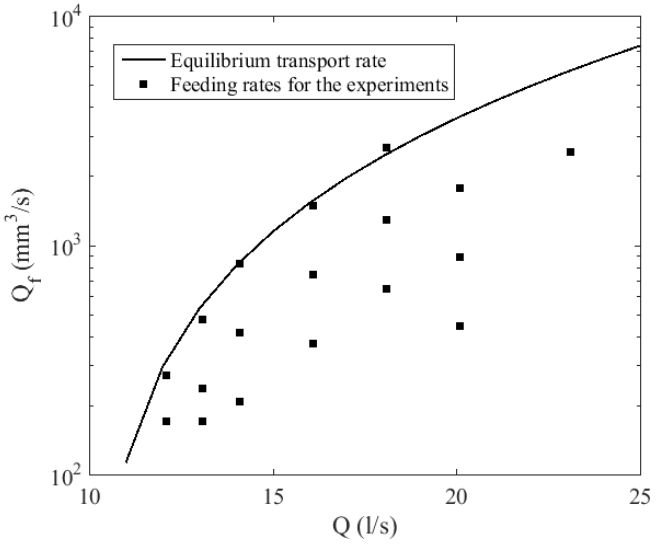

Figure 3.12. Experimental runs with respect to different discharges and feeding rates.

Table 3.2 Characteristics of feedings experiments.

Experiments	$Q(l/s)$	u^*/u_c^*	$\Delta t(s)$	$Q_s^*(\times 10^3 mm^3/s)$ (2.2)	$Q_f{}^*(\times 10^3 mm^3/s)$ (2.3)	$Q^*{}_f / Q^*{}_s$
R1	18.1	1.8	19.8	2.49	1.28	0.52
R2	18.1	1.8	39.6	2.49	0.64	0.26
R3	18.1	1.8	9.6	2.49	2.65	1.06
R4	20.1	2.0	14.4	3.63	1.76	0.49
R5	20.1	2.0	28.8	3.63	0.88	0.24
R6	20.1	2.0	57.6	3.63	0.44	0.12
R7	16.1	1.6	17.2	1.56	1.48	0.94
R8	16.1	1.6	34.4	1.56	0.74	0.47
R9	16.1	1.6	68.8	1.56	0.37	0.24
R10	14.1	1.4	30.6	0.84	0.83	0.99
R11	14.1	1.4	61.2	0.84	0.41	0.49
R12	14.1	1.4	122.4	0.84	0.20	0.25
R13	23.1	2.3	10.0	5.76	2.54	0.44
R14	13.1	1.3	54.0	0.55	0.47	0.85
R15	13.1	1.3	108.0	0.55	0.23	0.43
R16	13.1	1.3	150.0	0.55	0.16	0.31
R17	12.1	1.2	94.4	0.31	0.26	0.85
R18	12.1	1.2	150.0	0.31	0.16	0.54

Chapter 4 Image processing and particle tracking velocimetry (PTV)

4.1 Introduction to the application of image processing in fluid dynamics

In sediment transport studies, particle motion recording provides detailed information about the motion as well as quantitative information about the time evolution of particle position and velocity. Investigation of sediment transport throughout the observation of individual particles has been the core of many studies for decades [see e.g., *Francis*, 1973; *Fernandez Luque and Van Beek*, 1976; *Drake et al*., 1988; *Bottacin-Busolin et al.* [2008]; *Radice et al*., 2009 and 2010; *Lajeunesse et al*., 2010; *Ramesh et al*., 2011; *Roseberry et al*., 2012; *Campagnol et al*., 2013; *Julien and Bounvilay*, 2013; *Heays et al*. 2014, *Fathel et al*., 2015; *Furbish et al*., 2016]. Particle image velocimetry (PIV) and particle tracking velocimetry (PTV) are the main techniques that have been introduced and developed over the last three decades to measure the two, and three-dimensional velocity fields of moving particles in the flow [see *Smits and Lim*, 2000; *Willet and Kompenhans*; 1998 and *Blackett*, 1994]. The main principle of these techniques is grabbing video images of a lighten particle seeded flow to provide quantitative information about the flow field [*Nokes*, 2012]. In the present study, after conducting experiments of particle motion recording, (see Chapter 3) Streams package was used for particle identification and particle tracking velocimetry. An overview of Streams system with an example of its application on an experiment R10 (see Table. 3.2) are given in the following.

4.2 Overview of Streams system

Streams, is a flow visualization and analysis tool developed in the Department of Civil and Natural Resources Engineering at the University of Canterbury. The software is written in Java© programming language and is built in graphical user interface. In Streams, particle identification and tracking is achieved through a sophisticated analysis environment [*Nokes*, 2012]. Depending on the purpose of application, various algorithms can be used to process the raw data. Streams allows the user to import a sequence of images, detect particles and track them frame by frame providing Lagrangian information. In what follows, Streams core entities for a PTV analysis will be described.

4.2.1 Image sequence

Creating an image sequence is the initial step for any image-based analysis. Streams creates an image sequence from a series of frames captured by the recording device. Particle identification and tracking will be subsequently performed over the image sequence.

4.2.2 Particle identification

The term ‘particle’ stands for a region inside an image with different characteristics from the rest of the image. Particles in Streams are identified as neighbouring pixels with light intensities due to reflection higher than the background. Fig. 4.1 shows an example of an image in a sequence. Particle identification associated with the image is given in Fig. 4.2. Several algorithms are available for particle detection in Streams. For these experiments, a particle was detected for the pixels with intensities larger than a threshold defined by the user. An example of particle identification is illustrated in Fig. 4.2 in which over 100 particles were detected for the image (frame) in Fig. 4.1.

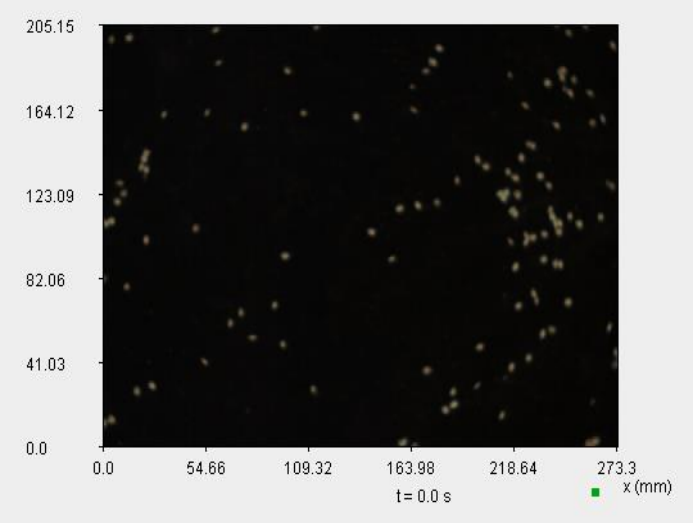

Figure 4.1 Sample of image within a sequence in Streams (Exp. R10).

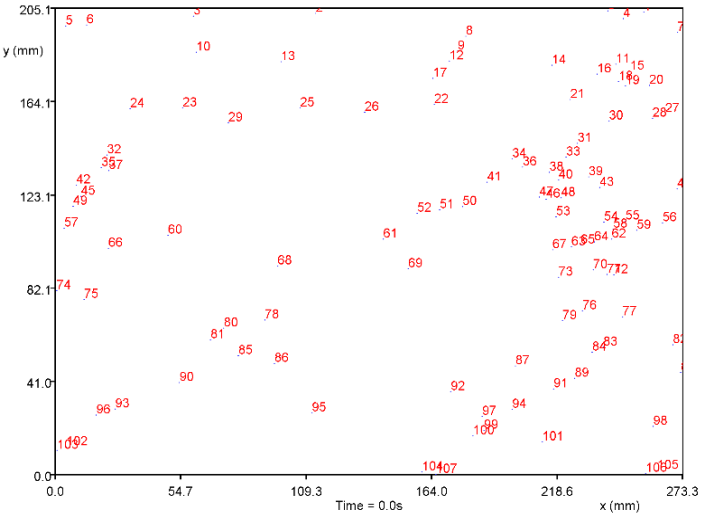

Figure 4.2 Sample of particle identification for the image sequence in Fig. 3.1.

4.2.3 Principles of Particle Tracking Velocimetry (PTV) in Streams

Having identified the existing particles in each frame, the next step is to connect the individual particles in subsequent frames and derive the full history of visualized particles. Tracking will result in Lagrangian information. In Streams Lagrangian paths are time series of particle position and velocity. It should be noted that the most challenging part of the PTV process is the tracking of individual particles from frame to frame. There are several techniques that can

be used, but each essentially ends to a decision-making algorithm that must select the "best match" between particles in two subsequent frames. A simple example of a match algorithm for particle in frame 1 is to pick among particles in frame 2 the one closest to the particle in frame 1.

4.2.4 Particle matching process

The first step in the matching process is to define a search window. In Streams, the search window is a rectangular region surrounding a particle in the first frame of the two being considered. Only particles located within this search window in the second frame are considered as possible matches to the particle in the first frame. Selecting a suitable search window will enhance the accuracy of matching process by limiting the candidates to a fraction of the total number of particles in the second frame. Once the match candidates have been identified for each particle in the first frame, Streams then calculates the costs of these matches using the costing strategies selected by the user. The user can assign a maximum matching cost (MMC) for each PTV analysis. Once the costing of individual candidates is calculated, Streams will then select the candidate with the lowest cost as a match to the particle in the previous frame. Therefore, setting of MMC is crucial for a successful analysis. If the given MMC is too low, correct matches will be missed. On the contrary, if the MMC is high several false candidates will be considered resulting in long computational times and possible mistakes in the matching process. Costing analysis also verifies that if a correct match in the next frame has not been associated with a particle, incorrect matches are not given a low cost. In fact, the best configuration of parameters is the one that all incorrect matches have costs exceeding the MMC. A total number of 16 different costings are available in Streams. Choosing the best MMC is a matter of conditions of experiments and practice. Depending on experimental conditions, for each test several matching costs were examined and the best was selected (see Table 4.1). Details of each costings can be found in *Nokes* [2012].

4.2.4.1 Particle mismatch and joining Lagrangian path

In general, due to the presence of many particles in PTV analysis, the matching process is not convenient and some of the results might be imperfect. In this respect, particles can be incorrectly matched, or not be even matched. Therefore, it is important to investigate the impact of such imperfections on the predicted results. The main reasons of particle mismatch are the presence of two and more adjacent particles in the search window as well as particle overlap. The mismatch results in the cut of particle paths where typically one path will finish at a certain time and location, and the second path will start closely within a few frames where the path was disconnected (see Fig. 4.3).

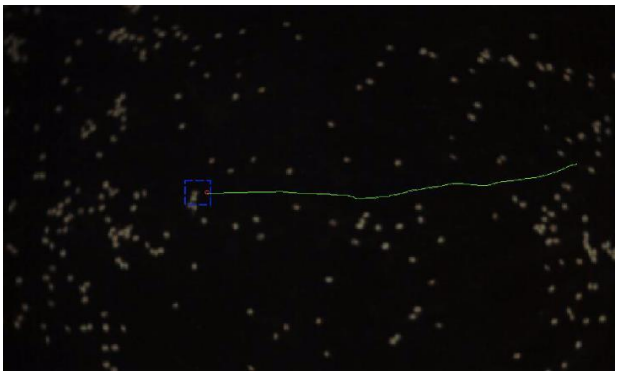

Figure 4.3. Example of partially tracked particle, mismatch due to the presence of several particles in the search window (blue rectangular represents the search window).

In this study, a full manual repairing was performed (R10a in Table 4.1) for the results of PTV analysis for experiment R10. The repairing provided a database of 321 correctly tracked particles. This database was used for the proof of concept to the framework introduced in *Ballio et al.* [2017]. Manual repairing was carried out as follows:

After particle identification, (i) tracked paths of particles were obtained by a distance matching process. As already discussed, these paths were discrete (discontinues), and did not represent the full history of each particle, thus (ii) a visual tool was developed to track the path of individual particles to find where the mismatch or discontinuation occurred. (iii) among other paths, the one whose beginning was closest to the end path in (ii) was joined to the earlier one. Finally (iv) connected paths were visually verified to assure a correct repairing. Example of a fully tracked particle (repaired paths) is given in Fig. 4.4.

Performing a manual repairing was time-consuming, hence, for other experiments it was decided to rely on the joining Lagrangian path algorithm defined by Streams.

The possibility of joining Lagrangian paths enables the user to connect the discrete paths that are corresponding to the same particle. However, it is important to mention that results of joining the Lagrangian paths were not always precise, and there were inaccuracies also in joining the segmented paths. Therefore, an accept/reject algorithm was introduced to achieve the best results from a PTV analysis using Streams.

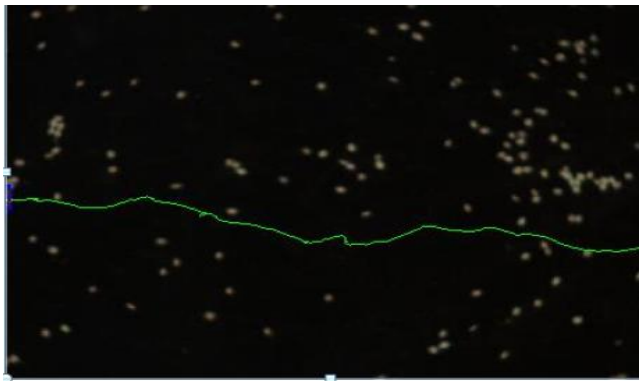

Figure 4.4 Example of a fully tracked particle.

4.3 Validation algorithm, accept/reject method

To perform the accept/reject method for the visual observation of particle path;

(i) Image sequence, particle identification and tracking were performed in Streams (see different costing of matches for each experiment in Table 4.1)

(ii) Joining Lagrangian path connected discrete segments to obtain the full Lagrangian path for each particle

(iii) Finally, an in-house developed visual tool was used to accept/eject the particles paths from (ii)

Summary of the total number of accepted particle paths for each experiment is given in Table 4.1. The validation rate was defined as the ratio between the total number of visually validated (accepted) paths and total number of detected paths.

Table 4.1. Summary of validation process.

Validated experiment	*Q* (l/s)	Applied Costings	No. of validated parths	Validation rate (%)
R1	18.1	Distance + recent velocity	971	58
R2	18.1	Distance + recent velocity	609	56
R3	18.1	Distance + recent velocity	1421	61
R7	16.1	Distance + recent velocity	416	64
R8	16.1	Distance + recent acceleration	398	62
R10a (manually repaired)	14.1	Distance + recent acceleration	321	100
R10	14.1	Distance + recent acceleration	192	66
R11	14.1	Distance + recent velocity	187	68
R12	14.1	Distance + recent velocity	187	69
R17	12.1	Distance + recent velocity	60	82

4.4 Statistical stability of validated database

Having obtained a database of validated particles for each experiment (Table. 4.1), the next step was to verify if the samples are statistically stable. For this purpose, hop length, hop averaged velocity, hop duration and hop rests were measured for each validated experiment and their datasets were randomly subsampled by half and 1/4 of the original population size (see chapter 1 for definitions and measurements). Following that a two-sample Kolmogorov-Smirnov (K-S) test was performed for these measurements to check the statistical stability of the samples.

In statistical analysis, the two-sample K-S test is used to find the equality between two cumulative distributions [*Frank and Massey*, 1951]. In other words, the test determines if samples come from populations with the same distribution. The two-sample Kolmogorov–Smirnov test is defined as:

$$D_{n,n'} = \max\left|F_n(x) - F_{n'}(x)\right| \tag{4.1}$$

Where $D_{n,n'}$ is the maximum absolute difference with F_n and $F_{n'}$ as the empirical distribution function for the range of x for each dataset. n and n' are the sizes of two samples respectively. The test is based on a null hypothesis h_0 assuming that there is no difference between the two distributions. The null hypothesis is rejected and at significance level α (the probability of rejecting the null hypothesis when it is true, $\alpha = 0.05, 0.1, \ldots$) if,

$$D_{n,n'} > c(\alpha)\sqrt{\frac{n+n'}{nn'}} \tag{4.2}$$

Where $c(\alpha) = \sqrt{-\frac{1}{2}\ln(\frac{\alpha}{2})}$ (4.3)

The results of the K-S test for the measured kinematics showed that the null hypothesis was not rejected at $\alpha = 0.05$ for any of the kinematics and proved that samples are stable. This

stability is also shown in Figs. 4.5 and 4.6 where the cumulative distribution functions (CDFs) of hop-averaged quantities indicated that sub-sampling the datasets of measured kinematics did not significantly alter the distributions.

Results of the K-S test for the nine validated experiments are given in Table 4.2.

Table 4.2 Kolmogorov-Smirnov test results for hop related quantities.

Kinematics	Δx		$u^{\Delta x}$		Δt^m		Δt^r	
Validated Exp.	$D_{n,n'}$	$c(\alpha)\sqrt{\frac{n+n'}{nn'}}$	$D_{n,n'}$	$c(\alpha)\sqrt{\frac{n+n'}{nn'}}$	$D_{n,n'}$	$c(\alpha)\sqrt{\frac{n+n'}{nn'}}$	$D_{n,n'}$	$c(\alpha)\sqrt{\frac{n+n'}{nn'}}$
R1	0.09	0.25	0.10	0.25	0.09	0.25	0.06	0.25
R2	0.10	0.23	0.08	0.23	0.06	0.23	0.04	0.23
R3	0.11	0.21	0.07	0.21	0.06	0.21	0.05	0.21
R7	0.07	0.25	0.09	0.25	0.11	0.25	0.05	0.25
R8	0.05	0.25	0.10	0.25	0.05	0.25	0.06	0.25
R10	0.07	0.24	0.06	0.24	0.07	0.24	0.05	0.24
R11	0.10	0.36	0.10	0.36	0.19	0.36	0.05	0.36
R12	0.19	0.33	0.11	0.33	0.14	0.33	0.04	0.33
R17	0.15	0.35	0.11	0.35	0.07	0.35	0.07	0.35

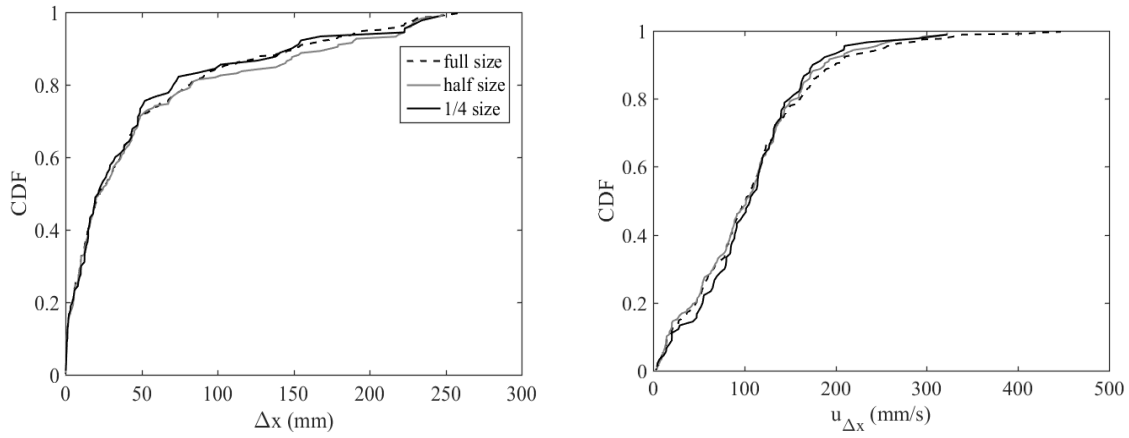

Figure 4.4 Cumulative Distribution Function of (CDF) hop length (left) and hop-averaged velocity (right) for the ¼, ½ and the full sample size. Distributions correspond to Experiment R1.

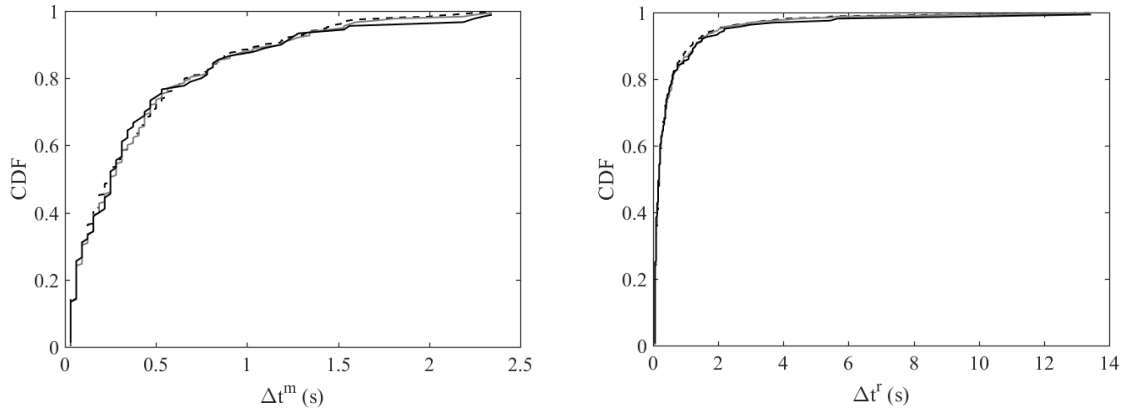

Figure 4.5 Cumulative Distribution Function of (CDF) hop duration (left) and time of rest (right) for the ¼, ½ and the full sample size (Experiment R1).

Chapter 5 Post-processing of particle tracking data

5.1 Introduction

Improvements in measuring capabilities lead to more detailed information and consequently, new conceptual issues arise requiring appropriate consideration. Two main aspects are discussed in this chapter. First, having detected the position of bed-load particles at every instant (PTV results), a need emerges to recognize motion and stillness of particles. This is necessary as kinematics measurements including those introduced in Chapter 2 require identifying particle changes of state (from stillness to motion and vice versa). It should be also added in this respect that a third state might be introduced for particles vibrating around a certain position. These vibrations may be considered as actual movements or, differently, they may be considered as stillness and, consequently, filtered out. The second aspect addressed here, an approach stimulated by several different choices appeared in the literature, is the possibility to introduce a minimum length for a particle hop to be considered a significant contribution to downstream conveyance of sediment.

5.2 Definition of motion and labelling

The descriptive/conceptual framework presented in Chapter 2 identifies the full history of a (tracked) particle as a combination of successive instants of motions and rests representing the basis of bedload transport. Therefore, applying this conceptual method on experimental data for kinematics measurements requires ‘motion’ identification. In other words, a need emerges to detect at every instant (frame) if a certain particle is at motion or not (labels 1 and 0

respectively). Different methods were proposed for motion recognition. For instance, *Roseberry et al*. [2012] introduced a cut-off velocity and defined motions based on values higher than that. Differently, *Seizilles et al*. [2014] considered a particle in motion if the standard deviation of the position over 4 successive frames is higher than 0.1 d. In this study motion labelling was initially performed using a criterion proposed by *Campagnol et al*. [2013], according to which a particle can be considered in motion at a certain instant if its *x* (streamwise) position is smaller than the *x* positions taken in all the subsequent instants:

$$if \;\; x_{ti} < x_{ti+\Delta t} \text{ for all } \Delta ts \rightarrow \text{Motion} \rightarrow \text{labeled (1)} \qquad (5.1)$$

(5.1) was then modified and another possible definition of motion was introduced. The new definition of motion required the position of a particle to be lower than all the future positions as well as being higher than all the past positions:

$$if \; x_{ti-\Delta t} < x_{ti} < x_{ti+\Delta t} \text{ for all } \Delta ts \rightarrow \text{Motion} \rightarrow \text{labeled (1)} \qquad (5.2)$$

The new criterion, more restrictive than the previous one, obviously increased the possibility to label a particle as still. Comparison between the definitions is illustrated in Fig. 5.1. As indicated, total number of resting instants are in general higher for the new definition.

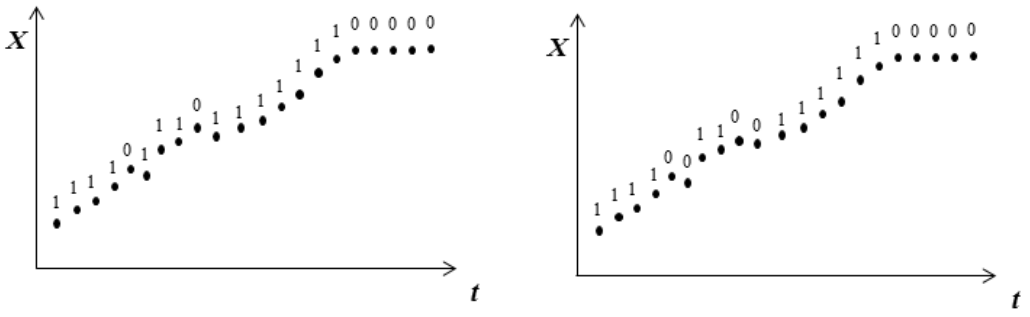

Figure 5.1 Campagnol et al. 2013 definition of motion (left) modified definition of motion (right).

The streamwise position (*x*) of one sample tracked particle from experiment R10a (see Table 4.1) is given in Fig. 5.2. The corresponding time series of the stream-wise particle velocity (*u*) was characterized by temporal fluctuations. Both definitions of motion were applied to the time

evolution of streamwise and the clipping function M introduced in chapter 2 separated the instants of motion and rest (Fig. 5.2). A preliminary choice was made in both definitions to consider movements of a particle around a stable position as stillness. According to such a choice, the velocity series in Fig. 5.2 illustrated both neat motion and fluctuations that could be considered as vibrations to be filtered out.

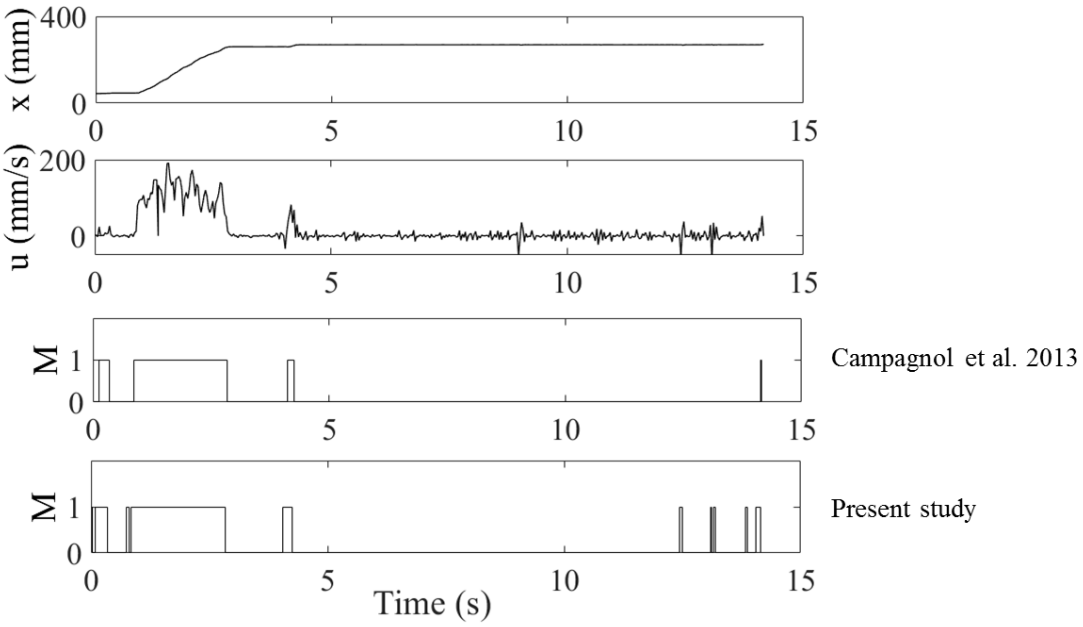

Figure 5.2 Sample of a tracked particle history: temporal evolution of particle position (x), velocity (u), and M as the status of the particle at each instant identified with the criterion of *Campagnol et al*. [2013] and the modified one (upper and lower diagram, respectively).

5.3 Comparison of definitions

In the following, the two definitions of motion were applied on particle tracking data from experiment R10a to measure some kinematics and compare the statistical results.

5.3.1 Statistics of instantaneous velocities

Figure 5.3 shows the Probability Density Function (PDF) of *u* for the statuses of stillness and motion identified with both the former definition of *Campagnol et al*. [2013] and the new criterion. The peak of the PDF for stillness (Fig. 5.3a) shows that most of the instantaneous velocities at rest fluctuate around zero. However, the right tail indicates that low probabilities of higher velocities also exist and they are related to particle shaking and short displacements, which were considered as stillness by the identification criteria. As one would expect, the instantaneous velocity values for motion are significantly higher (Fig. 5.3b), proving that both definitions depict a clear separation of the two populations. However, a comparison between the individual peaks of the PDFs in Fig. 5.3b and the right tails of the PDFs in Fig. 5.3a indicates that a large number of short displacements that were labelled as motion by the former criterion were instead identified as instants of rest by the new one.

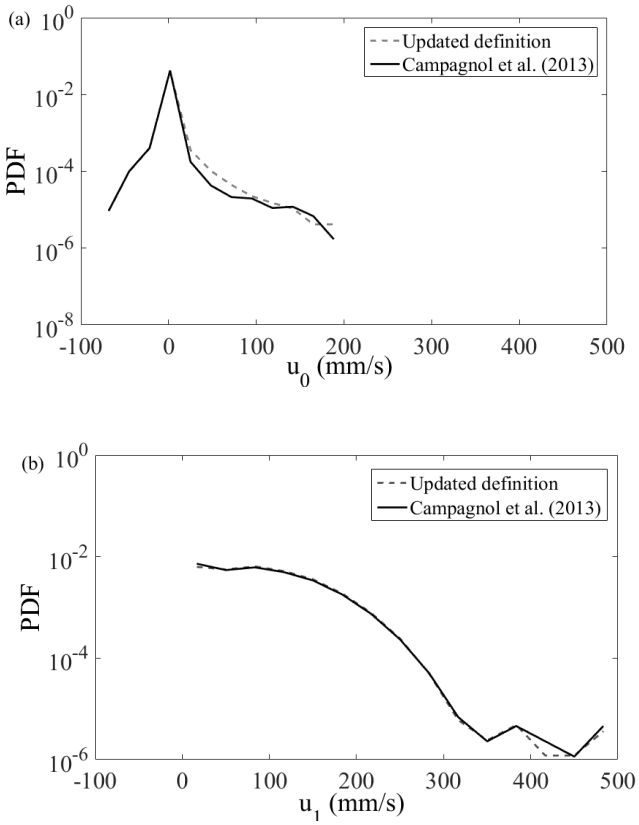

Figure 5.3 Probability Density Function (PDF) of instantaneous velocity for particles at rest (a) and motion (b) considering both the criterion of *Campagnol et al.* [2013] and the new one.

5.3.2 Statistics of hop length, hop duration and hop-averaged velocity

The total number of hops detected by each definition of motion is summarized in Table 5.1 together with the statistical properties (mean and standard deviation) of the hop-averaged kinematic quantities. The total number of hop lengths detected using the new criterion (240) was significantly lower than that (620) of hops detected by the criterion of *Campagnol et al*. [2013]. In addition, the first- and second-order statistical properties demonstrate how the different criteria for the definition of motion impacted the resulting values. The mean value of hop length increased using the new criterion, the same happening also for particle velocity and time of motion. The standard deviation of the samples also increased, but less than the mean value, thus resulting in a lower coefficient of variation.

Table 5.1 Statistical moments (mean and standard deviation) of hop-averaged kinematic quantities for the criterion of *Campagnol et al*. [2013] and the new one.

	Criterion by *Campagnol et al.* [2013]	New criterion
Number of hops	620	240
mean(Δx)(mm)	16.2	41.5
std(Δx) (mm)	40.4	56.3
cv(Δx) (-)	2.5	1.36
mean($u_{\Delta x}$) (mm/s)	20.7	50.7
std($u_{\Delta x}$) (mm/s)	27.5	35.2
cv($u_{\Delta x}$) (-)	1.33	0.69
mean(Δt^m) (s)	0.3	0.8
std(Δt^m) (s)	1.1	1.6
cv(Δt^m) (s)	3.67	2

The PDF of Δx obtained using the two criteria is presented in Fig. 5.4. The occurrence of the

shortest hop lengths was higher for the criterion by *Campagnol et al*. [2013] than for the new one. The PDFs of Δt^m and $u_{\Delta x}$ are illustrated in Figures 5.5 and 5.6, respectively. The PDF of Δt^m indicates how the new definition filtered short-duration motions. The PDF of $u_{\Delta x}$ also presented a much bigger right tail and vanishing presence of very low values when the new criterion was used.

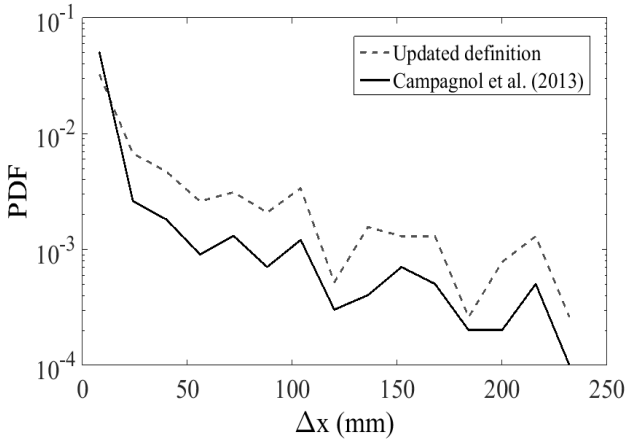

Figure 5.4 PDF of hop length for the criterion of *Campagnol et al*. [2013] and the new one.

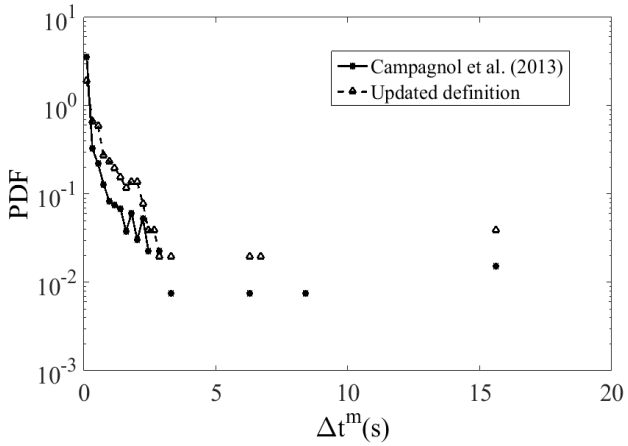

Figure 5.5 PDF of time of motion for the criterion of *Campagnol et al*. [2013] and the new one.

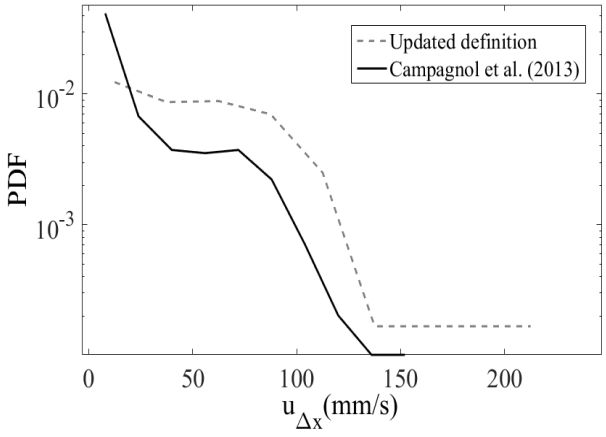

Figure 5.6 PDF of hop-averaged particle velocity for the criterion of *Campagnol et al*. [2013] and the new one.

The average of moving particles $\overline{N_m}$, Eulerian porosity φ_A^m, total number of entrainments N_e and disentrainments N_d and finally the average of entrainment and disentrainment rates $\overline{E}$, $\overline{D}$ are given in Table 5.2.

Table 5.2 Mean values of Eulerian quantities calculated by each definition of motion

	$\overline{N_m}$	φ_A^m	N_e	N_d	$\overline{E}(mm/s)$	$\overline{D}(mm/s)$
Campagnol et al. [2013]	16.64	0.34	839	875	0.0043	0.0045
Modified definition	15.56	0.32	379	419	0.0019	0.0021

As presented in Table 5.2, the total number of particles at motion identified by *Campagnol et al*. [2013] is higher than those recognized by the modified definition of motion and as a result Eulerian porosity φ_A^m also increases. The behaviour of porosity against those of other Eulerian measurements shows that the quantities are significantly correlated with porosity. As seen in Table 5.2, for example, with a 6 percent increase of porosity the entrainment and disentrainment rates were almost doubled.

5.4 Effect of using a threshold for hop length

Some previous studies introduced a threshold for hop lengths to be included in the analysis of the bed-load sediment transport. For example, *Drake et al*. [1988] considered only hop lengths longer than one particle size, while *Campagnol et al*. [2013] used a threshold of 1/30 the particle size.

Introducing a threshold might bias the data sample or, differently, a process might be self-similar in relation to a threshold in certain ranges. The concept is qualitatively illustrated in Fig. 5.7, where an imposed threshold initially affects a statistical moment of a quantity, after that a self-similarity range is present, then the moment varies again. In principle, a threshold located in a self-similarity range would not bias the data; the opposite would happen for a threshold out of that range.

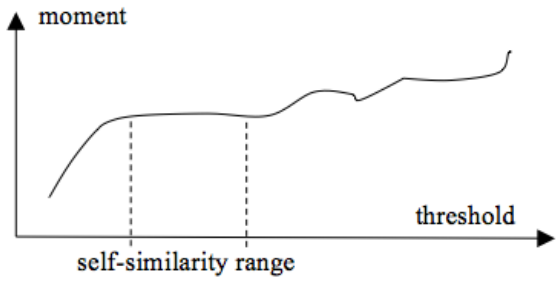

Figure 5.7 Qualitative indication of sensitivity of a quantity to some threshold.

Considering the new criterion for identification of motion, the sensitivity of the hop length Δx hop-averaged velocity $u_{\Delta x}$ and time of motion Δt^m was assessed to check the possibility to remove short hops. A series of thresholds (from 0.1 to 10 times the particle size) was introduced and the statistical behavior of the kinematic quantities was analyzed. Results are depicted in Fig. 4.8, demonstrating that the mean and median values of all the quantities constantly increase as the threshold becomes larger, while the standard deviation is gradually falling for the hop length and the mean velocity, while increasing for the time of motion. From the analysis, no self-similarity range could be recognized. The Cumulative Density Function (CDF) of hop length, hop-averaged velocity and time of motion was computed for different thresholds, and results are presented in Fig. 5.9. The CDF of the quantities progressively shifts right-wards as

the threshold for Δx is increased. This behaviour obviously reflects the fact that a larger threshold results in the absence of shorter hop lengths in the averaging sample. Therefore, a bias of the sample due to any chosen threshold was demonstrated, analogously with what was obtained for the moments of the distributions (Fig. 5.8).

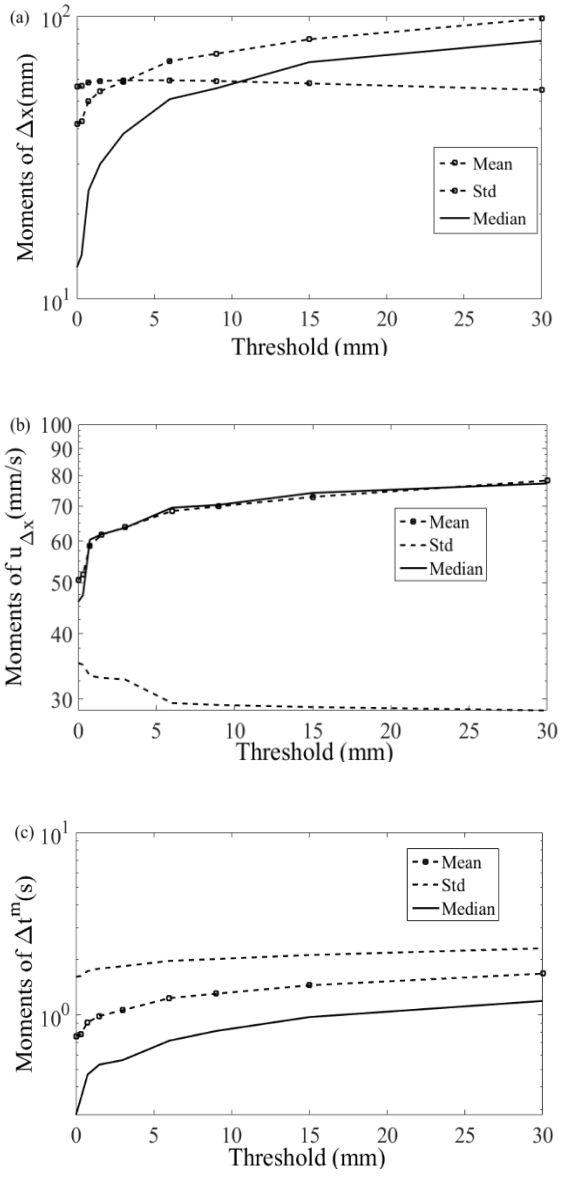

Figure 5.8 Statistical moments (mean, standard deviation, and median) of kinematic quantities using different thresholds for hop length: (a) hop length, (b) hop-averaged velocity, (c) time of motion.

Again, any choice is possible. The one preferred here is to use no threshold but, in addition, the important implication of the presented results is again that any statistical depiction of the sediment transport process must be accompanied by a clear description of the methods used for the analysis.

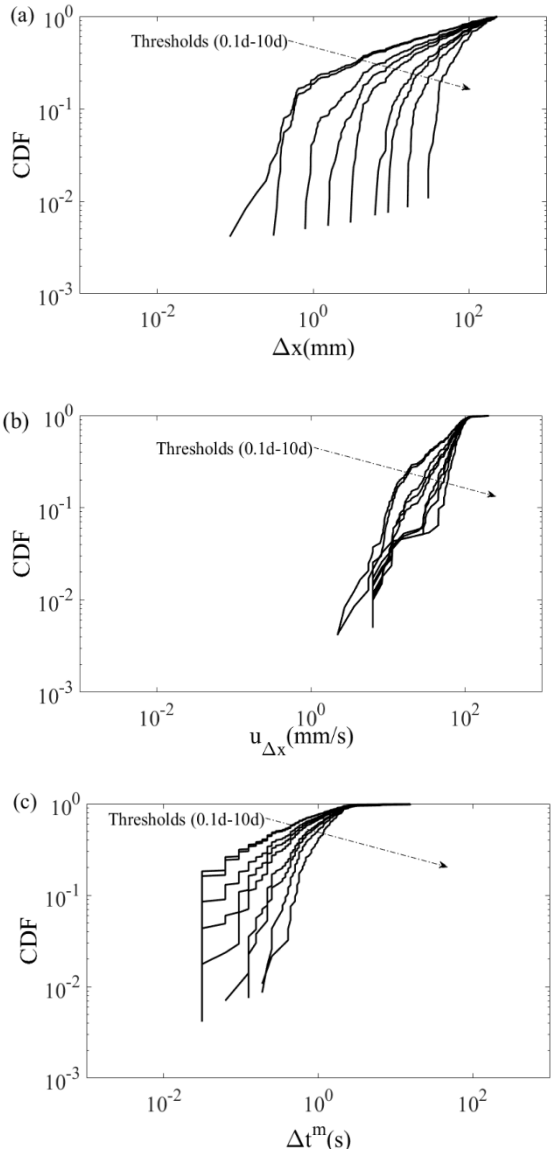

Figure 5.9 CDF of quantities using different thresholds for hop properties: (a) hop length, (b) hop-averaged velocity, (c) time of motion.

5.5 Conclusions

Conceptual/operational issues emerge when post-processing PTV data for bed-load sediment transport. Some of these issues were here highlighted and addressed on the basis of an experiment where image processing was applied to track the position of individual bed-load particles over time. Two issues considered are (i) definition of motion and stillness states for particles and (ii) possibility to introduce a minimum threshold for hop length. The sensitivity of resulting statistics of particle motion to different operational choices was explored. The main conclusions from the analysis of post-processing data are given in the following:

1. A framework for analysis of particle kinematics requires identification of particle state, thus a clear definition for instants of motion and rest is necessary.
2. The results of a statistical analysis indicated that data samples were highly affected by criteria chosen to recognize motion and stillness.
3. Applying a threshold for minimum hop length also biased the data samples as no self-similarity range could be detected.
4. In general, it is strongly highlighted here that thorough description of the strategies used for analysis is essential to make any data set suitable for comparison with other ones. In the absence of such a description, it is impossible to interpret possible differences among data from different studies.

5.6 General remark

The above results prove that statistics of particle motion are highly sensitive to different post-processing algorithms. The criterion to be privileged is an arbitrary choice of the researcher. Following a declared intention to filter out particle vibration, the modified criterion was here preferred. These considerations strongly call for thorough explanation of the post-processing algorithms used by any researcher, in the absence of which comparison among different data

sets would be majorly flawed.

Chapter 6 Lagrangian measurements

Experiments conducted under different stage values u^* / u_c^* (see chapter 3) resulted in datasets obtained from automatic tracking of individual particle motions (see chapter 4). These rich data collections provide the basis for defining the underlying forms of the distributions of Lagrangian quantities described in Chapters 1 and 2. In this chapter, individual properties of several up to many particles will be put together to build the samples. “Statistical analysis” will then represent the form and moments of the distribution of these samples.

Of particular interest, are the distribution of streamwise particle velocities, the distribution of particle hop distances and associated travel times, and the distribution of resting times. In the following sections, these distributions will be explored and the results will be compared with earlier works.

6.1 Particle instantaneous velocity

This section turns to the determination of the instantaneous velocity distribution for the moving and still particles, u_1 and u_0, respectively. Labels 0 and 1 refer to the clipping function defined in (2.1) and to the labelling procedure described in section 5.2. Instantaneous velocities are calculated based on displacements within subsequent frames as:

$$u = {dx}/{\Delta t}, dx = x_{i,t+\Delta t} - x_{i,t} \tag{6.1}$$

Several thousands of particle velocity values were obtained for each experiment. Samples of instantaneous velocity distributions for particles at rest and motion are given in Figs. 6.1 and 6.2, respectively. Negative values represent particles vibrations around a fixed position. These vibrations were recognized as stillness when analyzed with the proposed criterion for definition of motion. Presented results indicate a separation between the distributions of moving and still

particles. Regarding particles at rest u_0, the probability distribution function (PDF) is (almost) centered on zero.

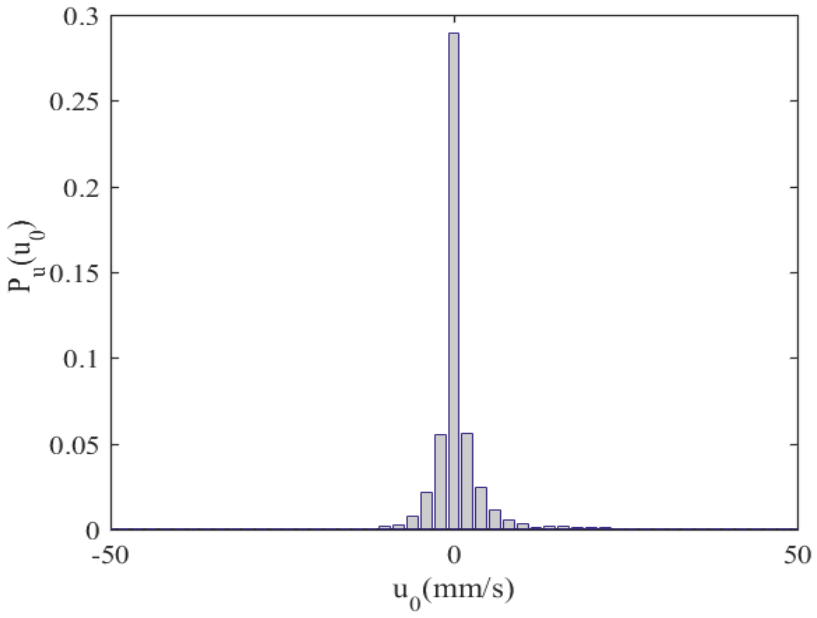

Figure 6.1 Probability distribution of instantaneous velocities for still particles u_0. Results from Experiment R7.

In contrast with *Lajeunesse et al*. [2010]; *Rosebery et al*. [2012]; and *Furbish et al*. [2016] who found an exponential form of distribution for the velocity of moving particles u_1, a truncated Gaussian form of distribution approximated the results in this study (Fig. 6.2). The finding is consistent with those reported by *Martin et al*. [2012], *Ancey and Heyman* [2014] and *Heays et al*. [2014] who also found that a Gaussian function closely matched the distribution of particles at motion. Dissimilar forms of distributions for the velocity of moving particles are due to different experimental set-up and measurement techniques. For example, the definition of motion in this study recognized short vibrations as rest and thus small displacements and subsequently the associated velocities were excluded from the statistical analysis. On the other hand, the slower frame rate used in this study (32 fps), compared to for instance, the 250-fps data of *Lajeunesse et al*. [2010] could not capture the subtle changes at slower particle velocities. It is however important to note that the tails in either form of distributions (the truncated Gaussian or exponential laws) show that the highest measured particle velocity does not exceed the mean fluid velocity (U=363.6 mm/s is the mean fluid velocity for Exp. R7, see Table 3.1).

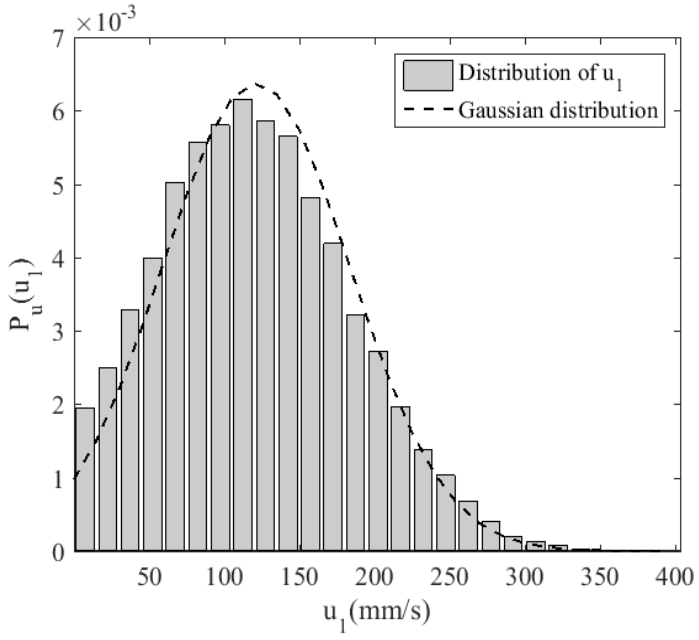

Figure 6.2 Probability distribution function for instantaneous velocities of moving particles u_1 (Experiment R7)

In Fig. 6.3 measurements of normalized particle velocity u/V_S for the full range of experiments are compared to those reported by five previous investigations. Here, $V_S = \sqrt{Rgd}$ is the particle settling velocity. *Lee and Hsu*, [1994], and *Abbott and Francis*, [1977] tracked the motion of individual particles over a rigid non-erodible rough bed while the results of *Fernandez-Luque and Van Beek*, [1976], *Nino and Garcia*, [1994] and *Lajeunesse et al*. [2010] correspond to erodible beds. As indicated in Fig. 5.3 except for the value corresponding to the lowest point of u^*/V_S found in this work, the average of particle velocities almost linearly increases with the stage value pointing the constant value of u/u^*. As described in chapter 3, the results of velocity measurements and shear velocity calculation using DOP2000 for the experiment with the lowest discharge (Q=12 l/s) were underestimated. This might best explain why the normalized value of (u^*/V_S) is slightly dispersed form the linear trend. A closer inspection also shows that particle average velocity in fixed bed experiments is higher than the experiments of erodible bed suggesting that particles entrained by the flow move faster over a fixed bed than

above a mobile one.

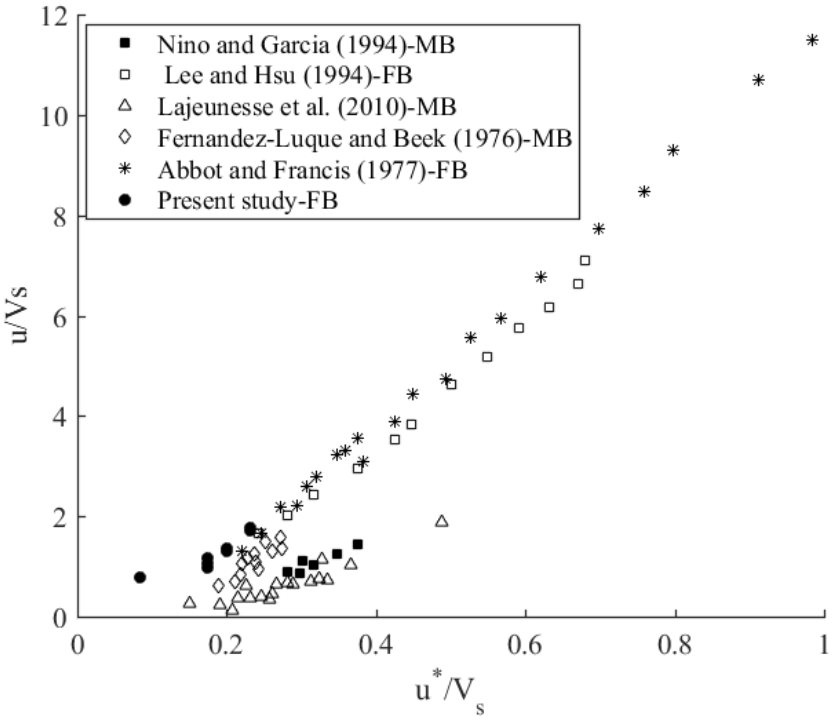

Figure 6.3. Average particle velocity u/V_s vs u^*/V_s measured by different researchers. FB represents a fixed bed and MB stands for a mobile bed configuration.

6.2 Experimental censorship in measurements of hop properties

As said earlier, particle motion recording offers high-resolution data for the statistical analysis of bed-load kinematics. Since the application of these techniques is growing it is therefore valuable to pay attention to what is truly being measured. Fig. 6.4 illustrates the sketch of experimental measurements. With special reference to intermediate range of scale and finite time and space domains, trajectories of tracked particles can be divided into *complete* and *incomplete* trajectories. Complete trajectories (also known as intermediate trajectory, and hop) are identified as trajectories for which motion from entrainment to disentrainment is entirely detected within the observation area. In contrast to complete trajectories, incomplete trajectories correspond to those that are only partially detected within the observation scale. Fig. 6.4 illustrates examples of complete and incomplete trajectories. It should be mentioned

that an incomplete trajectory is phenomenologically a segment of a complete one which, due to the finite observation scale, is non-completely observed and is therefore censored. In conclusion, one should bear in mind that during a visual experiment, due to the limited scale of observation complete hops are detected only for a portion of tracked trajectories and as a result, the associated measurements are biased by experimental censorship.

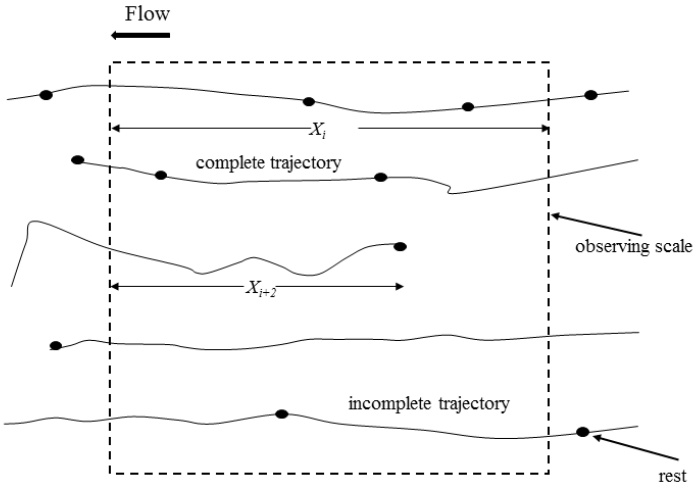

Figure 6.4 Schematic illustration of hop measurements and experimental censorship. X is the total distance that each particle travels during its observation.

First and second-order statistical moments (mean and standard deviation) together with coefficient of variation $cv = \sigma / \mu$ for hop related quantities (length, time of motion and velocity $u_{\Delta x} = \Delta x / \Delta t^m$) were analyzed for a range of spatial scales in Fig. 6.5. The scale dependence of moments was investigated using the constant width (L_y=200 mm) and increasing the observation length in the streamwise direction (L_{scale}). The scale length was then normalized by the entire length of observation (270 mm).

Fig. 6.5a and Fig. 6.5b demonstrate that when the observation scale is increased the average and standard deviation of hop lengths and hop durations also progressively grow, showing that enlarged observation areas enable the measurement of larger hop lengths and subsequently longer durations. The coefficient of variation remained constant after $L_{\text{scale}}/L_{\text{frame}}$=30. As depicted by Fig. 6.5c, in contrast to the behavior of hop length and hop duration, the mean and

standard deviation of hop averaged velocity are scale independent, suggesting that hop average velocity is invariant of scale.

The scale analysis examined the impact of spatial censorship. Associated results (Figs. 6.5a and 6.5b) prove that the observation scale continuously censors the complete hop lengths and their durations, telling that further progress is required in determining the cost of this censorship. *Roseberry et al*. [2012], *Fathel et al*. [2015] and *Furbish et al*. [2016] were probably the first studies who mentioned experimental censorship, however they did not propose a strategy to compensate it.

In the following, the statistical distribution of measured hop lengths and associated durations will be explored and the biased mean values of quantities will be calculated from their distribution. Ensuing the analysis of hop quantities, unbiased mean values will be then calculated using the method proposed by *Ballio et al*. [2017] and results will be compared with the biased measurements. Following that, the variations of unbiased and measured (biased) mean values of hop lengths and hop durations with shear velocity will be studied and results will be compared with previous literature investigations. To complete the investigation of hop properties, measurements of times of rest and the variation of their average values with shear velocity will be given. Please note that for a simplicity in terminology, herein, $\Delta(\Theta)$ represents a complete hop property, and $\Delta(\Theta)_{incomplete}$ stands for an incomplete property. Θ refers to any hop related quantity. Measured properties are also called ‘biased’.

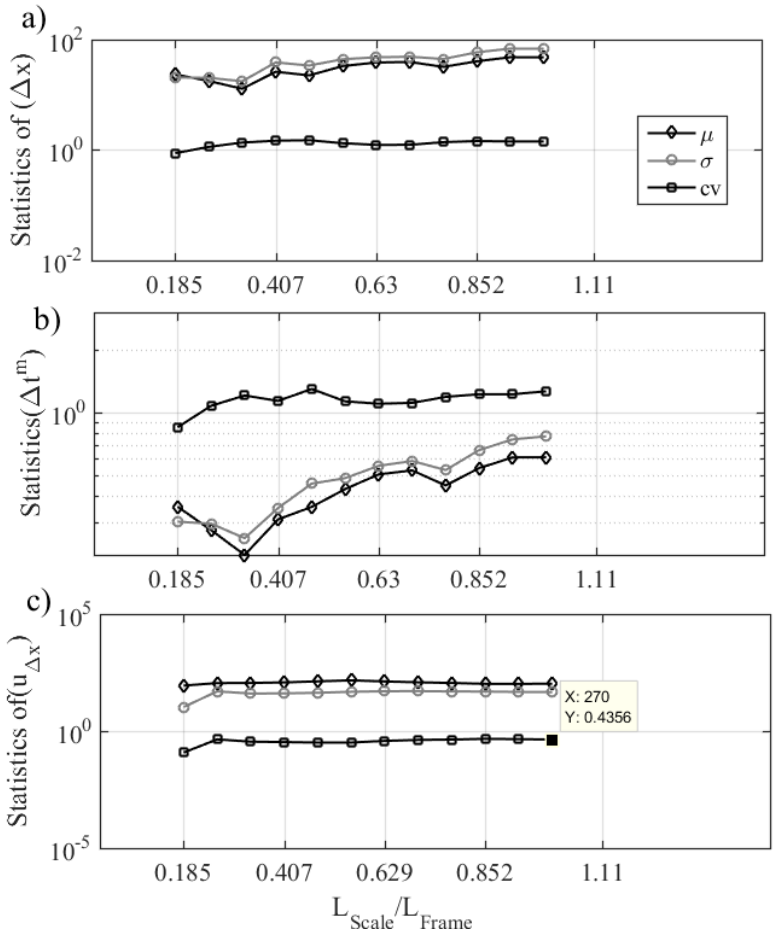

Figure 6.5 Scale analysis of hop measurements. a) hop length, b) hop duration and c) hop averaged velocity (Experiment R10).

6.3 Hop length

In this study, for the range of validated experiments over 700 complete and more than 5000 incomplete trajectories were identified within the observation window (270×200 mm^2). Figs. 56.6 and 6.7 depict examples of the distributions of complete and incomplete hops in this study. Distributions are related with measurements in Experiment R10. First and second order statistical moments (mean and standard deviation) of measured hop lengths are given in Table 6.1.

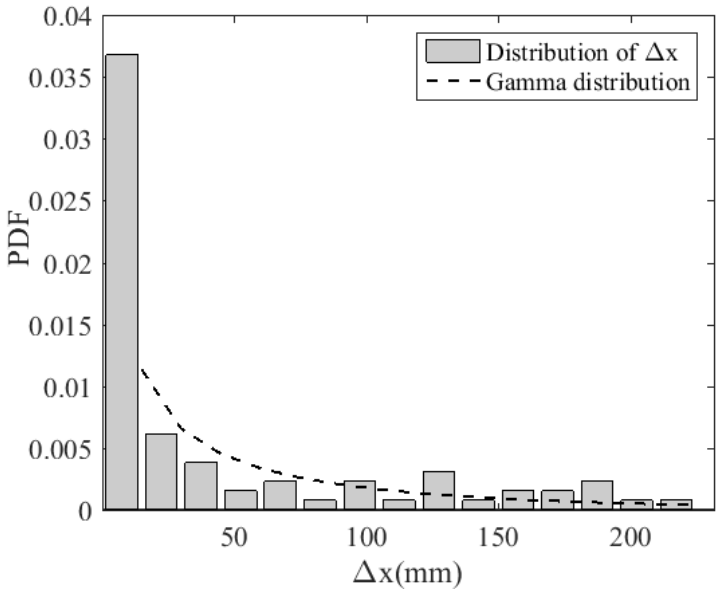

Figure 6.6 Probability distribution of complete hop lengths. Dashed line represents gamma distribution (Results from R10).

As indicated in Fig. 6.6, a gamma function approximates the distribution of measured hop lengths in this study. Presented results are in consistence with the findings of *Roseberry et al*. [2012] who found a similar form of distribution in their visual experiments of coarse sand particles. With respect to other reported datasets, *Lajeunesse et al*. [2010] suggested a distribution with a mode at finite hop distance, *Nakagawa and Tsujimoto* [1980] suggested an exponential distribution and *Fathel et al*. [2015] and *Furbish et al*. [2016] reported a Weibull distribution. As stated by *Martin et al*. [2012] "other experiments…have found only exponential or gamma (hop distance) distributions [*Hassan et al*., 1991; *Schmidt and Ergenzinger,* 1992; *Habersack*, 2001; *Lamarre and Roy*, 2008]".

The distribution of data in Fig. 6.7 shows that incomplete hop lengths (which are indeed censored hops) are dispersed and their sizes vary from a few particle diameters up to 270 mm (identical to the length of observation). A comparison between Fig. 6.6 and Fig. 6.7 and the difference between the mean value of complete and incomplete hops (Table 6.1) clearly indicates that the observation scale used for measurements was relatively short compared to physical length of the process. This further suggests that, the mean values of complete hop lengths (see Table. 6.1) should be considered biased and Fig. 6.6 may not represent the true

form of distribution associated with complete hop lengths.

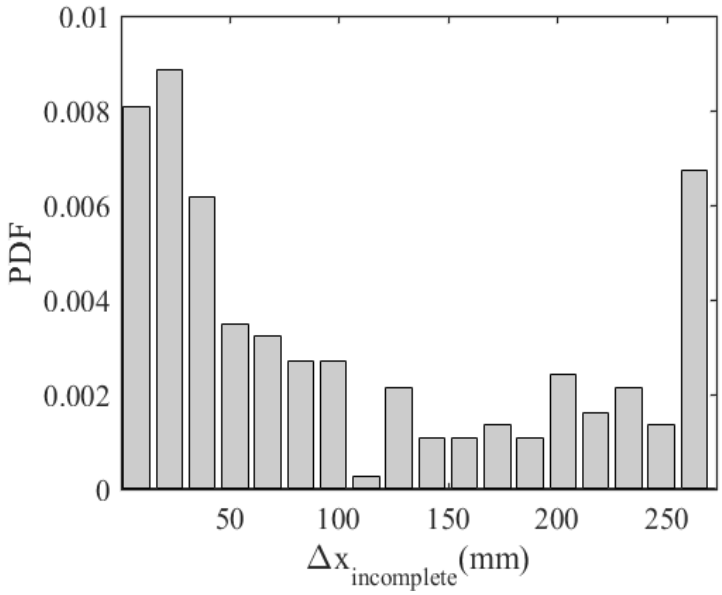

Figure 6.7 Probability distribution of incomplete hop lengths (Experiment R10).

In the present study, unbiased (true) values were inferred from the biased ones following the method proposed by *Ballio et al.* [2017]. In this method, the unbiased average of measurements is obtained using the full Lagrangian history (including complete and incomplete trajectories) of tracked particles and the number of detected entrainments. The proposed formula is:

$$\Delta x_{\text{unbiased}} = \sum X_i / N_e \tag{6.2}$$

where X_i is the total streamwise distance that particle *i* travelled within the observation scale (see Fig. 6.4) and N_e is the total number of detected entrainments with respect to the same spatial scale. The variation of normalized value of biased (measured) and unbiased hop lengths (true ones) $\mu(\Delta x)_{biased}/d$, $\mu(\Delta x)_{unbiased}/d$ with stage value u^*/u^*_c together with a summary of previous investigations are given in Fig. 6.8.

Experimental results are scattered by almost two orders of magnitude. Despite the variations in the normalized value of biased hop length, a general consistency in the findings of different studies suggest that on average, complete hop length is increasing with shear velocity. Some studies [e.g., *Lee and Hsu*, 1994; *Lajeunesse et al*., 2010] pointed out a steep increase whereas the measurements of this work show a much slower growth and is rather consistent with the data of *Ramesh et al.* [2012] and *Campagnol et al*. [2013].

The ratio between the unbiased mean value and the biased average of hop lengths is 2.9 and 17.7 for the lowest and the highest discharge respectively. This significant difference highlights the strong evidence of censorship in the measurements. Additionally, Fig. 6.8 shows that the ratio between the unbiased means and measured (biased) values of averaged hop lengths grows with shear velocity. This further demonstrates that experiments with higher stage values are subject to more imposed experimental censorships.

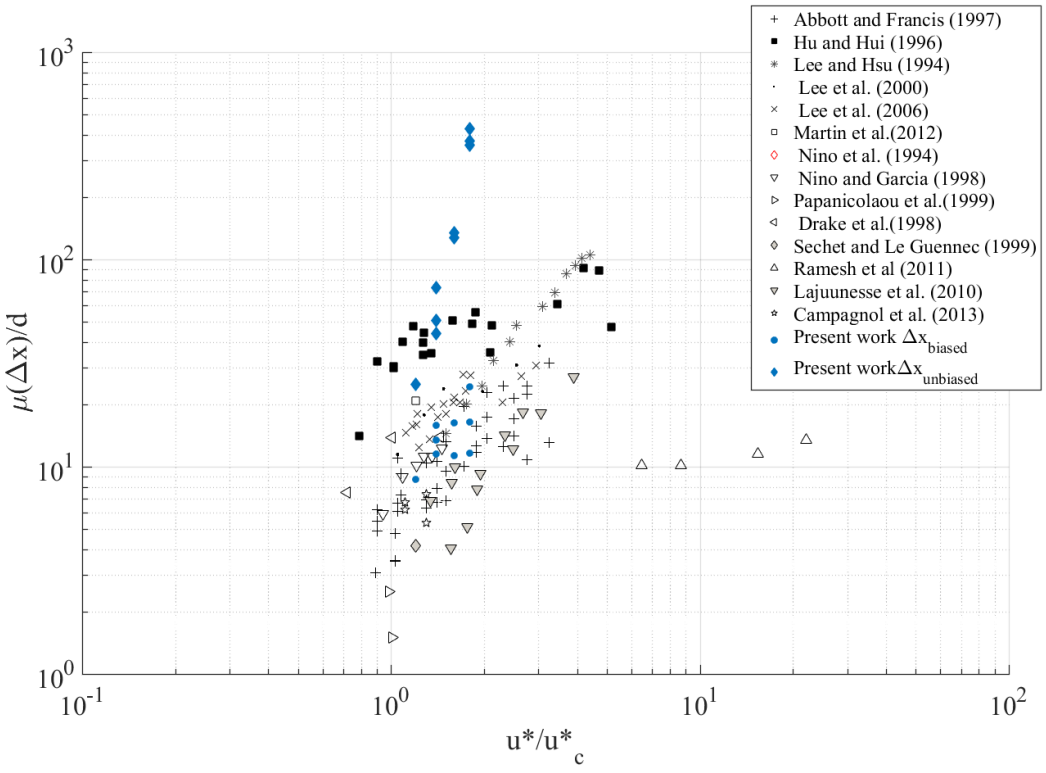

Figure 6.8 Variations of biased and unbiased mean values of hop lengths with shear velocity, comparison among different literature data.

6.4 Hop duration (Time of motion)

Probability distribution of time of motion for complete hops is given in Fig. 6.9. *Martin et al.* [2012], *Fathel et al.* [2015], and *Furbish et al.* [2016] reported that the distribution of hop travel times was best approximated by an exponential function. In this study, an exponential form did not match the distribution of hop durations. Despite the different types of distribution in the present study and the cited works a peak at origin was found similarly for all the measurements of hop duration suggesting the presence of many short intermediate trajectories in the experimental data. As discussed before, hop length measurements suffer from the experimental censorship and thus, by definition, measurements of their durations are also biased (see Fig. 6.4) and the validity of such distribution can be also questioned.

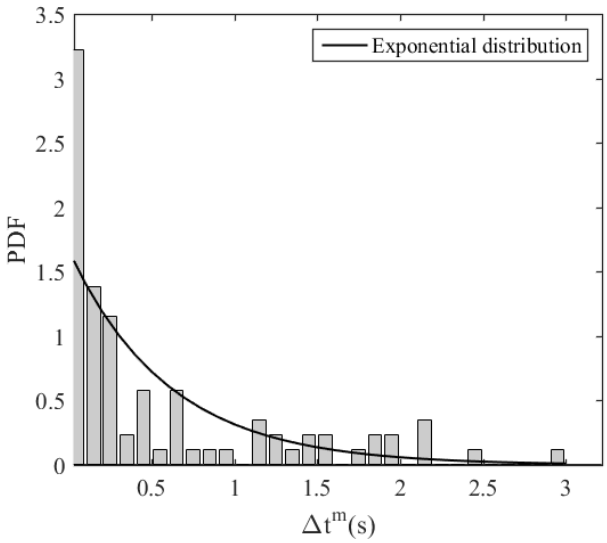

Figure 6.9 Probability distribution of complete times of motion. Results from Experiment R10.

Complete hop lengths were plotted against their times of motion in Fig. 6.10a in which the nonlinear relationship between hop length and its duration (also found by *Fathel et al*. [2015], and *Furbish et al.* [2016]) demonstrates an increase of complete hop length with the latter. As the first trend, hop lengths were growing rapidly for Δt^m=0-5s and for the second one much slower increase of hop length for Δt^m >5s was observed. Similar behavior becomes also obvious

from Fig. 6.10b where a steep increase of hop duration with hop averaged velocity is evident for Δt^m =0-5 and then the velocity nearly flattened out for Δt^m > 5s. Fig. 6.10 also shows that short travel times are in general associated with small hop lengths and small velocities where particles are in frequent interactions with the bed. Although the experimental setup did not enable side visualization, yet it is expected that the dominant types of bed-load transport for such hops were rolling and sliding. The longer times of motion, on the contrary, result in farther distances between entrainment and disentrainment when particles find the necessary time to reach higher velocities and overcome the interactions with the bed and consequently travel longer. The predicted dominant mode of transport for these conditions could be expected to be saltation.

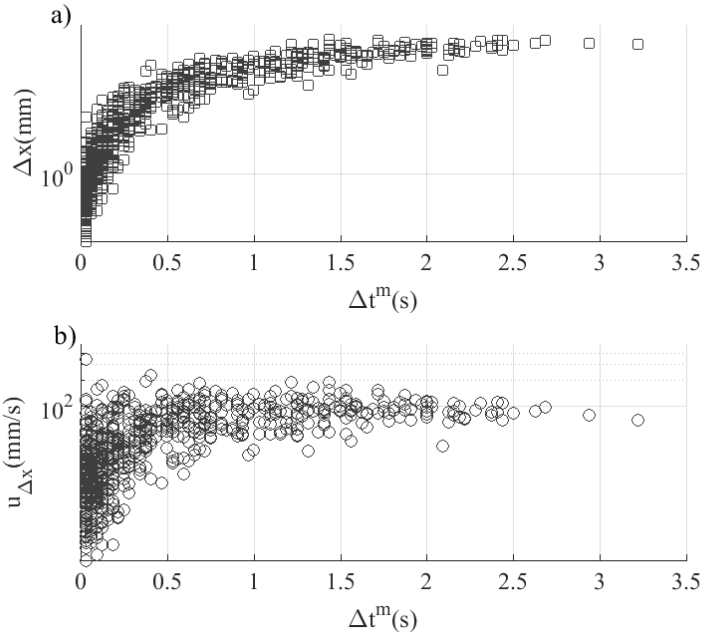

Figure 6.10 a) hop duration vs hop distance, b) hop duration vs hop averaged velocity. Data of all experiments.

The correlational analysis makes one expect a cross-effect in censorship due to the finite imaging window size where long hop lengths and their associated durations are censored (see the tail in Fig. 6.10a). The longest time of motion in our experiments was measured as 3.2s, significantly shorter than the duration of recordings (50 s) suggesting that the time scale of observation did not bias the results.

In order to evaluate the cost of spatial censorship, unbiased mean values of hop durations were also reconstructed as [*Ballio et al*., 2017]:

$$\Delta t^{m}{}_{\text{unbiased}} = \sum T_i^m \Big/ N_e \tag{6.3}$$

where T_i^m is the total duration of motion for particle *i*. The biased and unbiased averages of complete times of motion were normalized for each experiment $\mu(\Delta t^m)u^* / d$, and their variations with shear velocity are presented in Fig. 6.11.

As shown in Table 6.1, and Fig. 6.11, the true mean value of time of motion is at least twice as large as the biased measurements. The variation of mean biased time of motion demonstrates a weak increasing trend with higher shear velocities whereas, the unbiased value of hop duration was associated with a steep rise. Results in the present study contrast with the dispersed data of *Lajeunesse et al*. [2010] where no specific trend was observed for the variation of hop duration.

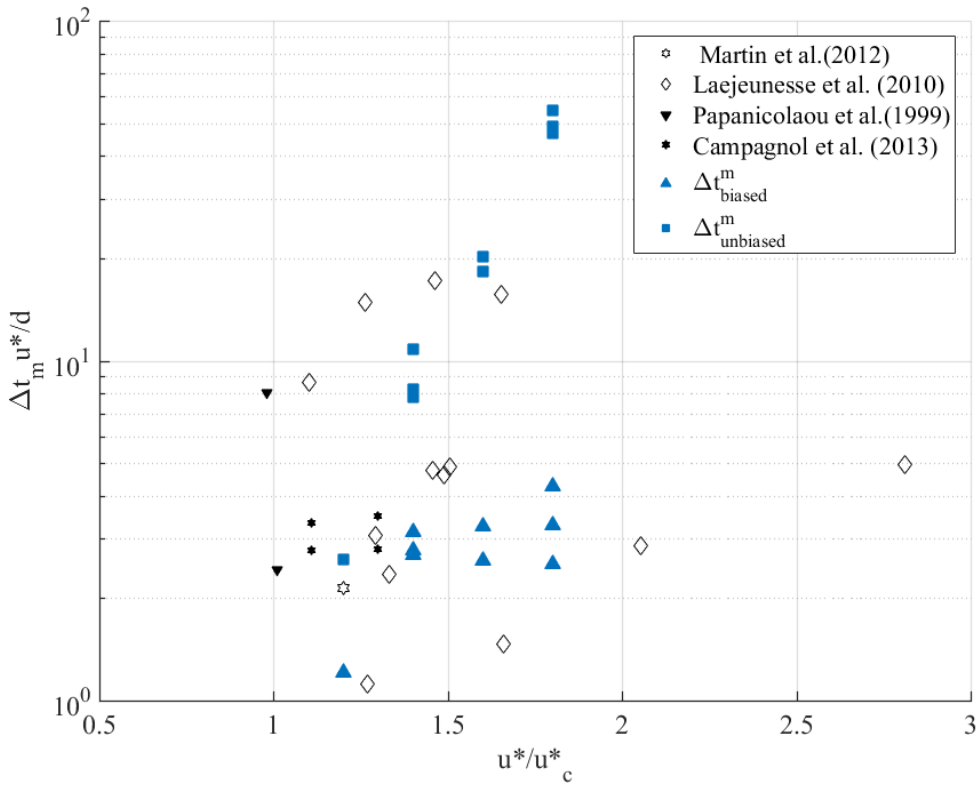

Figure 6.11 Variation of normalized averaged hop durations (biased and unbiased values) with shear velocity, comparison among different literature data.

6.5 Time of rest

A literature survey indicated that little attention was paid to quantify particle resting time and most of previous observational studies focused on particle motion. In this study, the framework was used to measure times of rest between subsequent disentrainment and entrainment events. Probability distribution of resting times are shown in Fig. 6.12. A distribution with a peak at origin and a tail toward higher values was also observed for time of rest as the counter part of hop duration. A comparison between Fig. 6.9 and Fig. 6.12 indicates that in general, within the observation scale most of measured particle motions and rests are short in duration. Nevertheless, the longer tail in Fig. 6.12 suggests the existence of relatively long rests (Δt^r >9 s) in contrast to the motion duration. The longest rest in this study was measured as 29 s suggesting that the 50 s of observation may not be enough to capture possible long rests and thus hop rests are suggestively biased by the time scale of experiments. The investigation of censorship for time of rest is out of the scope of the present study. The variation of normalized time of rest $\Delta t^r u^* / d$ was analyzed for a range of increasing shear velocities in Fig. 6.13 showing that the mean value of hop rest is decreasing for higher discharges. This finding is consistent with that of *Nino and Garcia* [1998] who expressed that the intensity of near bed turbulence increases with shear velocity, and as a result the resting particle is driven into the motion shortly after a disentrainment.

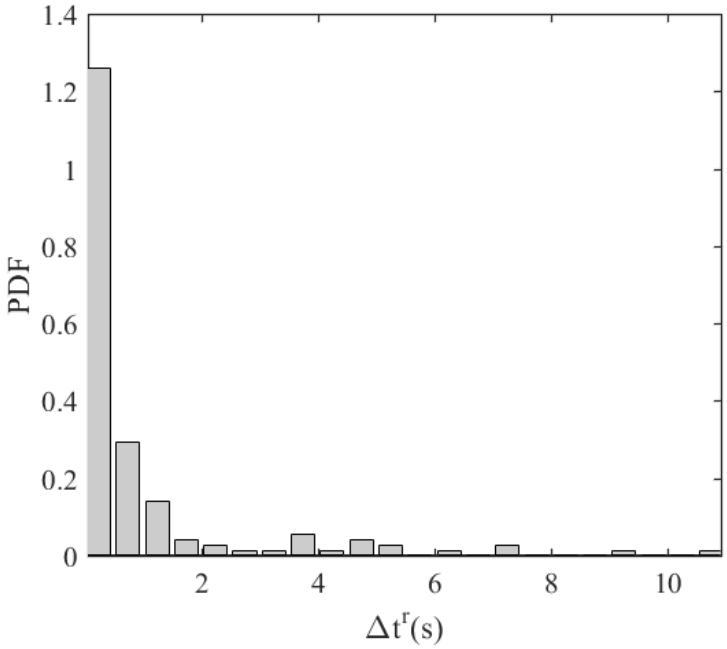

Figure 6.12 Probability distribution of complete times of rest. Results from Experiment R10.

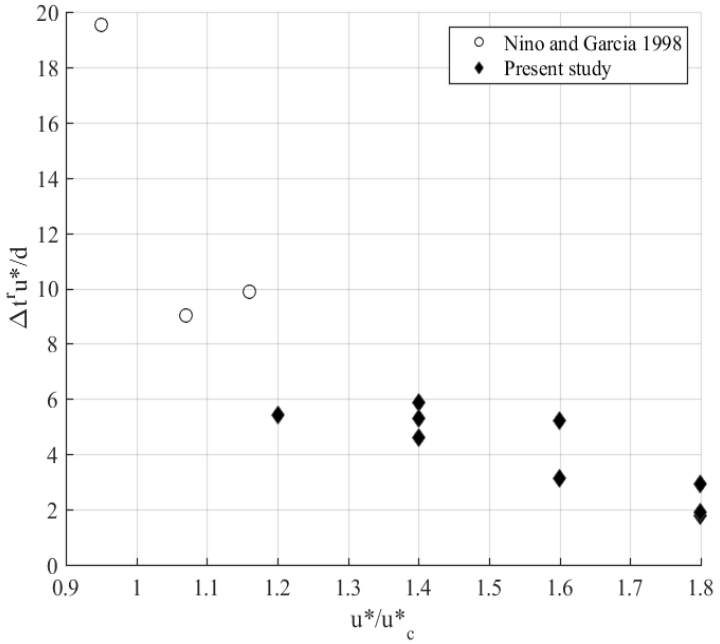

Figure 6.13 Variation of normalized time of rest with stage value.

6.6 Lagrangian time porosity

From a Lagrangian standpoint, time porosity can specify the relative duration of motion and rest periods of a particle or a group of particles. Strictly speaking, the Lagrangian movement porosity $\varphi_I^m(i)$ could not be computed from (2.7) due to the limitations of the observation window where each particle was observed only for a fraction of the total time. However, one can operationally estimate the temporal porosity for a single particle as $\varphi_{TA}^m(i) \approx T_A^m(i)/T_A(i)$, where T_A^m is the total time of movement for particle i during the time it was detected within the observation area A. Figure 6.14 shows the probability distribution of φ_{TA}^m. The plot indicates that $\varphi_{TA}^m = 1$ is the most probable value, corresponding to particles that never experienced periods of rest within the measuring space-time window. This result is, however, not representative of the behavior of a particle and is again connected to the limited length of the observation area, hence generating a strong bias of the distribution.

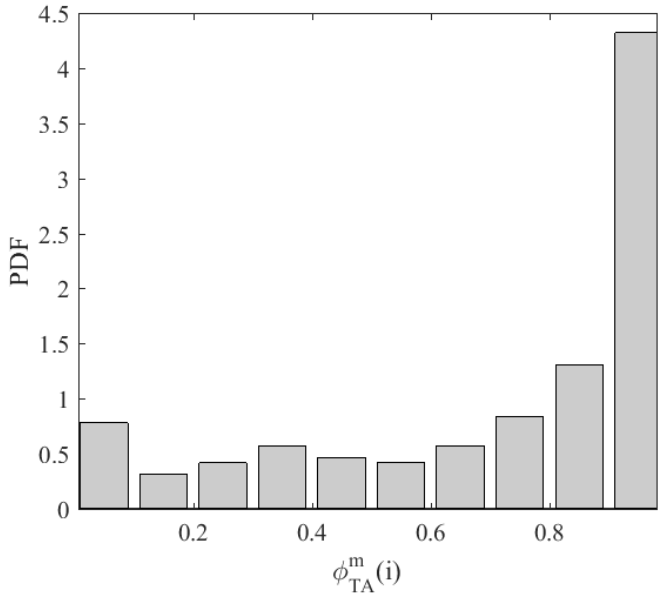

Figure 6.14 PDF of Lagrangian time porosity (Experiment R10).

The next task is to estimate the asymptotic value ϑ^m for the Lagrangian time movement porosity. On the basis of the available data, the only possible expression among the alternatives discussed in chapter 2 is evaluating ϑ^m through $\{\varphi_T^m\}_A$. Calculating the latter, a value of 0.724

is obtained. However, it should be noted that values for $\varphi_{TA}{}^{m}(i)$ for the different particles of the sample were not calculated over a unique T value, thus biasing a straightforward application of (2.22) that was derived under the hypothesis of the same observation time for all the particles. In other words, the limited observation area introduced the correlation (that was not embedded in (2.22) between the time spent within A and the time spent in motion. To overcome this, the sample average has to be operationally evaluated as:

$$\vartheta^{m} \cong \frac{\sum_{i=1}^{N} T_A^{m}(i)}{\sum_{i=1}^{N} T_A(i)} \tag{6.4}$$

In this way, a value of $\vartheta^{m} = 0.530$ is obtained.

The same procedure was applied to all the experiments. Variation of ϑ^{m} with shear velocity is given in Fig. 6.15 where an increasing trend is observed. This clearly sets out that higher fluid forces increase the relative duration which a particle spends in motion.

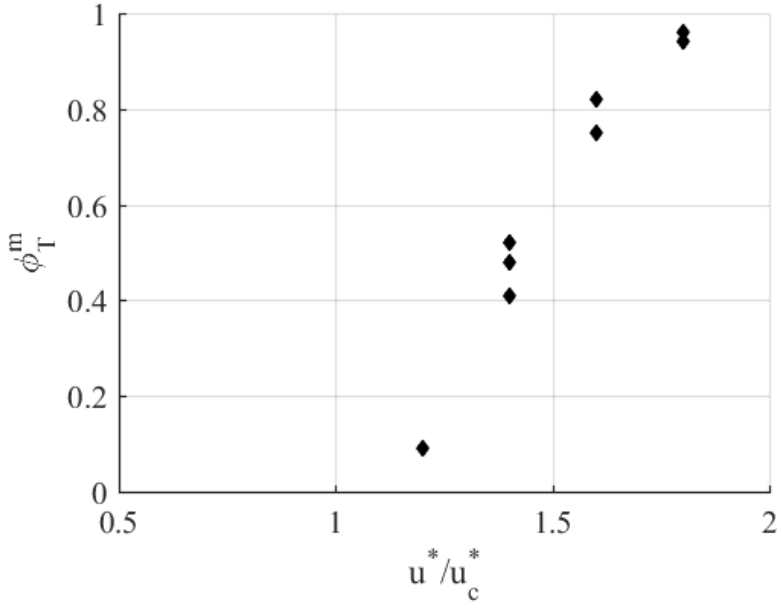

Figure 6.15 Variation of Lagrangian porosity with stage value.

6.7 Synthesis

Statistics of particle hops were obtained for all the performed experiments. Distributions were explored and mean values of the hop properties (length, duration) were computed from the distributions. However, many incomplete hops were observed when a particle crossed the boundaries of the observation area. Mean values computed above were therefore considered biased, because many particle hops had to be excluded from the samples as non-completely observed (incomplete trajectory). Unbiased average values of hop lengths and hop durations were calculated, and results proved that these values were significantly higher than measured (biased) ones, further highlighting the significant impact of censorship. The relatively long rests measured in this study suggested that the time scale of observation can also bias the results of time of rest. Biased mean values due to the spatial censorship were reconstructed for the range of experiments performed in this study, yet future studies should account properly for the impact of time censorship in the measurements of resting times. Lastly, using the arguments above, due to the impact of censorship it is difficult to accept if the reported results of different experimental studies (including those presented here) are truly representative of distribution forms of hop length and duration.

Main findings of this chapter are summarized below:

- A clear separation between the distributions of instantaneous velocities of moving and still particles indicated the efficiency of the proposed criterion for the definition of motion and rest
- A comparison between the results of particle velocities indicated that on average velocity of entrained particles over a fixed bed configuration is higher than those related with a mobile bed. It was also observed that particle velocity increases with shear velocity
- Scale analysis of hop length and hop duration indicated that the mean and standard deviation values increase as the spatial scale is enlarged. It also reflects how the finite image size biases the measurements of hop length and hop duration
- The ratio between the biased and unbiased mean values, indicate that spatial censorship significantly alters the statistical results

- The average of biased and unbiased values of hop length and hop duration were found to be increasing with shear velocity. The unbiased values were associated with a much steeper trend
- Correlational analysis suggested that short durations are in general associated with small hop lengths and small velocities while the longer time of motions were positively correlated with increased hop distances
- Resting times were shown to be decreasing with increasing shear velocities, and additionally they were found to be impacted by the time scale of observation.
- Lagrangian time porosity was increased with stage value showing that higher values of shear velocity increase the total duration of particle in motion

Table 6.1 First order statistics (mean values) of Lagrangian measurements together with the unbiased values.

Exp.	u^*/u_c^*	complete	incomplete	$\mu(u_1)$ (mm/s)	$\mu(\Delta x_{complete})$ (mm)	$\mu(\Delta x_{incomplete})$ (mm)	$\Delta x_{unbiased}$ (mm)	$\mu(\Delta t^m{}_{complete})$ (s)	$\mu(\Delta t^m{}_{incomplete})$ (s)	$\Delta t^m{}_{unbiased}$ (s)	$\mu(\Delta t^r_{complete})$ (s)	$\mu(\varphi^m_{TA})$ $(-)$
R17	1.2	87	60	70.54	26.05	103.10	75.13	0.49	1.25	1.04	2.19	0.09
R10	1.4	106	224	94.25	40.14	99.37	152.82	0.53	0.97	1.58	1.13	0.41
R11	1.4	125	230	85.82	34.56	99.25	132.11	0.52	1.06	1.50	0.89	0.48
R12	1.4	87	248	104.06	47.49	129.74	220.05	0.60	1.17	2.07	1.02	0.52
R7	1.6	92	491	116.82	48.90	168.46	402.84	0.55	1.39	3.39	0.53	0.82
R8	1.6	97	529	121.27	33.95	160.54	381.07	0.43	1.27	3.08	0.87	0.75
R1	1.8	42	679	152.99	34.72	196.17	1064.46	0.37	1.24	6.79	0.42	0.94
R2	1.8	51	1085	153.65	49.21	204.34	1115.51	0.48	1.29	7.10	0.26	0.96
R3	1.8	46	1557	158.49	72.73	190.83	1286.78	0.62	1.17	7.92	0.28	0.96

. Table 6.1 Second order statistics (standard deviation) of Lagrangian measurements.

Exp.	u^*/u_c^*	No. $\Delta x_{complete}$	No. $\Delta x_{incomplete}$	$\sigma(u_1)$ (mm/s)	$\sigma(\Delta x_{complete})$ (mm)	$\sigma(\Delta x_{incomplete})$ (mm)	$\sigma(\Delta t^m{}_{complete})$ (s)	$\sigma(\Delta t^m{}_{incomplete})$ (s)	$\sigma(\Delta t^r_{complete})$ (s)
R17	1.2	87	60	45.00	23.01	33.71	0.53	0.78	5.29
R10	1.4	106	224	52.01	32.77	44.13	0.61	0.80	2.28
R11	1.4	125	230	49.33	30.55	32.08	0.61	0.85	1.84
R12	1.4	87	248	55.74	37.00	40.18	0.76	0.89	1.82
R7	1.6	92	491	58.64	43.90	37.21	0.63	0.82	1.07
R8	1.6	97	529	62.60	38.75	41.64	0.58	0.76	2.07
R1	1.8	42	679	69.62	45.94	46.39	0.57	0.62	0.60
R2	1.8	51	1085	69.31	49.17	42.38	0.63	0.59	0.44
R3	1.8	46	1557	70.84	67.03	46.30	0.61	0.60	0.61

Chapter 7 Eulerian measurements

One of the main goals of the investigation of bed-load kinematics at small scales is to derive primitive quantities whose combination results in the calculation of sediment transport rate. Compared to field conditions where the sediment transport rate is typically measured over relatively long temporal scales by traps or indirect systems [*e.g., Garcia et al.,* 2000; *Rickenmann and McArdell,* 2007; *Krein et al.,* 2008; *Turowski,* 2010], performing experiments in a controlled environment (such as flume experiments) provides unique resolution capabilities to measure the entrainment rates and fluxes of sediments over various temporal and spatial scales [*e.g.,* Frey *et al.,* 2003; *Böhm et al,.* 2006; *Zimmermann et al.* 2008]. In this chapter, a series of Eulerian indicators of bed-load transport defined in chapter 2 will be analyzed. Combined with the measurements of these quantities, their scaling properties will be investigated and results will be compared with previous literature findings.

7.1 Entrainment/Disentrainment rates

After labelling particle motion (see the criterion of labelling in section 5.2), instants of entrainment and disentrainment were determined (obviously, with a temporal resolution depending on the frame rate of the camera). As depicted by Fig. 7.1, for a single particle, transition from label 0 to 1 and transition from 1 to 0 identify particle entrainment and disentrainment events respectively. Let one consider one sample experiment, test R10. Several particles were present and thus entrainment and disentrainment events were distributed in time and in space. Fig. 7.2 shows the progressive number of entrainments and disentrainments. For the presented experiment, after 50 seconds of observation a total number of 161 entrainments and 169 disentrainments were detected. The higher number of disentrainments indicates that in overall the experiment was associated with a slight deposition of particles.

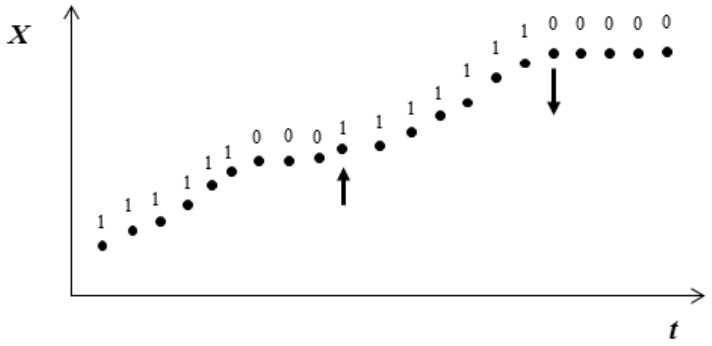

Figure 7.1 Definition sketch for particle motion (labels 0/1), and examples of entrainment event (upword arrow) and disentrainment event (downward arrow).

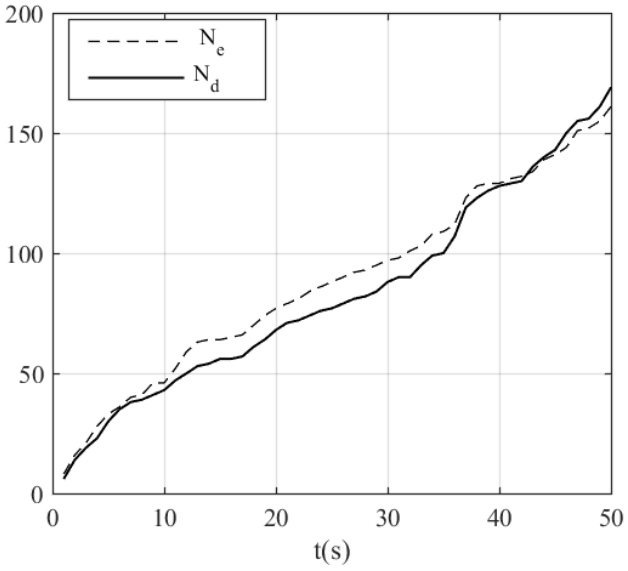

Figure 7.2 Progressive number of entrainments and disentrainments (Experiment R10).

7.1.1 Temporal variation of *E* and *D*

The Lagrangian data on single particle motion were averaged using appropriate spatial and temporal support scales (A and Δt, respectively, identifying an area of the bed and a sampling interval) to obtain values for the entrainment and disentrainment rates. Time averaged entrainment and disentrainment rates ($\overline{E}$ and $\overline{D}$) were quantified as:

$$E = \overline{E}\frac{w}{A}, D = \overline{D}\frac{w}{A} \tag{7.1}$$

Where $\overline{E}$, $\overline{D}$ can be calculated based on any given Δt from (2.30) and (2.31).

An example of time evolution of the entrainment and disentrainment rates for experiment R10, is depicted in Fig. 7.3 considering A = 270×200 mm^2 and different values of Δt. The shorter time scale used (0.05 s) was only slightly larger than the camera frame (1/32 s) and resulted in very low values of N_e and N_d: for example, the E value computed with (7.1) for just one entrained particle was equal to 0.007. The larger temporal scale (Δt=0.7s), which is larger than the mean duration of measured intermediate trajectories in this experiment (see Table 6.1), obviously enabled more entrainment and disentrainment events to occur in a single time interval; a value of E equal to 0.005 would in this case correspond to 10 entrained particles. Decreasing the temporal scale of sampling introduces less averaging of the fluctuation pattern: the signal for the lower time scale is characterized by noticeable intermittency (defined as the presence of zero values in the time series for E and D) and higher spikes. In addition to the temporal scale, the spatial one also affects the fluctuation pattern of entrainment and disentrainment rates. This is illustrated by Fig. 7.4 which is the counterpart of Fig. 7.3: a fixed temporal scale of 0.4 s was used with two different spatial scales (A=25×200 mm^2 and A=270×200 mm^2). The width of observation in streamwise direction was constant. The low peaks at 0.003 for E and D correspond to just one particle for the smaller area; for the larger one, values of 0.005 would correspond to 6 entrained or disentrained particles. Evidently, as for times, a larger spatial scale produces more averaging of fluctuations and reduces the intermittency of the entrainment or disentrainment process.

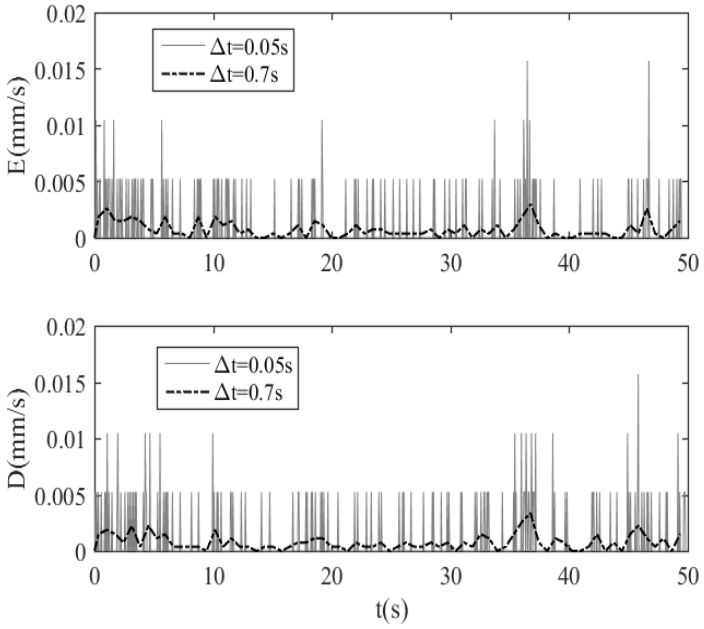

Figure 7.3 Temporal variation of E and D for fixed spatial scale (A=270×200 mm^2) and changing the time scale.

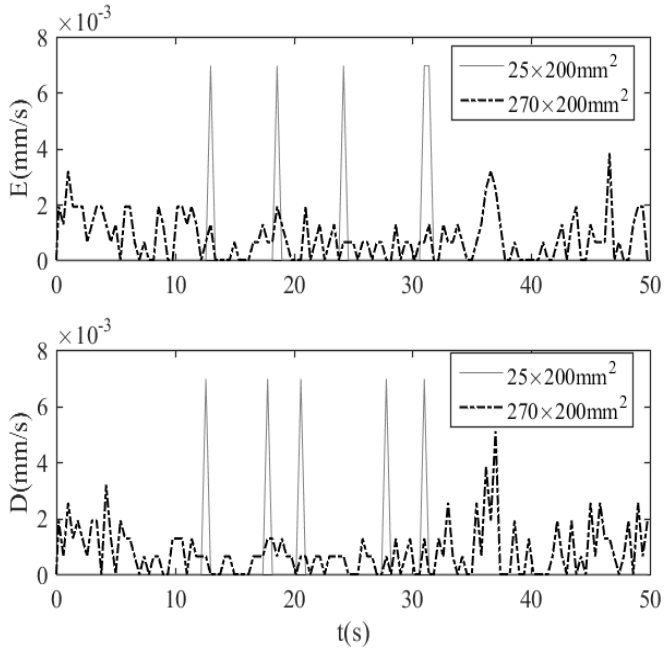

Figure 7.4 Temporal variation of E and D for fixed time scale (Δt=0.4 s) and changing the spatial scale.

7.1.2 Scale dependence of moments of *E* and *D*

The first and second-order statistical moments (mean and standard deviation) of E and D were systematically analyzed for a range of temporal and spatial scales. The dependency of moments on the temporal scale was investigated using the following Δts: 0.05, 0.1, 0.2, 0.5, 1, 2, and 3 s; these time intervals were made dimensionless using the average duration of intermediate trajectories for the current experiment ($\Delta t = 0.61\ s$) (see Table 6.1). The spatial averaging scale for the analysis was maintained constant and equal to 270×200 mm^2. For the spatial scale analysis, a constant Δt = 0.4 s was used and the following areas were selected: 25×200, 50×200, 100×200, 150×200, 200×200, and 270×200 mm^2. All these areas had the same width of 200 mm while the scale was enlarged by increasing the length in the stream-wise direction (L) that was normalized by the average length of intermediate trajectory (Δx =47.49 mm). Results are depicted in Fig. 7.5 and Fig. 7.6. The mean values of E and D were found to be scale-independent, meaning that numbers of entrained and disentrained particles increase linearly with the spatial and temporal scale used for sampling. By contrast, the standard deviation of the quantities decreases for increasing scale, reflecting the fact that averaging N_E and N_D over larger samples results in lower fluctuations. In both plots a scaling exponent close to -0.5 was obtained. *Radice et al.* [2009] proposed a mathematical derivation to support this exponent, and also provided arguments on deviations from this trend. They showed that for a non-correlated quantity the trend for the variance is an analytical power law with -0.5 exponent, with the deviation of experimental points from such trend being the effect of correlation. The values of exponents show that the E and D fields are not significantly correlated within the range of scales explored here.

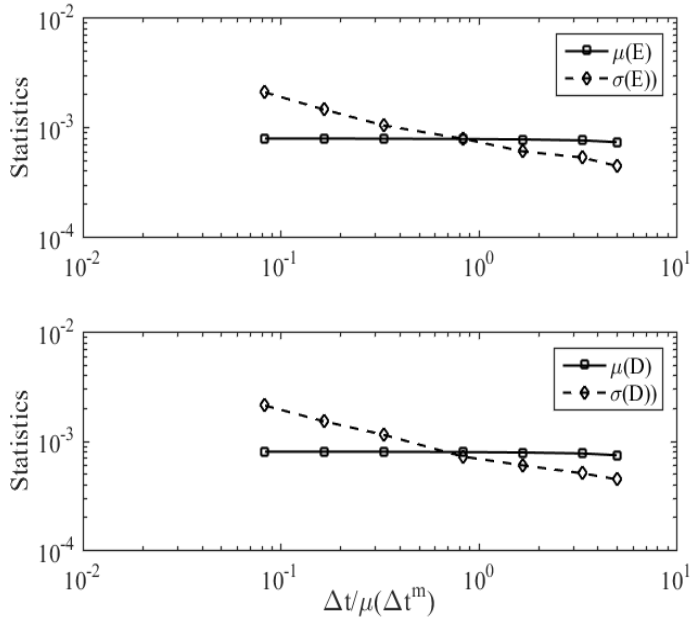

Figure 7.5 Statistics (mean and standard deviation) of *E* and *D* for different temporal scales and a fixed spatial scale (A=270×200 mm^2).

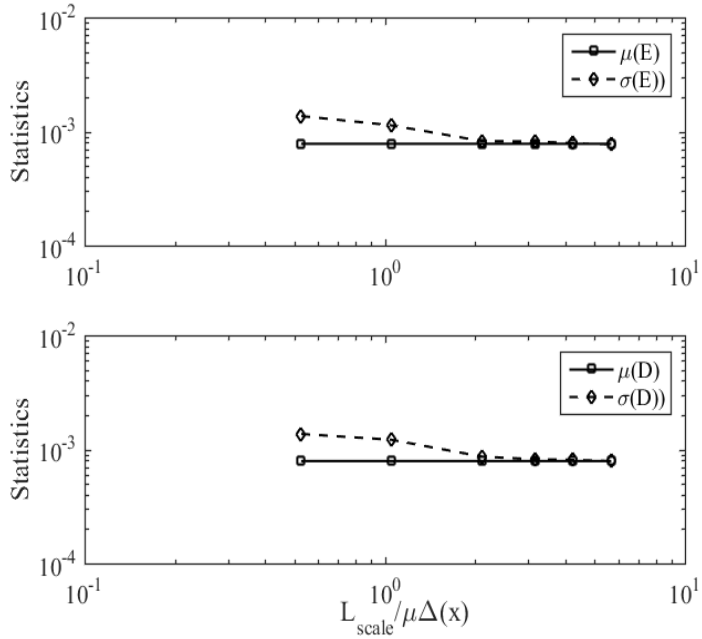

Figure 7.6 Statistics (mean and standard deviation) of *E* and *D* for different spatial scales and a fixed temporal scale (Δt=0.4 s).

7.2 Concentration and velocity of moving particles

Fernandez-Luque and Van Beek [1976], *Seminara et al*. [2002], *Parker et al*. [2003], and *Radice and Ballio* [2008] expressed the solid discharge as the product of the areal concentration of sediments and of the grain velocity. In the following, first, the Eulerian concentration and velocity components will be individually measured and investigated within the proposed framework. These measurements will be then ingredients to calculate the Eulerian solid discharge. Lastly, sediment flux passing a reference line will be systematically investigated. Experimental results in this study will be discussed considering a variety of scales, starting from a resolution of few particle diameters up to the entire scale of observation.

7.2.1 Eulerian Particle concentration

An example of temporal evolution of moving particles $N_A^m(t)$ (number of particles at motion at each instant within the spatial area) for test R10 is presented in Fig. 7.7. Moving particles fluctuate from a low number of about 20 particles to more than 58 particles, with an average of 37. Consistent with previous measurements [e.g., *Roseberry et al.,* 2012; *Ancey and Heyman*, 2014; *Fathel et al*., 2015], the fluctuation pattern reflects the associated balance between entrainment and disentrainment.

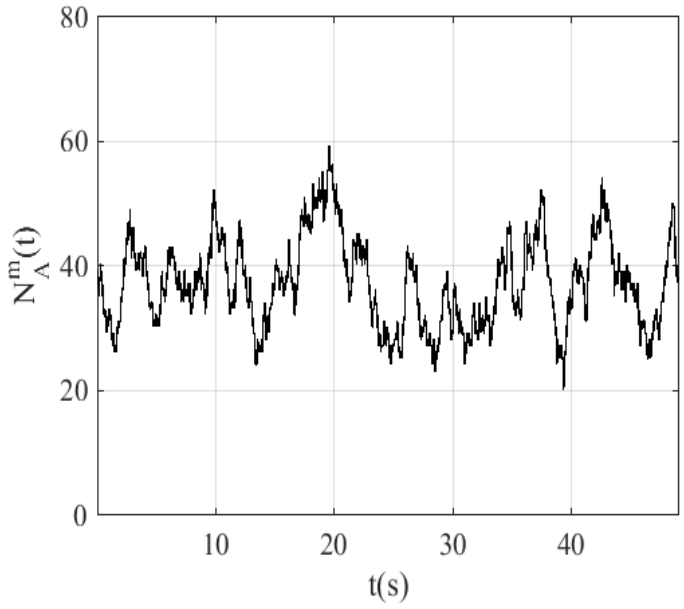

Figure 7.7 Temporal evolution of moving particles (R10).

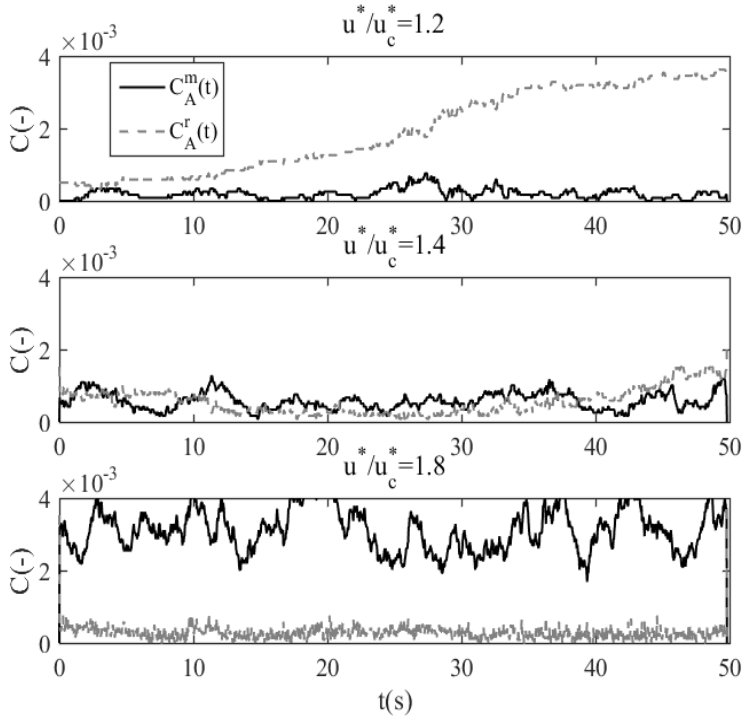

Figure 7.8 Temporal variation of particle concentration *C*. Tests in order; R17, R8 and R10.

An example of temporal evolution of dimensionless particle concentrations for three stage values are given in Fig. 7.8. For the lowest stage value $u^*/u_c^* = 1.2$ the concentration of resting particles is higher than those at motion suggesting that the associated shear velocity does

initiate motions for many particles. On the contrary, for the highest stage value $u^*/u_c^* = 1.8$ most of the particles present in the observation domain are at motion. For the experiment with $u^*/u_c^* = 1.4$ there is an approximate balance between the moving and still particles. The corresponding scale A in Figs. 7.7 and 7.8, was initially chosen to be sufficiently large (270×200 mm^2) so that during any small time-interval Δt, the difference between particles entering and exiting the reference area was relatively low compared to the total number of particles present in the support scale A.

Fig. 7.9 represents the mean and coefficient of variation (as the ratio of standard deviation to mean) as a function of stage value. Additionally, a comparison of the present data with the erodible bed experiments of *Radice and Ballio* [2008] and *Radice et al*. [2013] is given. Presented results indicate that the concentrations of moving particles increased by an order of magnitude for the range of explored stage values. That is because a higher value of shear velocity allows for more particles to stay at motion within the observation scale. This can be also depicted by Fig. 7.8 in which the balance between the number of resting and moving particles changes with shear velocity. Additionally, Fig. 7.9 shows that in the cited experiments with mobile bed configuration concentration of moving particles are on average higher than in the present study. This difference is due to the nature of mobile beds in which bed particles can be eroded and contribute to the transport flux. In all experiments, the coefficient of variation is decreasing with stage value.

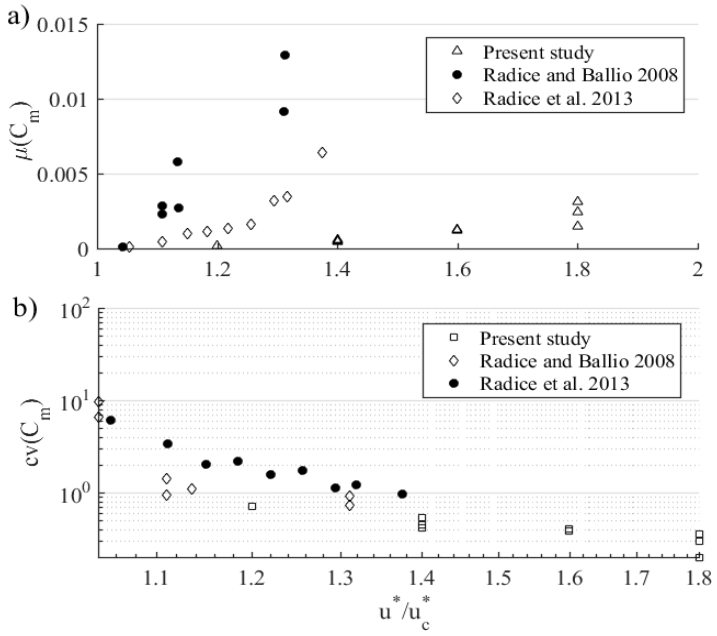

Figure 7.9 Variation of a) average and b) coefficient of varriation of concentration with stage value. Note the log scale for $cv(C_m)$.

7.2.2 Eulerian particle velocity

Fig. 7.10 indicates the fluctuation patterns of the Eulerian velocity associated with the concentration rates depicted in Fig. 7.8. Eulerian velocity $u_A^m(t)$ is calculated as the average of instantaneous velocities of moving particles $N_A^m(t)$ at each instant in the time series. As indicated in Fig. 7.10 with the increase of stage value, particle velocity also increases and the pattern of velocity fluctuation becomes smoother due to the averaging over more velocity values.

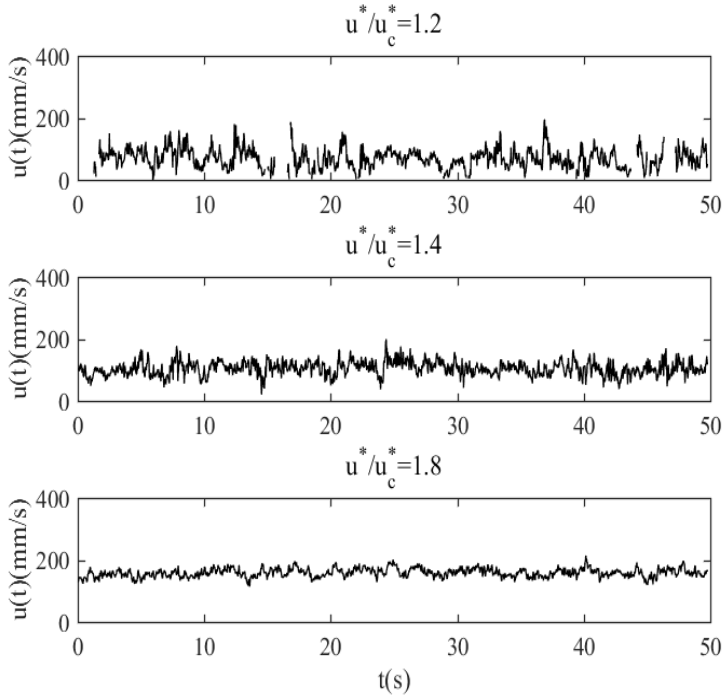

Figure 7.10 Temporal evolution of instantaneous velocity corresponding to concentrations depicted in Fig. 7.8.

An example of autocorrelation functions of $C_A^m(t)$ and $u_A^m(t)$ is given in Fig. 7.11. Considering the integral scale of correlation, these functions decay at about 2 and 1, for the concentration and velocity respectively. A comparison between the autocorrelation functions and the time scale of observation in these experiments (50 s) suggest that quantities are not affected by the temporal domain of observation. The variation of normalized velocity u_A^m / u^* was also compared with stage values in Fig. 7.12. Presented results suggest that except for the point with the lowest discharge ($u^* / u_c^* = 1.2$), particle velocity increases with stage values (The reason for the deviation of this point from the trend is described in section 3.2.3). This finding agrees with those obtained for the Lagrangian analysis of velocities (see Table 6.1).

A comparison between Fig. 7.9 and Fig. 7.12 indicates that Eulerian concentration and velocity both increase with the stage value. However, the rate of growth is much higher for the concentration of particles. This is in agreement with the erodible-bed data of *Radice and Ballio*

[2008] who also observed that concentration is more variable with shear velocity. The trend of variation of Eulerian velocities in Fig. 7.12 is aligned with the earlier finding of Lagrangian analysis which showed that the velocity of moving particles is higher above a fixed bed compared to those obtained over an erodible bed.

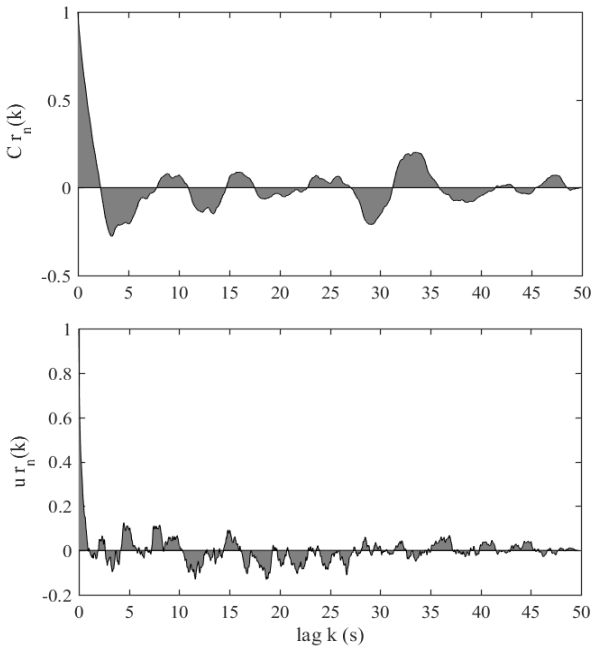

Figure 7.11 Autocorrelation functions of concentration and velocity (R10).

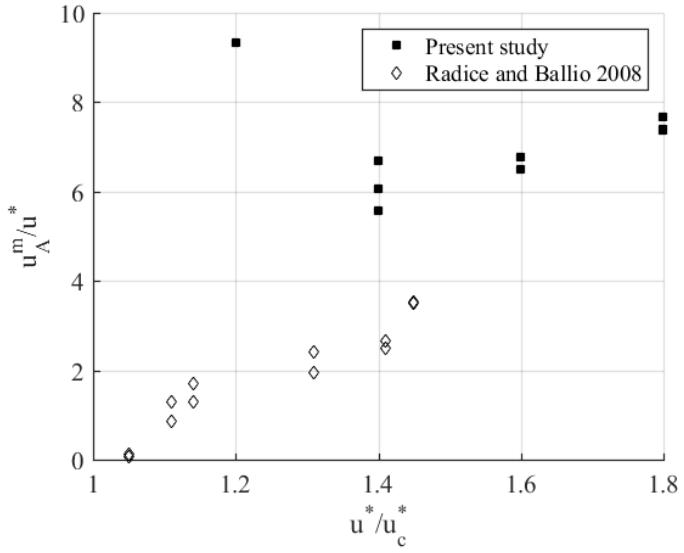

Figure 7.12 Eulerian average velocity as a sfunction of stage.

7.2.3 Scale analysis of statistical moments of concentration and velocity

First- and second-order statistical moments (mean and standard deviation) of C and u were systematically analyzed for a range of spatial and temporal scales (Fig. 7.13). Due to similar behavior of temporal and spatial scales on averaging the properties, only results of spatial scale analysis will be documented in this study.

The dependency of moments on the spatial scale was investigated using the same spatial support scales used in the analysis of E and D (see section 7.1). All these areas had the same width of 200 mm while the scale was enlarged by increasing the length in the stream-wise direction (L) that was normalized by the total length of the frame in streamwise direction (270 mm).

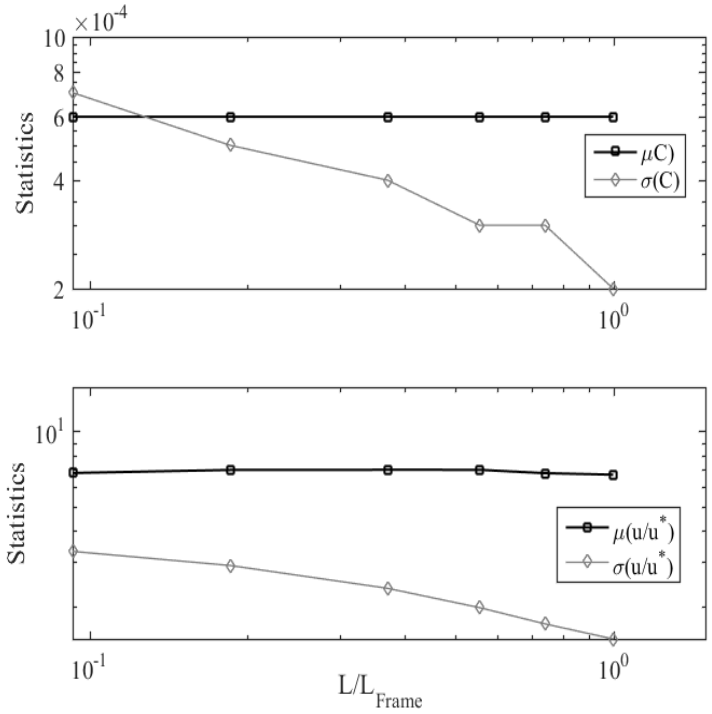

Figure 7.13 Statistics (mean and standard deviation) of C and u for different spatial scales.

As exploited in Fig. 7.13 the scale analysis of sediment flux components indicates that under weak bed-load transport and spatially uniform conditions the mean values of concentration and

velocity are independent of the scale of observation. Additionally, it is shown that the standard deviation decreases for both parameters. The scaling exponent of -0.50 is similar to scale analysis of E and D, indicating that C is uncorrelated at least within the ranges of investigation whereas the 0.5 value of exponent for the velocity indicates some deviations mainly due to the spatial correlation of velocity field.

7.3 Solid discharge across a line perpendicular to the flow direction

This section explores the results of calculated sediment flux across a line perpendicular to the main flow (2.19). In addition, the spatial analysis of sediment fluxes will be given.

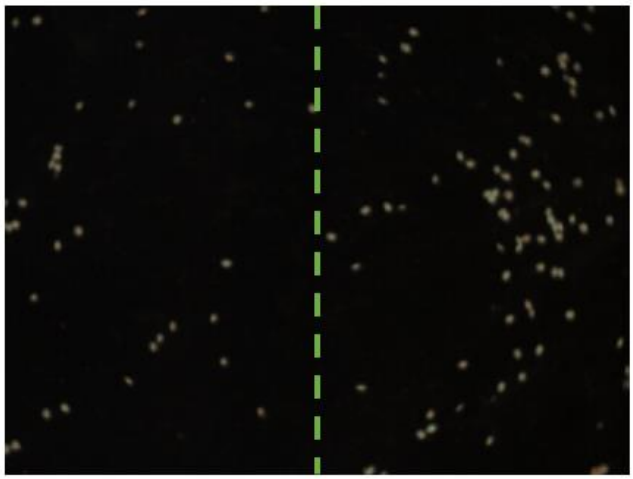

Figure 7.14 Indication of the reference line for crossing. Flow from right to left.

The temporal evolution of solid discharge was calculated for a range of Δt starting from Δt = 0.05 s up to Δt =3 s. Results are presented in Fig. 7.15 where the length of the reference line was constant (B=200 mm). The line was positioned in the middle of the frame at X=135 mm. (Fig. 7.14).

Fluctuations of patterns of sediment flux show that for small temporal scales the process is intermittent with significant number of zero sediment fluxes while for increasing Δt the total number of zero values in the time series of solid discharge reduces providing a much smoother pattern. This is similar to the findings of *Campagnol et al.* [2012] for mobile bed configuration.

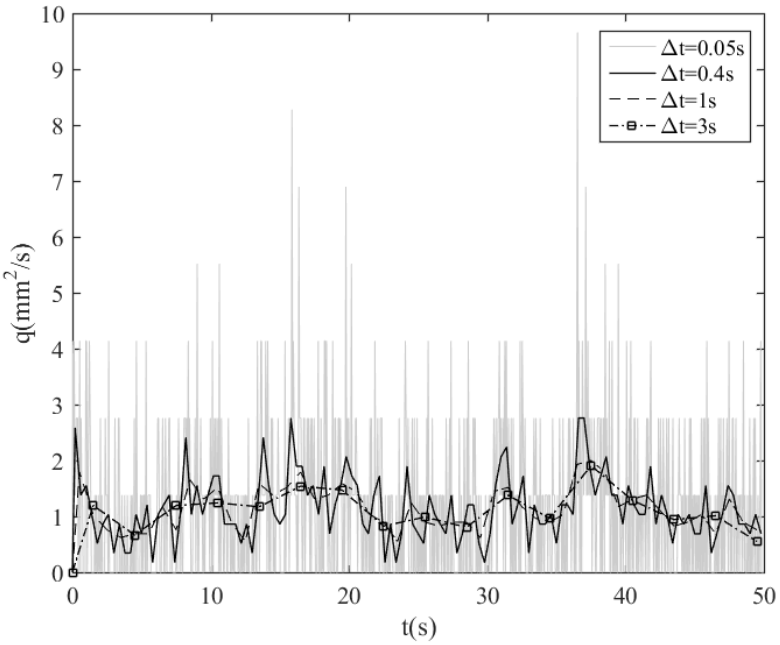

Figure 7.15 Temporal evolution of sediment flux passing through the vertical line for different values of Δt scales (Experiment R10).

The temporal evolution of solid discharge was also calculated for a range of various transverse line lengths starting from B= 5 mm up to B =200 m. The scale B was centered in the middle of the reference line and was expanded to both sides. For this analysis, the time scale was constant as Δt = 1 s. Fig. 7.16 depicts that similar to various temporal scales, the increased length of reference line also flattened out the fluctuations of spikes. The scale dependence of mean and standard deviation of q was also verified for a range of spatial and temporal scales in Fig. 7.18. The dependency of moments on the spatial scale was verified for the following transverse line lengths B=25, 50, 100, 150, 200 mm whereas the dependency of moments on the temporal scale was investigated using the following Δt= 0.05, 0.4, 0.2, 0.7, 3 s.

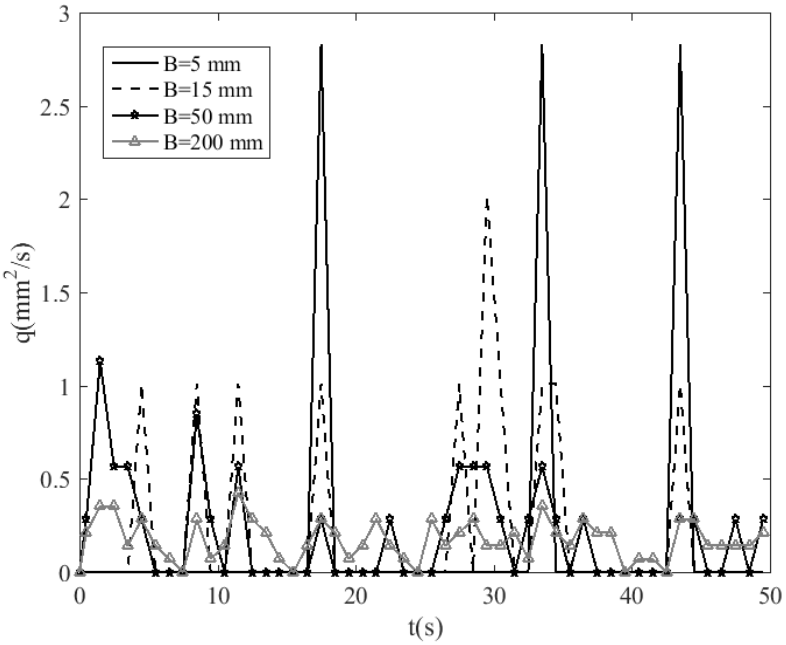

Figure 7.16 Temporal evolution of sediment flux passing through the vertical line for different values of *B*, and $\Delta t = 1$ s (Experiment R10).

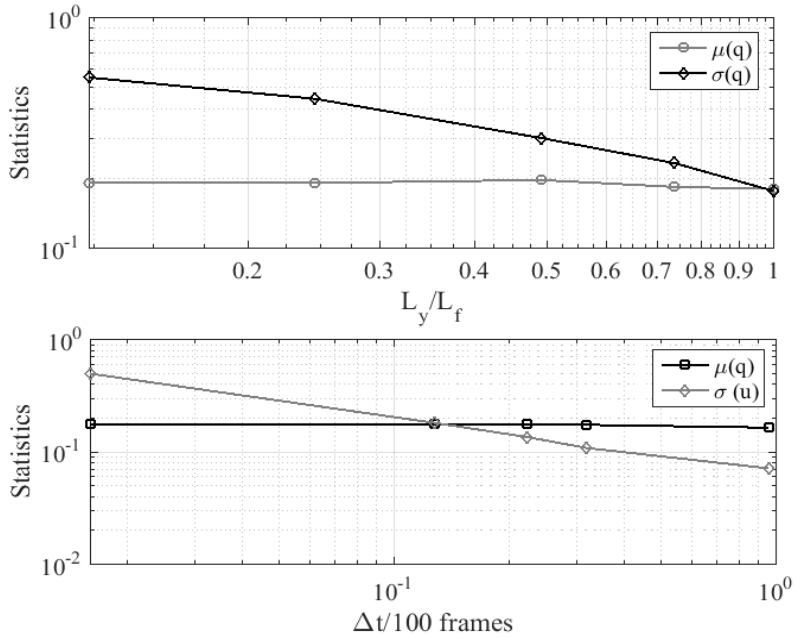

Figure 7.17 Spatial and temporal scale analysis of *q* (Experiment R10).

As depicted by Fig. 7.17, and in consistence with previous findings for other Eulerian quantities, the average of q is also independent of the temporal and spatial scales while the standard deviation is shown to be decreasing. A power law with the exponent close to -0.5 was also obtained for the scaling behavior of standard deviations, representing that fluxes are not correlated.

7.4 Feeding rates and sediment fluxes

Fig.7.18 shows a comparison among the feeding rates, sediment fluxes passing through a reference line in the middle of the frame, and Eulerian solid discharge.

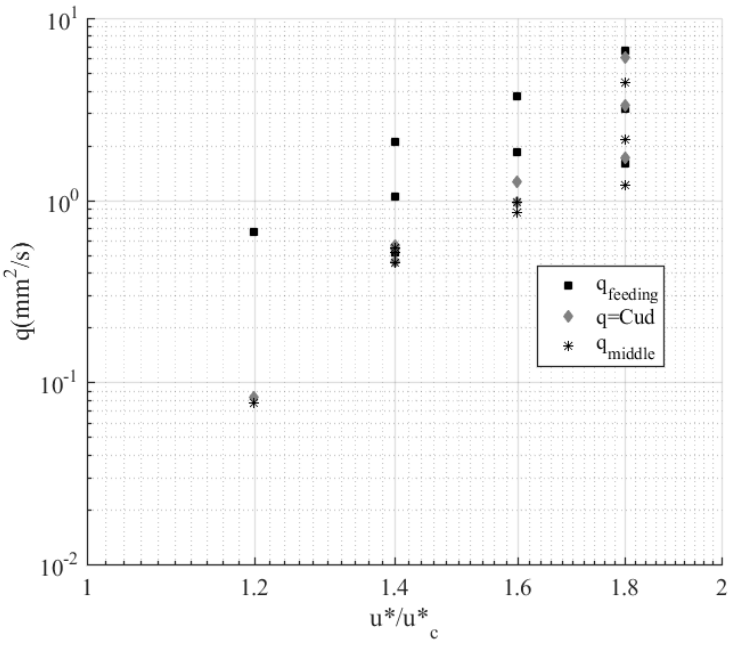

Figure 7.18 Various sediment fluxes.

As depicted above only for the experiments with the highest stage value $u^*/u_c^*=1.8$ the Eulerian sediment fluxes per unit width are almost identical to the values of feeding rates, while

for the rest of experiments fluxes of transport are lower. This comparison suggests that (3.7) might underestimate the transport capacity of the flume at low discharges.

7.5 Discussion and conclusions

Eulerian quantities of bed-load transport concerning various spatial and temporal reference scales were studied in this chapter. Temporal evolutions of entrainment and disentrainment rates, concentration and velocity, solid discharge over a reference line, and Eulerian fraction of movement were explored. Their variations with stage value were also analyzed. Scale variability was verified for the mean and standard deviation of four quantities (E, D, C, u, q). Finally, results of Eulerian measurements were compared with those obtained from a Lagrangian standpoint to prove the synergies between the two approaches. The main conclusions derived from the analysis are:

- The time series for the explored quantities (E, D, C, u, q) show that quantities are highly fluctuating for small support scales, for which the intermittency of the sediment transport process clearly emerges and high spikes are detected. For increasing support scales, the fluctuation pattern becomes ‘smoother’ due to averaging over larger numbers of quantities.
- The mean values of E, D, C, u, q are scale independent, whereas a scale dependency was found for the standard deviation of these parameters.
- The trend of variation of the standard deviation of E, D, C, q with a support scale was well approximated by a power law with exponent of –0.5, suggesting that these quantities are self-uncorrelated, at least in the ranges of scales explored in this work. These findings are consistent with those obtained in earlier works considering the flux of sediment over mobile bed.
- It was shown that the key components determining the average transport rate exhibit different behaviors when correlated to the bed shear stress: in particular, the sediment concentration is much more variable with bed shear stress than the sediment velocity

Table 7.1 Summary of Eulerian measurements.

Test	u^* / u_c^*	$\mu(C_m)$ $(-)\times 10^{-4}$	$cv(C_m)$ $(-)$	$\mu(u)$ (mms^{-1})	$cv(u)$ $(-)$	$\mu(E)\times 10^{-4}$ (mms^{-1})	$\mu(D)\times 10^{-4}$ (mms^{-1})	$q_s = \overline{Cu}d$ $(mm^2 s^{-1})$
R17	1.20	1.99	0.71	69.54	0.46	4.72	6.34	0.047
R10	1.40	4.63	0.53	94.44	0.29	9.00	8.06	0.136
R11	1.40	5.22	0.43	86.72	0.29	10.08	10.13	0.135
R12	1.40	5.78	0.41	104.59	0.22	7.92	8.31	0.181
R7	1.60	12.39	0.39	116.31	0.14	10.18	11.11	0.434
R8	1.60	12.05	0.38	120.78	0.15	11.41	11.36	0.439
R1	1.80	14.52	0.36	151.96	0.14	6.54	5.90	0.667
R2	1.80	24.09	0.30	153.14	0.10	10.28	9.49	1.112
R3	1.80	31.23	0.20	158.51	0.09	12.19	10.77	1.487

Chapter 8 Synergies between Lagrangian and Eulerian approaches

In order to prove the synergies between the two approaches and prove the validity of the framework for analysis used in the present work, results for Lagrangian and Eulerian quantities are compared in this section.

8.1 Instantaneous velocity

Suppose that there are *N* active particles in the system. From a Lagrangian point of view, first, the time average of instantaneous velocities for each particle is derived. The average of these values (average over *N* particles) can be calculated as $\{u\}$. From a Eulerian standpoint, the average instantaneous velocity of all the active particles at each instant in the time series $N_A^m(t)$ and afterwards the mean value of these averages can be calculated as $\overline{u_A^m(t)}$ which is a time averaged velocity. In principle, the time average is equal to ensemble average:

$$\{\overline{u(i)}\} = \overline{u_A^m(t)} \tag{8.1}$$

This relationship is verified in Fig. 8.1 where the measurement of velocity from the two approaches yield identical results.

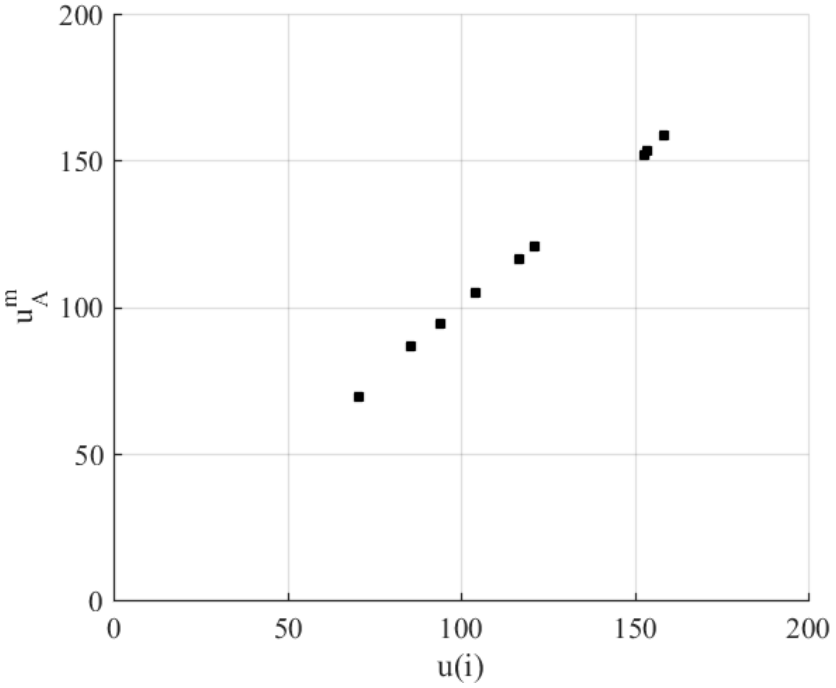

Figure 8.1 Comparison of velocities from the two approaches. Each square represents the results of one experiment.

8.2 Bulk description – Eulerian fraction of movement

Figure 8.2 shows the time series of the fraction of particles moving within the observation window, $\varphi_A^m(t)$. Its time average is 0.539, which is very similar to the Lagrangian time porosity obtained from $\left\{\varphi_T^m\right\}_A$=0.521 $\cong$ $\overline{\phi_A^m(t)}$ with 1.7 % difference. Fig. 8.2 indicates that both Lagrangian and Eulerian porosities provide identical results further proving the validity of the proposed framework.

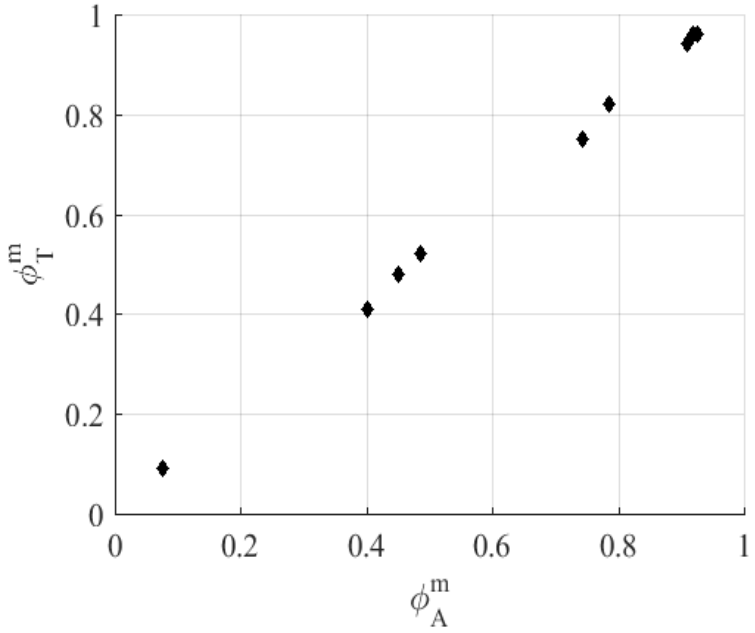

Figure 8.2. Comparison of φ_A^m and φ_{TA}^m.

8.3 Sediment flux

Sediment fluxes can be related to descriptors of particle motion through two main approaches:

i) $q \sim C \times u$ (2.16), C is the concentration and u is the particle velocity. This is a purely Eulerian relationship which can be applied at any spatial scale, as discussed in *Ballio et al.* [2014].

ii) $q \sim E \times \Delta x$ (2.34) where E is the average of (Eulerian) entrainment rate and Δx is the mean value of unbiased hop length identical to the entrainment rate calculated by (6.2). This is a mixed Eulerian-Lagrangian relationship which should be applied to scales larger than the hop lengths. The sediment flux was calculated using both equations (i) and (ii), and results are presented in Fig. 8.3.

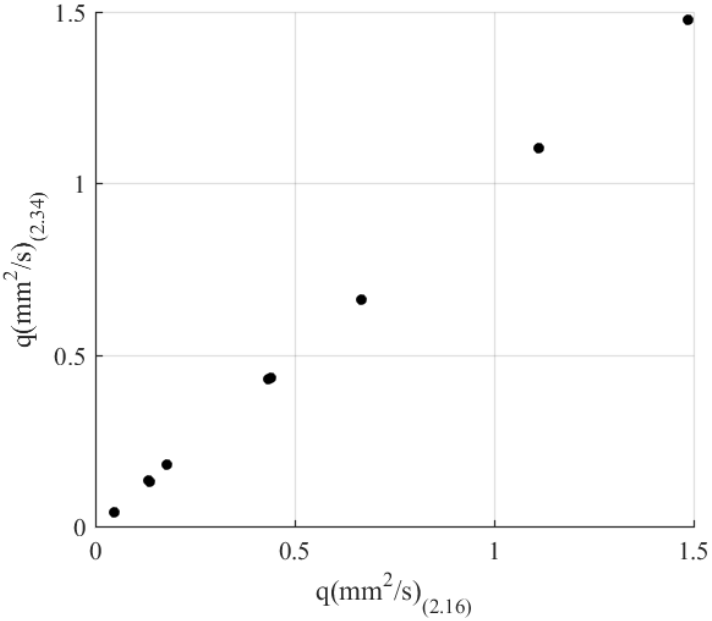

Figure 8.3 Comparison between sediment flux q derived from (2.15) and (2.34).

A comparison between the calculated sediment fluxes in this work, indicates that the two expressions are related. By comparing the different formulations, it is interesting to notice that the information on the quantity of moving particles is embedded either in the concentration C (space porosity) or in the entrainment rate E (time porosity).

In summary, a comparison between the results of Eulerian measurements and those obtained from a Lagrangian standpoint in this chapter prove the synergies between the two approaches.

Conclusions

In this study, a novel conceptual framework was used to investigate the Lagrangian and Eulerian kinematic properties of bed-load sediment particles moving over a fixed rough bed. The framework defines a number of relevant quantities, including particle instantaneous velocity, hop length and duration, rest time, concentration of moving particles, entrainment and disentrainment rates, solid discharge.

Laboratory experiments were performed where the particle motion was recorded from the top using a CCD camera, and a PTV analysis of the captured images was performed to provide the time evolution of particle position as the basis for the measurements. A significant part of the work was devoted to avoiding tracking mistakes in the data samples. For one experiment this was achieved by manually fixing the PTV errors. This operation was extremely time-consuming; therefore, for the other experiments, a visual validation procedure was used removing wrong tracks from the data sets.

The kinematic quantities were defined accounting for states of particle motion and rest. Therefore, a definition for motion recognition was given. Differently from some other studies, the criterion proposed for motion identification did not impose a velocity or displacement threshold to define particle motion, and was rather based on the stream-wise instantaneous position of a particle. A comparison between values measured using different criteria for motion identification showed that statistics of particle motion are sensitive to the criterion that one uses. This sensitivity cannot be avoided; however, its quantification may help analysis of experimental data coming from different sources.

From a Lagrangian standpoint, distributions of instantaneous particle velocity were obtained for all the performed experiments. Distributions for still and moving particles were well separated, with some overlapping that was mostly related with particle vibration around a

certain position. The shape of the obtained distributions was compared with analogous observations from the literature, suggesting that different operational conditions can lead to different distributions. In a following part of the analysis, statistics of particle hops were investigated. It was noticed that, due to the finite size of an observation area, many particle hops had to be excluded from the samples as non-completely observed; the measurements were, therefore, biased. An attempt was made to obtain better estimates of mean values for hop length and duration from the total travel length (or the total time of motion) for all the particles and the number of observed entrainment events. The estimates obtained in this way were significantly larger than those obtained from the sample of complete hops, and were shown to increase with shear velocity. Particle velocity also increased with the shear velocity, whereas the particle time of rest was decreasing. Due to the experimental censorship of particle hops, the distributions presented for hop properties (those reported by previous findings as well as those presented in this study) might not represent the true form of distributions.

Eulerian measurements were performed with reference to suitably chosen spatial and temporal scales. The variability of the first and second moments of several parameters with the support scale was verified. Quantities like the entrainment and disentrainment rates, the areal concentration and velocity and the solid discharge are highly fluctuating for small support scales while for, the larger scales, the fluctuation patterns became progressively smoother. Consistently with the results of earlier works that considered the flux of sediment over a mobile bed, it was also found that, under the explored bed-load transport conditions, mean values of the mentioned quantities did not vary with the scale of observation, while for larger scales the standard deviation was decreasing by a power law with exponent of -0.5. This finding endorsed that these quantities are self-uncorrelated, at least in the ranges of scales explored in this work. It was shown that the key components of the average transport rate exhibit different behaviors when correlated to the bed shear stress: in particular, the sediment concentration was much more variable with bed shear stress than the sediment velocity.

The results of some Eulerian measurements were compared with those obtained from a Lagrangian standpoint. Almost identical values were obtained for particle velocities, porosities, and sediment fluxes, proving the complementarity between the two approaches.

Notation

U	=	bulk velocity of the flow
R	=	hydraulic radius
d	=	diameter of particle
w	=	volume of particle
$\delta^{/}$	=	viscous sublayer
u^{*}	=	shear velocity
k_s	=	boundary roughness height
q^{*}	=	Dimensionless sediment transport rate per unit width
q_s	=	volumetric sediment transport per unit width
Re_s	=	Settling Reynolds number
u^{*} / u_c^{*}	=	Stage value
L_p	=	particle trajectory
V_p	=	mean velocity of a travelling particle within its trajectory
τ^{*}	=	Shields number
C_A	=	areal concentration
v_A	=	areal average velocity
i	=	index for particle
j	=	index for events
t	=	time coordinate

x = stream-wise coordinate

x_0 = location of a target line

t_0 = time at which a particle reaches a target line

A = reference bed area

L = stream-wise extension of A

N = number of particles in the sample

N_A = number of particles within A

N_A^m = number of moving particles within A

N_A^r = number of particles resting within A

J = number of events within observation of one particle

T = total time of Lagrangian observation

$\langle\theta\rangle$ = average over particle events

$\overline{\theta}$ = average over time

θ' = deviation from a temporal mean

$\{\theta\}$ = average over particles

$\{\theta\}_A$ = average over particles within A

M^m = clipping function for particle motion

M^A = clipping function for particle within $AExpected\ values$

ϑ^m = expected value of porosity

τ = $\tau^m + \tau^r$, expected value of Δt

τ^m = expected value of Δt^m

τ^r = expected value of Δt^r

υ = expected value of u

υ^m = expected value of u^m

ξ = expected value of Δx

C_A^m = concentration of moving particles within A

u_A^m = average velocity of moving particles within A

D = disentrainment rate

E = entrainment rate

φ_A^m = Eulerian porosity

φ_N^m = relative number of particles in motion

φ_T^m = Lagrangian time porosity

l_r = length of a reference (target) line

q = sediment flux crossing a target line

t^d = instant of disentrainment

t^e = instant of entrainment

T^m = total time of motion for one particle

T^r = total time of rest for one particle

u = instantaneous particle velocity

$u^{\Delta x}$ = average particle velocity within a hop

Δt = duration of a particle event (motion+stillness)

Δt^m = duration of a motion event

Δt^r = duration of a stillness event

Δx = length of particle motion (or, hop length, or, displacement in a motion event)

λ = distance travelled by a particle within T

z_v = measured vertical distance

z_b = bed elevation

References

Abbott, J.E., and Francis, J.R.D. (1977), Saltation and suspension trajectories of solid grains in water streams. Philos. Trans., Royal Society of London, A 284, pp. 225-254.

Ancey, C. (2010), Stochastic modeling in sediment dynamics: Exner equation for planar bed incipient bed load transport conditions, J. Geophys. Res., 115, F00A11, doi:10.1029/2009JF001260.

Ancey, C., and J. Heyman (2014), A microstructural approach to bed 922 load transport: mean behaviour and fluctuations of particle transport rates, J. Fluid Mech., 744, 129–168, doi:10.1017/jfm.2014.74.

Ancey, C., Bigillon, F., Frey, P., Ducret, R., and Lanier, J. (2002), Saltating motion of a bead in a rapid water stream, Phys. Rev., E 66:036306.

Ancey, C., T. Böhm, M. Jodeau, and P. Frey (2006), Statistical description of sediment928 transport experiments, Phys. Rev. E, 74(1), doi: 10.1103/PhysRevE.74.011302.

Ashida, K., and M. Michiue (1973), Studies on bed-load transport rate in open channel flows, in Proceedings of the International Association for Hydraulic Research International Symposium on River Mechanics 9–12 January 1973, Bangkok, Thailand, pp. 407–417, Asian Inst. Of Technol., Bangkok.

Bagnold, R. (1956), The flow of cohesionless grains in fluids, Philos.Trans. R. Soc. London A, 249, 235–297.

Bagnold, R. (1980), An empirical correlation of bedload transport rate in flumes and natural rivers, Proc. R. Soc. London, Ser. A, 372, 453–473.

Ballio, F., A. Radice, D. Prokrajac and S. A. Hosseini-Sadabadi (2017), Lagrangian and Eulerian description of bed-load transport, J. Hydraul. Res., (under review)

Ballio, F., V. Nikora, and S. E. Coleman (2014), On the definition of solid discharge in hydroenvironment research and applications, J. Hydraul. Res., 52(2), 173–184, doi:10.1080/00221686.2013.869267.

Böhm, T., C. Ancey, P. Frey, J. Roboud, and C. Ducottet (2004), Fluctuations of the solid discharge of gravity-driven particle flows in a turbulent stream, Phys. Rev. E, 69(6 1), 061307, doi: 10.1103/PhysRevE.69.061307.

Böhm, T., Frey, P., Ducottet, C., Ancey, C., Magali, J., and Reboud, J. (2006), Two-dimensional motion of a set of particles in a free surface flow with image processing, Exp. in Fluids, vol.41(1), pp. 1-11.

Bridge, J. S., and D. F. Dominic (1984), Bed load grain velocity and sedimen transport rates, Water Resour. Res., 20, 476–490.

Campagnol, J., (2012), Characterization of bed-load sediment transport t the grain scale. Politecnico di Milano.

Campagnol, J., A. Radice, and F. Ballio (2012), Scale-based statistical analysis of sediment fluxes, Acta Geophys., 60(6), 1744–1777, doi: 10.2478/s11600-012-0028-6.

Campagnol, J., A. Radice, F. Ballio, and V. Nikora (2015), Particle motion and diffusion at weak bed load: accounting for unsteadiness effects of entrainment and disentrainment, J. Hydraul. Res., 53(5), 633–648, doi:10.1080/00221686.2015.1085920.

Campagnol, J., A. Radice, R. Nokes, V. Bulankina, A. Lescova, and F. Ballio (2013), Lagrangian analysis of bed-load sediment motion: database contribution, J. Hydraul. Res., 51(5), 589–596, doi:10.1080/00221686.2013.812152.

Chanson, H. (1999), The Hydraulics of open channel flow: an introduction, Elsevier Butterworth-Heinemann

Cohen, H., J. B. Laronne, and I. Reid (2010), Simplicity and complexity of bed load response during flash floods in a gravel bed ephemeral river: A10 year field study, Water Resour. Res., 46, W11542, doi: 10.1029/2010WR009160.

Coleman, S. E., and V. I. Nikora (2011), Exner equation: a continuum approximation of a discrete granular system, Water Resour. Res., 45(9), 1–8, doi: 10.1029/2008WR007604.

Dey, S. (1999), Time-variation of scour in the vicinity of circular piers. Water Marit Energ Proc

Dey, Subhasish. *Fluvial Hydrodynamics.* Springer-Verlag Berlin Heidelberg, 2014.

Dietrich, WE, Smith JD (1984) Bedload transport in a river meander. Water Resour Res 20(10):1355–1380

Drake, T. G., Shreve, R. L., Dietrich, W. E., Whiting, PJ, Leopold, L. B. (1988), Bedload transport of fin gravel observed by motion picture photography. J Fluid Mech 192:193–217.

Duboys, S. (1879), Lerhone et les rivieres à lit affoillable, Ann. Ponts Chaussees, Ser., 5, 18, 141–195.

Einstein, H. (1950), The bed-load function for sediment transportation in open channel flows, Tech. Bull. 1026, U.S. Dep. of Agric., Washington, D. C.

Engelund, F., and J. Fredsoe (1976), A sediment transport model for straight alluvial channels, Nord. Hydrol., 7(5), 293–306.

Ettema, R. (2008), Ice effects on sediment transport in rivers. In: Garcìa MH (ed) Sedimentation

Fan, N., A. Singh, M. Guala, E. Foufoula-Georgiou, and B. Wu (2016), Exploring a semimechanistic episodic Langevin model for bed load transport: Emergence of normal and anomalous advection and diffusion regimes, Water Resour. Res., 52, 2789–2801, doi:10.1002/2015WR018023.

Fathel, S. L., D. J. Furbish, and M. W. Schmeeckle (2015), Experimental evidence of statistical ensemble behavior in bed load sediment transport, J. Geophys. Res. – Earth Surf., 120, doi: 10.1002/2015JF003552

Fernandez-Luque, R., and R. Van Beek (1976), Erosion and transport of bed-load sediment, J. Hydraul. Res., 14, 127–144.

Francis, J. (1973), Experiments on the motion of solitary grains along the bed of a water-stream, Proc. R. Soc. London, Ser. A, 332, 443–471.

Frey, P., C. Ducottet, and J. Jay (2003), Fluctuations of bed load solid discharge and grain size distribution on steep slopes with image analysis, Exp. Fluids, 35(6), 589–597, doi:10.1007/s00348-003-0707-9

Furbish, D. J., J. C. Roseberry, and M. W. Schmeeckle (2012a), A probabilistic description of the bed load sediment flux: 3. the particle velocity distribution and the diffusive flux, J. Geophys. Res. – Earth Surf., 117(3), F03033, doi: 10.1029/2012JF002355.

Furbish, D. J., P. K. Haff, J. C. Roseberry, and M. W. Schmeeckle (2012b), A probabilistic description of the bed load sediment flux: 1. Theory, J. Geophys. Res. – Earth Surf., 117, F03031, doi:10.1029/2012JF002352.

Garcia, C., H. Cohen, I. Reid, A. Rovira, X. Úbeda, and J. B. Laronne (2007), Processes ofinitiation of motion leading to bedload transport in gravel-bed rivers, Geophys. Res. Lett., 34(6), L06403, doi: 10.1029/2006GL028865.

Gomez, B. (1991), Bedload transport, Earth Sci. Rev., 31(2), 89–132.

Hassan, M. A, H. Voepel, R. Schumer, G. Parker, and L. Fraccarollo (2013), Displacement characteristics of coarse fluvial bed sediment, J. Geophys. Res. – Earth Surf.,118, 155–165, doi: 10.1029/2012JF002374.

Heathershaw, A. D, Thorne, P.D (1985) Sea-bed noises reveal role of turbulent bursting

Heays, K. G., H. Friedrich, B. W. Melville, and R. Nokes (2014), Quantifying the dynamic evolution of graded gravel beds using Particle Tracking Velocimetry, J. Hydraul. Eng.,140(7), 04014027, doi: 10.1061/(ASCE)HY.1943-7900.0000850.

Heritage, G.L., and Milan, D.J. (2009), Terrestrial laser scanning on grain roughness in a gravel-bed river, Geomorphology, vol.113(1-2), pp.4-11.

Hu, C., and Hui, Y. (1996), Bed-load transport. I: Mechanical characteristics, J. Hydraul. Eng., vol. 122, pp. 245–254.

Keshavarzy, A., and Ball, J.E. (1999), An application of image processing in the study of sediment motion, J. Hydraul. Res., vol. 37, No 4, pp. 559-576.

Lajeunesse, E., L. Malverti, and F. Charru (2010), Bed load transport in turbulent flow at the grain scale: Experiments and modeling, J. Geophys. Res. – Earth Surf., 115, F04001, doi:10.1029/2009JF001628.

Lee, H. Y, Lin, Y. T., You, J. Y., and Wang, H. W. (2006), On three dimensional continuous saltating process of sediment particles near the channel bed, J. Hydraul. Res., vol. 44(3), pp. 347-389.

Lee, H. Y., Y. H. Chen, J. Y. You, and Y. T. Lin (2000), Investigations of continuous bedload saltating process, J. Hydraul. Eng., 126(9), 691–700, doi: 10.1061/(ASCE)0733-9429(2000)126:9(691).

Lee, H.Y., and Hsu, I.S. (1994), Investigation of saltating particle motions. J. Hydraul. Eng., vol. 120, pp. 831-845.

Lisle, I. G., C. W. Rose, W. L. Hogarth, P. B. Hairsine, G. C. Sander, and J. Y. Parlange (1998), Stochastic sediment transport in soil erosion, J. Hydrol., 204, 217–230, doi:http://dx.doi.org/10.1016/S0022-1694(97)00123-6.

Liu, Y., F. Metivier, E. Lajeunesse, P. Lancien, C. Narteau, and P. Meunier (2008), Measuring bed load in gravel bed mountain rivers: Averaging methods and sampling strategies, Geodin. Acta, 21, 81–92.

Martin, R. L., D. J. Jerolmack, and R. Schumer (2012), The physical basis for anomalous diffusion in bed load transport, J. Geophys. Res. – Earth Surf., 117, F01018, doi:10.1029/2011JF002075.

Métivier, F., P. Meunier, M. Moreira, A. Crave, C. Chaduteau, B. Ye, and G. Liu (2004), Transport dynamics and morphology of a high mountain stream during the peak flow season: The Ürümqi River (Chinese Tian Shan), in River Flow 2004, vol. 1, pp. 770–777, A. A. Balkema, Leiden, Netherlands.

Meunier, P., F. Metivier, E. Lajeunesse, A. S. Meriaux, and J. Faure (2006), Flow pattern and sediment transport in a braided river: The "torrent de St Pierre" (French Alps), J. Hydrol., 330, 496–505.

Meyer-Peter, E., and R. Müller (1948), Formulas for bed-load transport, paper presented at 2nd Meeting of International Association for Hydraulic Research, Int. Assoc. for Hydraul. Res., Stockholm.

Nelson, J.M., R.L. Shreve, S.R. McLean, and T.G. Drake (1995), Role of near-bed turbulence in bed-load transport and bed form mechanics, Water Resour. Res., vol. 31, pp. 2071-2086.

Nelson, J.M., R.L. Shreve, S.R. McLean, and T.G. Drake (1995). Role of near-bed turbulence in be load transport and bed form mechanics, Water Resour. Res., vol. 31, pp. 2071-2086.

Nikora, V., H. Habersack, T. Huber, and I. McEwan (2002), On bed particle diffusion in gravel bed flows under weak bed load transport, Water Resour. Res., 38, 171–179.

Nikora, V., J. Heald, D. Goring, & I. McEwan (2001), Diffusion of saltating particles in unidirectional water flow over a rough granular bed, J. Phys. A, Mathematical and General, 34, L743–L749, doi: 10.1088/0305-4470/34/50/103.

Niño, Y., and García, M. (1996), Experiments on particle-turbulence interaction in near-wall region of an open channel flow: implication for sediment transport, J. Fluid. Mech., vol.326, pp. 285-319.

Niño, Y., and García, M. (1998), Experiments on saltation of sand in water, J. Hydraul. Eng., vol124(10), pp. 1014-1025.

Niño, Y., and M. Garcìa (1998), Using Lagrangian particle saltation observations for bedload sediment transport modelling, Hydrol. Process., 12(8), 1197–1218, doi:10.1002/(SICI)1099-1085(19980630)

Niño, Y., García, M., and Ayala, L. (1994), Gravel saltation 1. Experiments, Water Resour. Res., vol. 30(6), pp. 1907-1914.

Nokes, R. (2012), Streams v. 2.00. System theory and design, University of Canterbury, Christchurch, New Zealand, url: http://www.civil.canterbury.ac.nz/streams. shtml.

Papanicolaou, A. N, Diplas, P., Evaggelopoulos, N, Fotopoulos, S. (2002), Stochastic incipient motion criterion for spheres under various bed packing conditions. J Hydraul Eng 128(4):369–380

Papanicolaou, A. N., P. Diplas, N. Evaggelopoulos, and S. Fotopoulos (2002), Stochastic incipient motion criterion for spheres under various bed packing conditions, J. Hydraul. Eng., 128(4), 369–380, doi: 10.1061/(ASCE)0733-(2002)128:4(369).

Papanicolaou, A.N., Diplas P., Balakrishnan M., and Dancey CL (1999), Computer vision technique for tracking bed load movement, Journal of Computing in Civil Engineering, vol. 13, pp. 71–79.

Parker, G., Seminara, G., Solari, L. (2003), Bed load at low Shields stress on arbitrarily sloping beds:alternative entrainment formulation. Water Resour Res 39(7):1183

Radice, A. (2009), Use of the Lorenz curve to quantify statistical nonuniformity of sediment

Radice, A., and F. Ballio (2008), Double-average characteristics of sediment motion in one dimensional bed load, Acta Geophys., 56(3), 654–668, doi: 10.2478/s11600-008-0015-0.

Radice, A., F. Ballio, and V. Nikora (2009), On statistical properties of bed-load sediment concentration, Water Resour. Res., 45(6), W06501, doi: 10.1029/2008WR007192.

Radice, A., S. Sarkar, and F. Ballio (2017), Image-based Lagrangian particle tracking in bedload experiments, J. Vis. Exp., under review.

Radice, A., V. Nikora, J. Campagnol, and F. Ballio (2013), Active interactions between turbulence and bed load: Conceptual picture and experimental evidence, Water Resour Res., 49(1), 90–99, doi: 10.1029/2012WR012255.

Ramesh, B., U. C. Kothyari and K. Murugesan 1055 (2011), Near-bed particle motion over transitionally-rough bed, J. Hydraul. Res., 49(6), 757–765, doi:10.1080/00221686.2011.620369.

Recking, A., P. Frey, A. Paquier, and P. Belleudy (2009), An experimental investigation of mechanisms involved in bed load sheet production and migration, J. Geophys. Res., 114, F03010, doi:10.1029/2008JF000990.

Roseberry, J. C., M. W. Schmeeckle, and D. J. Furbish (2012), A probabilistic description of the bed load sediment flux: 2. Particle activity and motions, J. Geophys. Res. – Earth Surf., 117(3), F03032, doi: 10.1029/2012JF002353.

Schmid, A. (1985), Wandnahe turbulente bewegungsabläufe und ihre bedeutung für die

Sechet, P., and Le Guennec, B. (1999), Bursting phenomenon and incipient motion of solid particles in bed-load transport, J. Hydraul. Res., vol. 37, pp. 683-696.

Seminara, G., Solari, L., and Parker, G. (2002), Bed load at low Shields stress on arbitrarily slopin beds: failure of the Bagnold hypothesis, Water Resour. Res., vol. 38(11), pp. 31-1/31-16.

Seminara, L., L. Solari, and Parker, G. (2002), Bed load at low Shields stress on arbitrarily sloping beds: Failure of the Bagnold hypothesis, Water Resour. Res., 38(11), 311–316.

Shields, A. (1936), Anwendung der Aehnlichkeitsmechanik und der Turbulenzforschung auf die Geschiebebewegung, Mitteilungen der Preußischen Versuchsanstalt für Wasserbau (in German) 26. Berlin.

Singh, A., K. Fienberg, D. J. Jerolmack, J. Marr, and E. Foufoula-Georgiou (2009), Experimental evidence for statistical scaling and intermittency in sediment transport rates, J. Geophys. Res. – Earth Surf., 114, F01025, doi:10.1029/2007JF000963.

Sutherland, A. J. (1967) Proposed mechanism for sediment entrainment by turbulent flows transport rate. J Hydraul Eng 135(4):320–326

Turowski, J. M. (2010), Probability distributions of bed load transport rates: A new derivation and comparison with field data, Water Resour. Res., 46(8), W08501, doi:10.1029/2009WR008488.

Wong, M. (2003), Does the bedload equation of Meyer-Peter and Müller fit its own data?, paper presented at 30th Congress of the International Association for Hydraulic Research, Int. Assoc. of Hydraul. Res., Thessaloniki, Greece.

Yalin, M. S. (1977), Mechanics of sediment transport. Pergamon, Oxford.

Yalin, M. S., da Silva AMF. (2001), Fluvial processes. IAHR Monograph, International Associatio for Hydraulic Research, Delft.

Zanke, U.C.E. (2003). On the influence of turbulence on the initiation of sediment motion, Int. J.Sediment Research, vol. 18, pp. 17-31.